UCLouvain

Université catholique de Louvain
Secteur des Sciences et Technologies
Institut de Recherche en Mathématique et Physique
Centre for Cosmology, Particle Physics and Phenomenology

Muography: using cosmic rays as an imaging tool for volcanology and cultural heritage applications

Doctoral dissertation presented by

Marwa Al Moussawi

in fulfilment of the requirements for the degree of Doctor in Sciences

Thesis jury commission

Dr. Andrea Giammanco (Supervisor)	UCLouvain, Belgium
Prof. Eduardo Cortina Gil (Supervisor)	UCLouvain, Belgium
Prof. Philippe Ruelle (Chair)	UCLouvain, Belgium
Prof. Christophe Delaere	UCLouvain, Belgium
Prof. Michael Tytgat	VUB, Belgium
Prof. Haitham Zaraket	Lebanese University, Lebanon

January, 2024

Acknowledgement

I express heartfelt thanks to everyone who contributed significantly to the successful completion of my PhD journey. Their consistent support, guidance, and expertise have been truly invaluable.

First and foremost, I express my heartfelt thanks to my supervisors, Dr. Andrea Giammanco and Prof. Eduardo Cortina Gil. They consistently provided guidance not only in academia but also in my personal life. I appreciate them for being like my second family, offering support during challenging times. Their profound knowledge, continuous encouragement, and feedback were instrumental in shaping my research and refining my scholarly abilities. I consider myself fortunate to have worked with them. My gratitude also extends to Prof. Haitham Zaraket, who significantly contributed to my success from my third year of university up to my PhD. I appreciate him for being a special mentor, teaching me a lot about physics.

I thank my jury members, Prof. Philippe Ruelle, Prof. Christophe Delaere, and Prof. Michael Tytgat, for their valuable contributions during the evaluation and correction of my thesis.

Special thanks go to all MURAVES collaboration members, particularly Giulio Saracino and Luigi Cimmino, for their insightful comments and shared expertise. Additionally, I am deeply grateful to Pavel Demin, Laurent Bruniaux, Nicolas Szilasi, and Ayman Youssef for their outstanding contributions to the technical and electronics solutions that played a pivotal role in the success of our portable muoscope at CP3.

Gratitude is also owed to all CP3 members, who have become a second family. A special acknowledgment goes to our secretary, Carinne Mertens, and Stéphanie Laudrain for their unwavering administrative support.

To my special friends at CP3, especially the muography team: Ishan Darshana, Maxime Lagrange, Zahraa Zaher, Amrutha Samalan, Samip Basnet, and Vishal Kumar, thank you for hearing me, supporting me during challenging times, and being part of my good days. Thanks for believing in me and providing a listening ear during those years.

Reflecting on my journey, I cannot overlook the sacrifices of the martyrs in my country, to whom I owe gratitude for the gift of safety and life for me and my family.

To my dearest family—Mom, Dad, my lovely brothers Mouhamad, Ibrahim, Hassan, my lovely sister Roba, and my very special little Sara—you are the meaning of my life. I am grateful for everything, thanks for being an integral part of all my successes, which I dedicate to you.

To my special and beloved one, Rakan, words cannot fully express my gratitude for your unwavering support, promises, love, and sacrifices. Your presence has been my strength, and I acknowledge that I could not have completed this journey without you.

To my second family, my mother-in-law Jamila, my dear ones Rana, Achwaa, Rawaa, Amani, Safaa, and Zeinab, and my second brothers Mouhamad and Elie—thank you for being part of my life and offering unwavering support.

Preface

Cosmic rays, originating from various astrophysical processes both within and beyond our galaxy, are high-energy particles. Propagating in all directions, these particles consistently reach Earth's atmosphere and engage in collisions with air nuclei, resulting in the generation of particle showers, which include muons. Muons, similar to electrons but significantly heavier, possess the capability to penetrate dense materials. This property renders them suitable for peering inside structures of considerable dimensions, analogous to how X-rays are utilized in X-ray radiography. Muography utilizes cosmic muons as an imaging tool across diverse fields such as archaeology, civil engineering, geology, nuclear reactor monitoring, nuclear waste characterization, underground surveys, and cultural heritage.

Embarking on this exploration, the first chapter delves into the fundamentals of cosmic muons, tracing their origin from primary cosmic rays to their interactions in the atmosphere. Unveiling the intricacies of muon imaging, we explore radiographic and tomographic methods, shedding light on diverse applications in fields such as archaeology, volcanology, and nuclear safety.

In Chapter 2, our attention shifts to Monte Carlo simulations, encompassing the entire process from cosmic muon generation to their passage through the object of interest and the details of detector response. The chapter compares various Monte Carlo approaches at each step, providing a comprehensive evaluation of their respective methodologies.

Chapter 3 describes the MURAVES detector, with a emphasis on developing the simulation chain. Offering an in-depth exploration of its design, objectives, and preliminary results, we navigate through hardware intricacies and simulation nuances.

Chapter 4 delves into the development of the Portable Muoscope, featuring Resistive Plate Chambers (RPCs). The discussion extends from the application of resistive coatings to addressing environmental challenges. This chapter navigates through the design, testing, calibration, and performance studies of our detector, enhanced by simulations using Garfield++ for a deeper understanding.

The final chapter presents a pioneering exploration of muon applications in cultural heritage preservation. Our focus in this chapter is on advocating for the adoption of portable and safe muography, particularly in a regime new for muography (relatively low size). Our simulation study illustrates the potential

applications and limitations of muography, further delving into measuring momentum and identifying electrons (e-) and positrons (e+), with the aim of substantially enhancing the sensitivity of muographic imaging.

Contents

1. Chapter
Cosmic muons

1.1. Primary cosmic rays

Muography is based on the existence of a natural steady stream of cosmic particles from outer space, which has been extensively investigated and quantified over the last century. This radiation was first discovered in 1912 [1], when Victor Hess ascended to 5300 meters on a balloon and measured the rate of ionization in the atmosphere, discovering that it increased to around three times that at sea level. He attributed this overabundance to penetrating radiation entering the atmosphere from above; this is what we now call cosmic rays. These high-energy particles are an important feature of the interstellar and intergalactic medium. They continuously impinge the Earth's atmosphere with an intensity of about 10000 particles per second per square meter (falling off with increasing energy), most abundantly (89 %) protons (nuclei of hydrogen), but they also include (10 %) nuclei of helium and (1 %) other heavier nuclei, significantly up to iron. Those particles are generally called primary cosmic rays.

Cosmic ray research opened the door to a world of particles beyond the bounds of the atoms : the positron (the antielectron) was found in 1932 [2] and the muon in 1937 [3], followed by the pion [4], the kaon [5], and numerous more. Until the early 1930s, when high-energy particle accelerators were introduced, natural radiation was the only means to explore the expanding particle "zoo". Indeed, when CERN was established in 1954, one of its scientific concerns was cosmic rays. Despite the fact that accelerators were the finest hunting ground for new particles, the physics of cosmic rays is still intensively investigated.

The energies of primary particles ranges from 1 GeV (the energy of a small particle accelerator) to as much as 10^8 TeV (more than the Large Hadron Collider's beam energy). Figure 1.1 [6] shows the observed cosmic ray spectrum across energies from 1 GeV to 10^{12} GeV and reveals a power-law spectrum, $J(E) \propto E^{-\alpha}$, where J is the intensity, E the kinetic energy per nucleon and α the spectral index. The spectral shape bends downward for low energies (below 30 GeV) due to the modulation imposed by the presence of a magnetic wind that originates from our Sun and prevents extremely low energy particles from entering the inner solar system. $\alpha \sim 2.7$ for the hadronic component at energies above ~ 30 GeV, and this value is constant over many decades of energy up
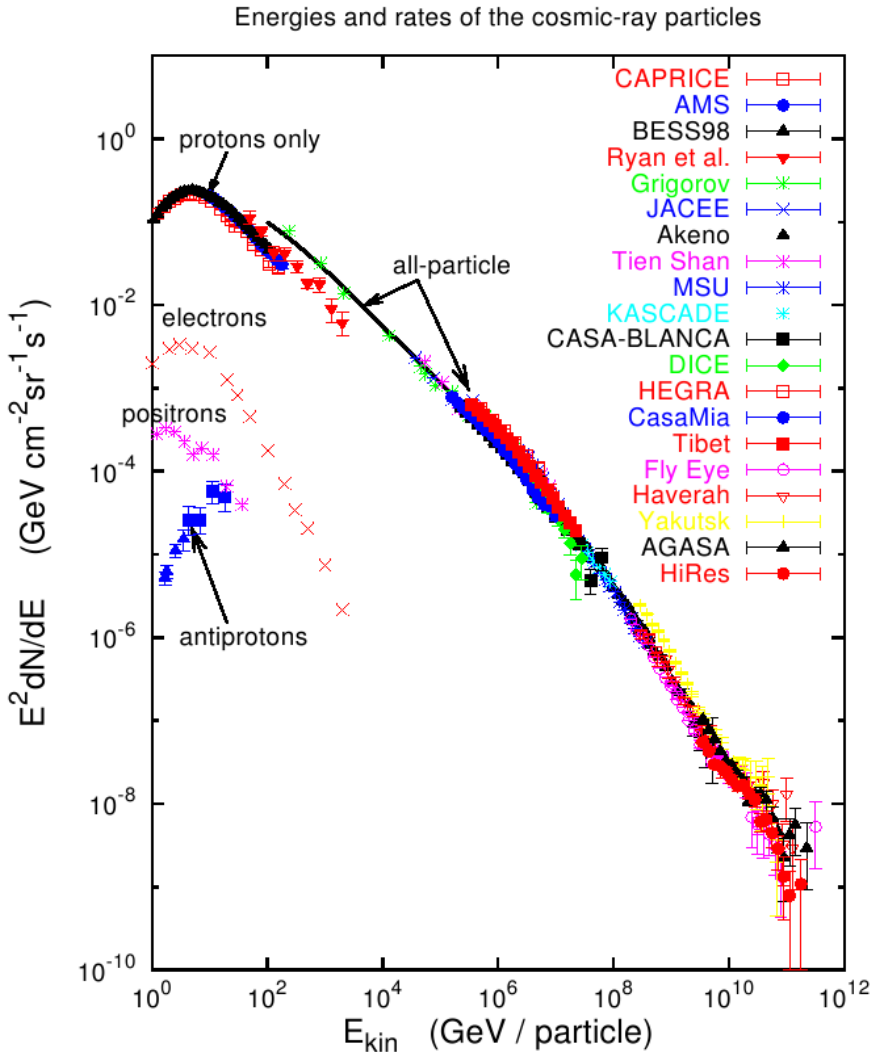
Figure 1.1. ǀ The intensity spectrum of cosmic rays extends over more than ten orders of magnitude in energy with a smooth spectrum $I(E) \sim E^{-2.7...3.0}$. Figure from [6]

to the so-called "knee" at $\sim 3 \times 10^6$ GeV, which was first discovered in 1958 by Kulikov and Khristiansen [7], after which the spectrum steepens and reaches a slope of $\alpha \sim 3$ with a slightly falling tendency to reach about ~ 3.15 at 10^9 GeV. Beyond the so-called "ankle" at $\sim 10^{10}$ GeV, where the extragalactic component is likely prominent, the spectrum seems to flatten with $\alpha \sim 2.7$ at extremely high energies. The origin of the "knee" in the energy spectrum is very important

for the understanding of the origin of cosmic rays. Various theories have been proposed to explain this phenomenon, with one prevalent idea linking the knee to the upper limit of acceleration achievable by galactic supernovae. According to this theory, the maximum energy attainable through the Fermi process is directly proportional to the charge of the nucleus, as expressed in equation [8]:

$$E_{max} \leq Z \times 3 \times 10^4 GeV \tag{1.1.}$$

Enrico Fermi proposed the Fermi acceleration process in 1949. In this mechanism, charged particles gain energy through collisions with interstellar clouds, propelling them to higher energies. However, this acceleration process is not limitless; there exists an upper threshold determined by the charge of the nucleus. As stated in eq 1.1, the maximum energy (E_{max}) a particle can achieve is directly proportional to the nucleus charge (Z). This fundamental limitation sets the stage for the knee phenomenon observed in the cosmic ray energy spectrum. Consequently, as particles approach this energy cut-off, the composition of cosmic rays should gradually become enriched in heavier nuclei if there is a steepening of the spectrum caused by the end-point of this type of acceleration mechanism [9].

Another possible reason for the knee phenomenon is a shift in the galactic cosmic rays path (rigidity cut-off), where rigidity, a fundamental parameter in cosmic ray physics, plays a vital role in deciphering the behavior of charged particles in magnetic fields. Rigidity (R), denoted as [10]:

$$R = r_L B = \frac{pc}{Ze} \tag{1.2.}$$

offers valuable insights into cosmic particle trajectories. Here r_L known as Larmor radius or gyroradius, signifies the orbit's radius of a charged particle moving in a uniform perpendicular magnetic field, p represents momentum, B is the magnetic field strength, c is the speed of light, Z denotes the charge of the nucleus, and e represents the elementary charge. Rigidity-dependent galaxy leakage, which increases with energy [11], could cause protons to steepen first, followed by helium and heavier nuclei, assuming the steepening effect correlates uniformly with rigidity for all particles. According to this scenario, the composition would get heavier while the spectrum of all particle energies per nucleus would get steeper. The existence of other sources and acceleration mechanisms, such as neutron stars, binary systems, and the same large supernova leftovers, can be a third factor [12]. Contrary to the earlier prediction, this would predict the onset of a new proton source in this energy range.

1.2. Cosmic rays in the atmosphere

Upon entering the atmosphere, the primary cosmic radiation interacts with the electrons and nuclei of the atoms and molecules that make up the air. As a result, the radiation's composition changes as it travels through the atmosphere, as particles lose their energy through hadronic and/or electromagnetic processes. This causes an extended air shower (EAS), which consists of three components: The photon-electron component grows primarily in the electromagnetic cascade process, which is primarily started by neutral pion decay, the muon component, which primarily results from the decay of charged pions but also from kaons, charmed and beauty particles, and the hadronic component, which for energetic events constitutes the core of a cascade or shower.

These secondaries transverse momenta lead the particles to expand laterally as they travel through the atmosphere. The particles become less and less energetic as the cascade progresses longitudinally, penetrating deeper and deeper, as the energy of the originating particle is divided and redistributed among more and more participants. The atmospheric depth X, measured in g/cm^2, is a crucial quantity for describing the interactions and subsequent propagation of the particles created. It is defined as the integral in height of the atmospheric density above the observation level h:

$$X = \int_h^\infty \rho(h') \, dh' \sim X_0 e^{-h/h_0} \tag{1.3.}$$

A rough estimate for an isothermal atmosphere was employed in the last step, where $h_0 \sim 8.4 km$ is the scale height in the atmosphere and $X_0 = 1030 g/cm^2$ is the atmospheric depth at sea level [13]. Regarding particles that are incident vertically, relation 1.3 is applicable. The atmospheric depth is scaled by $1/\cos\theta$ to give the slant depth at zenith angles $\theta \leq 70^\circ$, for which the flat Earth approximation holds. The Earth's curvature must be taken into account for bigger zenith angles. According to the atmospheric profile, the total horizontal atmospheric depth ($\theta \sim 90^\circ$) is about $36000 g/cm^2$.

Nitrogen and oxygen make up the majority of the nuclei in the Earth's atmosphere (78% and 21% of all nuclei, respectively), which makes the primary beam interaction target is made up of a mixture of protons and neutrons.

And since the majority of those secondary particles (produced by hadronic interactions) are unstable and can decay while traveling through the atmosphere, the decay probabilities must be recognized and correctly accounted for when computing particle fluxes and energy spectra. The decay probability of a secondary particle of momentum $p[GeV/c]$ after traversing vertically a thickness $X[g/cm^2]$ in a medium of matter density $\rho[g/cm^3]$ can be evaluated, resulting in

$$W = 1 - exp\left[- \int \frac{m_0}{\rho \tau_0 p} dX \right] \sim \frac{m_0 X}{\rho \tau_0 p} \qquad (1.4.)$$

where $\tau_0[s]$ and $m_0[GeV/c^2]$ are respectively the mean life and mass of the unstable particle under consideration at rest. According to the relation shown above (1.3), if an unstable particle is impacted at a zenith angle of $\theta > 0^{\circ}$ (inclined trajectories), the probability for the decay along its path in a specific atmospheric depth X is enhanced by the factor $sec(\theta)$,

$$W = \frac{m_0 X sec(\theta)}{\rho \tau_0 p} \qquad (1.5.)$$

This equation makes it clear that the decay probability of a particle for a particular column of air is dependent on the particle's mean life, momentum (or energy), density (or altitude), and zenith angle of propagation in the atmosphere.

Figure 1.2 shows the vertical fluxes of the secondary cosmic ray components in the atmosphere as a function of atmospheric depth for E > 1 GeV. Except for protons and electrons towards the top of the atmosphere, all particles are formed by interactions of primary cosmic rays in the air. Muons and neutrinos are produced by the decay of charged mesons, whereas electrons and photons are produced by the decay of neutral mesons.

The charged particle and photon flux in the atmosphere exhibits a local maximum in the altitude range of about 15-26 km, known as the Pfotzer Maximum [14, 15], which corresponds to the maximum of secondary particle production, where the flux rises with depth until it reaches a maximum at $100 g/cm^2$, after which it begins to fall, due to energy loss, absorption and decay processes.

Based on a particle's capacity to penetrate 15 cm of lead (i.e., $167 g/cm^2$ in thickness), cosmic radiation can be classified as a hard or soft component. The hard penetrating component is made up of energetic hadrons and muons, whereas the soft component, which cannot penetrate this thickness, is mostly made up of electrons, photons and low energy muons. Depending on the altitude, one may dominate the other. At sea level, muons make up the majority of the hard component.

1.3. Cosmic-rays muons

In a cloud chamber experiment in 1936, Carl D. Anderson and Seth Neddermeyer noticed particles in the cosmic radiation that curled differently from other known particles when they passed through magnetic fields. It was then assumed that their mass was greater than that of an electron but smaller than that of a proton. It was once believed to be the particle Hideki Yukawa, a
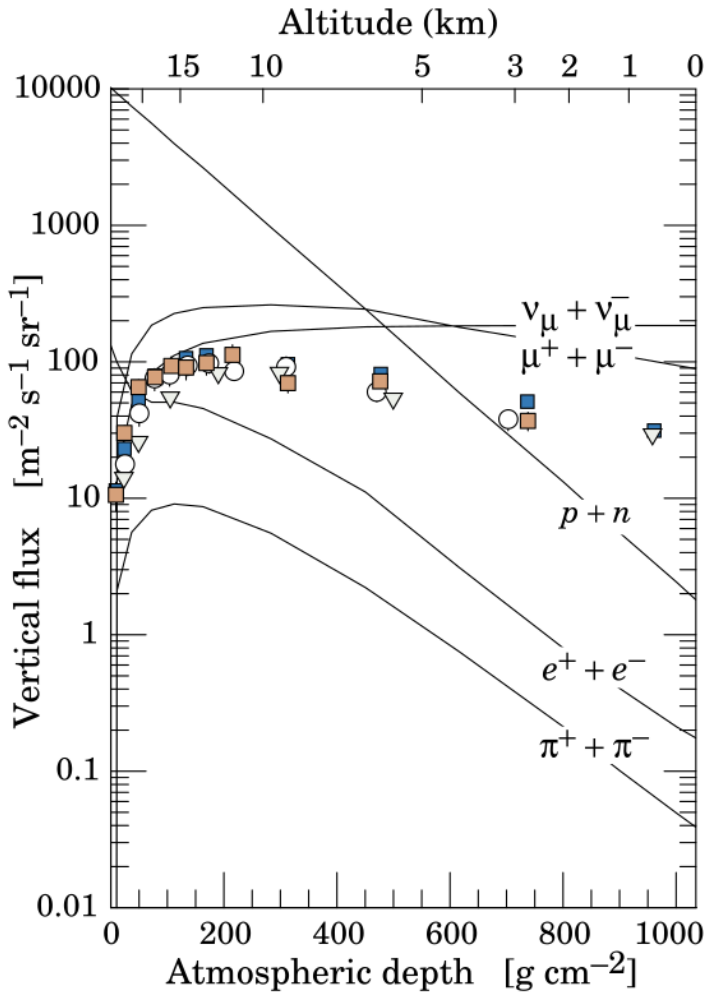
Figure 1.2. | Vertical fluxes of various particles, for momenta larger than 1 GeV. Points correspond to measurements of the vertical flux of negative muons only, with different symbols corresponding to different experiments [10].

Japanese scientist [16], had hypothesized in 1935 to explain the strong force that holds protons and neutrons together in atomic nuclei due to its mass. However, it was later found that a muon belongs to the lepton group since it never interacts with nuclei or other particles via the strong interaction. Muons are unstable elementary particles (200 times heavier than electrons) with lifetime of 2.2 μs before decaying into an electron and two different types of neutrinos by the weak interaction.

1.3.1. Atmospheric muon production

After entering the atmosphere, primary cosmic rays, which are mostly protons, collide with the atmosphere's oxygen and nitrogen nuclei. These collisions are under the strong nuclear force control. The most typical subatomic particles created in these collisions are pions($\pi^{\pm}, \pi^0$) and kaons ($K^{\pm}, K_0^S, K_0^L$), which decay into muons when charged. When not decaying into muons immediately, kaons decay into two or three pions, which, in turn decay into muons.

The majority of muons are produced high in the atmosphere, usually around 15 km, by following the processes:

$$\pi^{\pm} \rightarrow \mu^{\pm} + \nu_{\mu}(\overline{\nu}_{\mu}) \qquad (1.6.)$$

$$K^{\pm} \rightarrow \mu^{\pm} + \nu_{\mu}(\overline{\nu}_{\mu}) \qquad (1.7.)$$

with branching ratios respectively of the $\sim 100\%$ (lifetime $= 2.6 \times 10^{-2} \mu s$) and $\sim 63.5\%$ (lifetime $= 1.2 \times 10^{-2} \mu s$) [17].

The time dilation effect of special relativity from the Earth's perspective, $\Delta t_{Earth} = \Delta t_{\mu}/\sqrt{1 - v_{\mu}^2/c^2}$, permits cosmic ray muons to survive the distance down to the Earth's surface. At sea level, muons account for around 80% of the charged portion of secondary cosmic rays. About one particle per cm^2 every minute, and integral intensity of vertical muons : $I_V(E_{\mu} > 1 GeV) \sim 70 m^{-2} s^{-1} sr^{-1}$ [18].

The meson source spectrum directly affects the muon spectrum at Earth's surface. The probability of muon decay rises at low energies. The typical decay length ($d_{\mu} \sim \gamma \tau_{\mu} c$) of a muon with energy of 1 GeV corresponding to a Lorentz factor of $\gamma \sim 10$ is $\sim 6 km$. Due to the fact that pions are normally created at altitudes of 15 km and decay very quickly (for $\gamma = 10$, the decay length is only $d_{\pi} \sim 78 m$), the decay muons do not reach sea level but instead decay or are absorbed by the atmosphere.

The scenario changes when high energies are present. For pions of 100 GeV the interaction probability dominates ($d_{\pi} > \lambda_{\pi}$). Pions with these energies will so make more tertiary pions in subsequent interactions, which will similarly decay ultimately into muons, but with degraded energy. As a result, the muon spectrum at high energies is always steeper than the parent pion spectrum.

The average muon energy at sea level is $\sim 4 GeV$ [10]. In the 10-100 GeV range, the energy spectrum is progressively steepens to reflect the primary spectrum, and steepens even more at higher energies because pions with $E_{\pi} > \epsilon_{\pi} = 115 GeV$ prefer to interacts in the atmosphere before decaying.

Muons having an energy of $E_{\mu} \sim 3 GeV$ have an overall angular distribution $\propto \cos \theta^2$, which is typical of muons. At lower energies, the angular distribution steepens more and more, while at higher energies, it flattens and approaches a
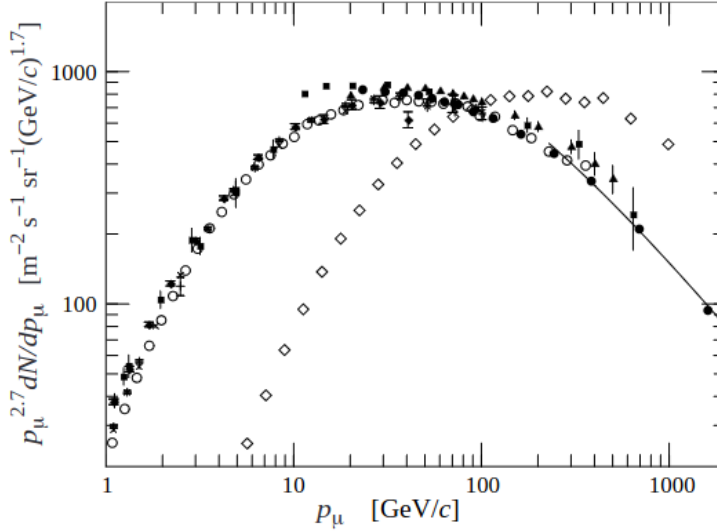
Figure 1.3. ∥ Spectrum of muons at $\theta = 0°$ (○, ●, ■, ▼, ×, +) and $\theta = 75°$ (◇) [10]. The line plots the result from eq 1.9 for vertical showers.

$sec\theta$ distribution for $E_\mu \gg \epsilon_\pi$ and $\theta < 70°$. The muon energy spectrum at sea level is showed in Figure 1.3 for two different zenith angles, $\theta = 0°$ and $\theta = 75°$. The average muon energy rises at large angles because high energy pions decay before interacting and low energy muons decay before reaching the surface.

Another factor needs to be taken into consideration when thinking about muons coming from inclined horizontal directions: muon parent particles travel relatively long distances in rare parts of the atmosphere with large zenith angles. In comparison to the interaction probability, the decay probability is higher due to the low area density at high elevations for inclined directions. As a result, for inclined directions pions will decay mainly into high-energy muons. And due to muon decays and the larger atmosphere absorption effects at big zenith angles, the strength of muons coming from horizontal directions at low energy is naturally reduced.

1.3.2. Muon flux

The probability of producing a muon with energy E_μ by the above processes at a slant depth X in the atmosphere depends on the decay probabilities of π and K mesons, whereas the total muon flux reaching a certain depth is also influenced by muon energy loss and decay in flight. These effects can be accounted for by adding a suppression factor S_μ to the muon flux, as follows:

$$\frac{dN_\mu}{dE_\mu} = S_\mu(E_\mu) \times \frac{dN_{0\mu}}{dE_\mu} \tag{1.8.}$$

At high energies when $S_\mu \to 1$, assuming the intensity of primary proton $I_p(E) \sim 1.8 \times (E/1GeV)^{-\alpha} cm^{-2} s^{-1} sr^{-1} GeV^{-1}$, with $\alpha \sim 2.7$. The muon flux at sea level, according to [19], may be approximated by:

$$\frac{dN_\mu}{dE_\mu d\Omega} \approx 0.14 \frac{E_\mu^{-2.7}}{GeV.sr.cm^2.s} \left[\frac{1}{1 + \frac{1.1E_\mu \cos\theta}{115GeV}} + \frac{0.054}{1 + \frac{1.1E_\mu \cos\theta}{850GeV}} \right] \tag{1.9.}$$

where the two terms represent the contributions of pions and charged kaons, ignoring charm and heavier flavors contribution which start to be significant at very high energies.

In a muon radiography experiment, the flux of incident cosmic muons is utilized to quantify the attenuation caused by the target, it is therefore necessary to give an accurate model of this flux in order to reduce errors in density measurements. A Monte Carlo simulation starting from primary particles and following their interactions up to muon production is one option, another is to use measured fluxes as a reference, or to provide an analytical model for sea-level muon flux, as in the case of the Gaisser's model in eq 1.9.This formula is valid under two conditions: 1) the curvature of the Earth can be neglected ($\theta < 70°$), and 2) muon decay is negligible ($E_\mu > 100/\cos\theta$ GeV) [10]. However, in numerous cases when muon radiography is used, the only useful muon trajectories are near-horizontal, necessitating the employment of an appropriate model for those angles. A new parametrization has been developed to account for the Earth curvature, which is non-negligible at high θ, by replacing θ with a new angle θ^*. The value of $\cos(\theta^*)$ is occasionally computed using a simple geometrical extrapolation, given that the altitude of the initial interaction is known a priori. This approach employs a more difficult extrapolation method given in [20], which demonstrates how $\cos(\theta^*)$ may be recovered from an integral equation by equating interaction length $X(\theta) = X(0)$. In essence, the formula below, borrowed from Reference [20], parameterizes the numerical solution of the integral equation:

$$\cos\theta^* = \sqrt{\frac{\cos\theta^2 + P_1^2 + P_2(\cos\theta)^{P_3} + P_4(\cos\theta)^{P_5}}{1 + P_1^2 + P_2 + P_4}} \tag{1.10.}$$

where $P_1 = 0.102573$, $P_2 = -0.06828$, $P_3 = 0.958633$, $P_4 = 0.0407253$ and $P_5 = 0.817285$. This new parametrizations is included in the modified Gaisser's formula :

$$\Phi_\mu(\theta, E) = 0.14 \left[\frac{E}{GeV} \left(1 + \frac{3.64 GeV}{E(\cos \theta^*)^{1.29}} \right) \right]^{-2.7} \times \left[\frac{1}{1 + \frac{1.1E_\mu \cos \theta^*}{115 GeV}} + \frac{0.054}{1 + \frac{1.1E_\mu \cos \theta^*}{850 GeV}} \right]$$
(1.11.)

which take into account also the low-energy regimes.

1.3.3. Interaction with matter

Muons lose some of their energy when they move through matter, but unlike other particles, they may travel hundreds of meters through rock without being totally absorbed. This feature makes muons excellent for investigating the interiors of large bodies such as volcanoes and pyramids. The interaction of cosmic radiation particles with matter is a key component of studying the characteristics of this radiation and its potential uses. In general, the passage of muon particles through matter is characterized by two main characteristics:

1. Loss of energy by the particle.
2. Deviation of the particle from its incident direction (scattering).

Both of these effects can reveal information about the composition of the crossing material.

1.3.3.1. Energy Loss of Muons

The mean stopping power of a muon in a substance may be expressed as [21,22]:

$$-\frac{dE}{dx} = a(E) + b(E)E$$
(1.12.)

where the first term, $a(E)$, indicates the contribution of the atomic excitation and ionization processes, which are often characterized, for energies not too high (< 100 GeV) where ionization is the dominant energy loss mechanisms for muons, by the Bethe-Bloch relation :

$$-\frac{dE}{dx} = 2\pi N_a r_e^2 m_e c^2 \frac{Z}{A} \frac{z^2}{\beta^2} \left[\ln \left(\frac{2m_e c^2 \beta^2 \gamma^2 W_{max}}{I^2} \right) - 2\beta^2 - \delta - 2\frac{C}{Z} \right]$$
(1.13.)

with :

$2\pi N_a r_e^2 m_e c^2 = 0.1535 MeV cm^2/g$	ρ : density of absorbing material
r_e : classical electron radius	z : charge of incident particle in units of e
m_e : electron mass	
N_a : Avogadro's number	β : v/c of the incident particle
I : mean excitation potential	γ : Lorentz factor $\frac{1}{\sqrt{1-\beta^2}}$
Z : atomic number of absorbing material	δ : density correction
	C : shell correction

A : atomic weight of absorbing material

W_{max} : maximum energy transfer in a single collision.

The maximum energy transfer is that produced by a head-on collision. For an incident particle of mass M, kinematics gives:

$$W_{max} = \frac{2m_e c^2 \eta^2}{1 + 2s\sqrt{1 + \eta^2} + s^2} \tag{1.14.}$$

where $s = m_e/M$ and $\eta = \beta\gamma$. Moreover, if $M \gg m_e$ then $W_{max} \sim 2m_e c^2 \eta^2$.

The Mean Excitation Potential (*I*) is the average orbital frequency $\bar{\nu}$ from Bohr's formula times Planck's constant, $h\bar{\nu}$. It is a logarithmic average of ν weighted by the oscillator strengths of the atomic levels, thus it is really challenging to determine this amount. Nevertheless, it can be parameterized in a variety of ways, such as by selecting a value that applies to all elements, by a straightforward proportionality between I and Z, by semi-empirical formulae that connect I and Z, or even by specialized tables of values for each element [21].

The Shell and Density Corrections these quantities are important to correct the Bethe-Bloch formula at high and low energies respectively.

The second component of eq 1.12, $b(E)$, accounts for the energy loss caused by bremsstrahlung processes, pair production, and nuclear interactions, and can be expanded as the sum of three terms, $b = b_{brems} + b_{pair} + b_{nucl}$. This thesis will not address the reflection of these processes on the muon stopping power law, which has been extensively studied and explicitly determined in [21].

Several muon radiography experiments via absorption employ a common material type called standard rock as a reference to run simulations and analyze muon flux predictions. This hypothetical substance has the density of crystalline quartz ($\rho = 2.65 g/cm^3$), Z and A of 11 and 22, respectively (which is equivalent to sodium), and density effect parameters evaluated on calcium carbonate. Variations in the chemical makeup of the rock, analyzed in [23], can cause significant biases in the muon flux. Aside from the obviously accountable differences in density, the composition of the rock can also impact the muon flux. According to this study, the muon fluxes for each rock below 300 m differ by no more than 2.5% from their individual density-modified standard rock flux. When the target comprises high Z^2/A rocks (such as basalts and limestones) and the rock thicknesses surpass 300 m, the flux differences exceed 2.5%. This corresponds to the point at which radiative losses, whose stopping power contribution is determined by Z^2/A, begin to dominate the energy loss mechanisms. When dealing with basaltic rocks or carbonates with high Z^2/A ratios and thicknesses over 300 m, it is necessary to account for the chemical composition of the rock. These consequences are not yet being analyzed as part of the MURAVES project (discussed in Chapter 3), which is investigating

the density distribution of Mt. Vesuvius.

1.3.3.2. Multiple scattering

Muons, like any other charged particle, lose energy when traversing a medium and can be scattered as a result of the Coulomb interaction. In the case of a single process, diffusion may be represented using Rutherford's formula [24], which played a critical role in understanding the phenomena of alpha particle dispersion through thin sheets of gold, leading to the construction of atomic models predicated on the assumption of a large central core. Due to Rutherford's formula, which states that the chance of having an angular deflection, $P(\Delta\theta)$ is proportional to $1/\sin(\Delta\theta/2)^4$, it is anticipated that the angular deflection will typically be very small, although occasional significant deviations can occur.

Depending on the thickness traversed and the expected average number of individual scattering processes, three alternative possibilities are often distinguished when treating these phenomena [25]:

1. If the thickness is very thin, the possibility that the particle would have more than one large scattering process along its route in the material is minimal, and the phenomena may be represented as a single Rutherford deflection (single scattering).

2. If the thickness is very large, the number of large scattering processes is very high, and the overall energy loss is still small, the phenomenology can be treated statistically to determine the probability of having a given overall deflection using various approximations. Multiple scattering is the term used in a scenario where large scattering events are more then ten and it is the most usually treated condition, even in practical applications.

3. Plural scattering occurs when the thickness has an intermediate value such that the number of individual scattering is of the order of ten. This is a difficult scenario to deal with, because the process cannot be defined by a single interaction or the sum of several interactions. A treatments of this kind of situation has been reported by Keil and collaborators [26].

If the average number of scatterings is high and the energy loss is small, as is typically the case in muographic applications, the distribution of net deflection as a function of thickness may be derived by statistically treating the process, as in Molière's theory [27, 28]. The net scattering distribution may be characterized for many applications using the central limit theorem, which asserts that the total of a large number of distributions, in this case the single Coulomb scatterings, can be approximated by a Gaussian. The Gaussian approximation describes 98% of the actual distribution [10], with a standard deviation that is well approximated across a wide range of Z and for not-very-thin targets by [29]:

$$\sigma_{\Delta\theta} = \frac{13.6 MeV}{\beta c p} z \sqrt{\frac{x}{X_0}} \left[1 + 0.038 \ln \left(\frac{xz^2}{X_0 \beta^2} \right) \right] \qquad (1.15.)$$

where p, c, and z are the particle momentum, velocity, and charge (for the muons $z = 1$), x is the thickness of the scattering medium, and X_0 is the material radiation length, defined as:

$$X_0 = 716.4 g/cm^2 \frac{A}{Z(Z+1) \ln \left(287/\sqrt{Z} \right)} \qquad (1.16.)$$

where Z represents the atomic number and A represents the atomic mass. Several muon radiography applications rely on measuring muon deflections to determine the characteristics of the deflectant material, further information is provided in the following sections.

1.4. Imaging

Numerous researchers have explored the possibility to use cosmic rays to gain insight into a object placed between the source of cosmic rays and a particle detector. This was initially done in 1955, by the Australian physicist Eric George [30] for the computation of tunnel overburden, which may be considered the first tomographic setup in which cosmic rays were utilized as the major signal source. 15 years later, Alvarez et al [31] set another milestone for this method when they search for a hidden chambers in the Pyramid of Khafre in Egypt. The advancement of detector technology, was a significant step forward in the growth of this technique's use. The name "muography" [32, 33] is now used to characterize this imaging approach based on muon detection. This technique involves two imaging methods: muon tomography (muon radiography by multiple scattering) and muon radiography (radiography by absorption), which are used for three-dimensional imaging similar to X-ray tomography and two-dimensional imaging absorption respectively. The following provides a brief overview of these various muography methods.

1.4.1. Muon radiography

Absorption-based muography (AM) takes advantage of the energy loss caused by the ionization and the deflections of muons when they travel through any material, (already discussed in section 1.3.3), and provides insights into their density. The mechanism is quite similar to that of ordinary X-ray radiography, which is used to scan human bodies or small objects, with the difference that the source in muography is natural (cosmic muons), hence the flow cannot be controlled and is not unidirectional. Another significant difference is the nature of muons, which can penetrate hundreds of meters of rock while X-rays cannot survive more than around ten meters. This feature makes muons more

appropriate for scanning larger bodies like volcanoes, pyramids and so on.

The probability for a muon to be absorbed by a given target along a specific line of sight is obtained by comparing the muon flux coming from the different directions within a muon detector's acceptance to the "free-sky" flux, which is the basis of absorption-based muography. This may be expressed explicitly in terms of "opacity" along that line of sight, which is defined as the density integrated over a path length: $O = \int \rho(x)\,dx$. The "meters water equivalent" (mwe) is the opacity unit used, with a conversion factor of $1\,mwe = 100\,g/cm^2$, where the energy loss of an energetic muon is around 0.2 GeV/mwe.

The charged-particle trackers described in section 1.5 are used to rebuild the paths of the observed muons in space using track parameters that are obtained from the collected data. The angles defining the muon arrival direction, which are often shown as a 2D muon angular distribution plot, are calculated using the track parameters. With the AM technique, muon radiography equates to a measurement of transmission, which is the ratio of the flux of muons that reach the detector after passing through the target (measured flux) and a calibration flux, called free sky, measured by taking data in the same conditions but pointing the detector toward the open sky for a certain time. This procedure ensures that geometrical factors and trigger efficiency are in good approximation equal for both datasets. The measured transmission in any given angular region around (α, ϕ) in specific data taking time (Δt), is calculated as [32] [34] [35] [36]:

$$T^m(\alpha, \phi, \rho) = k\,\frac{N^\mu(\alpha, \phi)}{N^{fs}(\alpha, \phi)} = k\,\frac{\int_{E_{min}(\rho)}^{\infty} \phi_\mu(\alpha, \phi, E)\,dE}{\int_{E_{min}^{det}}^{\infty} \phi_\mu(\alpha, \phi, E)\,dE} \qquad (1.17.)$$

where N^μ, N^{fs} represent the number of muons detected after passing the target and from free sky, respectively, and k is the calculated constant :

$$k = \frac{\Delta t_{fs}}{\Delta t_\mu}\,\frac{\epsilon_{DAQ}^\mu}{\epsilon_{DAQ}^{fs}}\,\frac{\epsilon_{an}^\mu}{\epsilon_{an}^{fs}} \qquad (1.18.)$$

where ϵ_{DAQ} and ϵ_{an} represent the data acquisition efficiency and the analysis efficiency.

The minimum detectable energy of muons, denoted as E_{min}^{det}, depends on the specific characteristics of the detector, and E_{min} represents the minimum energy that muons must have in order to cross the target and reach the detector, it can be evaluated by integrating eq. 1.12 [21]. It depends on average target density ρ and on the target thickness seen from the detector in the direction (α, ϕ) and $\phi(\alpha, \phi, E)$ is the differential muon flux with respect to the muon energy E in the given angular region.

Observed transmission must be compared to predicted transmission in order

to assess the density distribution or density anomalies. This predicted transmission value must be calculated using simulations that take into account a realistic muon flux at sea level, precise geometry of the volume of interest from the perspective of the detector, and an estimated average of the volume density. The outcome of this comparison will be a complete 2D average density map distribution.

1.4.2. Muon tomography

This method was proposed for the first time in 2003, is based on multiple Coulomb scattering, which is discussed in section 1.3.3.2. During this process, muons interact with the nuclei of the material, causing them to deviate from their path and decelerate. This technique relies on measuring the deviations of muons as they traverse the target. To implement this approach, detectors are strategically placed to measure muons before and after their interaction with the target, enabling the creation of three-dimensional models depicting the densities of obstructed objects. Muon tomography finds applications in transportation, industrial processes, and nuclear control systems.

Simplifying eq.1.15, the standard deviation of the scattering angle for muon of momentum p can be approximated as follows:

$$\sigma_\theta \sim \frac{13.6MeV}{pc} \sqrt{\frac{x}{X_0}} \tag{1.19.}$$

Here, scattering angles are related to the linear scattering density $\lambda = 1/X_0$ which is approximately the product of the atomic number Z and the density ρ, given by $\lambda \sim Z\rho$ as deduced from eq. 1.16. The eq. 1.19 is derived under the assumption that muons with momentum p are monochromatic and follow a Gaussian distribution. However, cosmic muons are not monochromatic, and their scattering angles are characterized by the following expression:

$$\frac{dN}{d\theta} = \frac{1}{b\sqrt{2\pi x\lambda}} \int_0^\infty p f(p) e^{\frac{-\theta^2 p^2}{2x\lambda b^2}} dp \tag{1.20.}$$

Here, $f(p)$ represents the momentum spectrum and $b = 13.6MeV/c$. The variance of the distribution in eq. 1.20 is given by:

$$\langle \theta^2 \rangle = \lambda x b^2 \langle \frac{1}{p^2} \rangle \tag{1.21.}$$

where the individual unknown momentum is replaced by a fixed value determined from the mean of the distribution of the quantity $1/p^2$.

This equation (eq.1.21) illustrates how the scattering angle variance depends on the material density, emphasizing the need for accurate muon momentum

measurements in certain scenarios where substituting the mean cosmic-ray muon momentum is insufficient for achieving desired results

1.4.3. Applications

Casting its gaze beyond its initial domains, muography has emerged as a versatile and indispensable tool in a myriad of scientific applications. This section delves into the expanding horizons of muography, exploring its diverse applications across different fields. From unraveling the mysteries of volcanic landscapes and ancient civilizations to ensuring nuclear safety and security, muography's capabilities have transcended traditional boundaries. In this section, we venture into the ever-expanding realm of muography applications, showcasing its multifaceted utility and transformative impact on scientific research and geological exploration.

1.4.3.1. Archaeology and cultural heritage

The initial concept was introduced by Luis Alvarez in 1965 [31], when he proposed using cosmic muons to investigate an Egyptian pyramid. A few years earlier, Alvarez had visited the Giza pyramid complex and was struck by the architectural mystery surrounding the Great Pyramid of Khufu and the Pyramid of Khafre. Despite their similar sizes, Khafre's pyramid had a much simpler design, even more so than the tomb of Khufu's great-grandfather, Sneferu, during whose reign there had been architectural experimentation and increasing pyramid complexity.

Alvarez's curiosity about whether hidden chambers might exist within Khafre's pyramid was not widely shared among archaeologists, as they recognized that architectural evolution and family dynamics do not follow linear paths. Nonetheless, driven by the spirit of exploration, Alvarez was intrigued by the possibility of uncovering hidden secrets. Thus, in 1966, the Joint Pyramid Project, led by Alvarez, was formally launched. The team created a detector based on spark chambers, a common tool in particle physics experiments at the time, and placed it in the known large chamber at the base of Khafre's pyramid. Unfortunately, no secret chamber was discovered during this endeavor [31].

Building upon the legacy of Alvarez, a research cohort from the National Autonomous University of Mexico (UNAM) embraced a similar mission in the year 2000. Their objective was to delve into the inner sanctum of the Sun Pyramid located in Teotihuacan, Mexico [37, 38]. This pyramid, ranking as the world's third-largest, was constructed by the Aztecs in the 14th century. The team employed a detector based on multi-wire chambers for their exploration. Following nearly a decade of dedicated experimentation, their most significant discovery was the revelation of a region within the pyramid characterized by lower density. This region intriguingly assumed the form of an equilateral

triangle, with each side measuring an impressive 60 meters [38].

In 2015, the ScanPyramids project [39] revived interest in muography within the context of Egyptian archaeological investigations. This project harnessed a combination of non-invasive methods to scrutinize Old Kingdom pyramids, aiming to unveil hidden voids and architectural features. The pinnacle of this undertaking was the discovery, in 2016, of an unexpectedly expansive void within the Great Pyramid of Giza [40]. Remarkably, this void bore a striking resemblance to the cross-section of the Grand Gallery and spanned a minimum of 30 meters (Figure 1.4). The data collection process encompassed the utilization of nuclear emulsions, scintillator-based telescopes situated in the Queen's chamber, and gaseous detectors positioned outside the pyramid. All three investigative teams, upon separate data analyses, concurred on the discernment of an augmented muon flux originating from the same spatial locus. Statistical significance far exceeded 5 standard deviations from the null hypothesis positing the absence of a void. This discovery was further substantiated by the observed excess of muons within the angular region corresponding to the Grand Gallery. Subsequent data collection efforts have aimed to characterize the void, leading to the recent revelation that its shape aligns with a corridor-like structure measuring approximately 9 meters in length with a transverse section of about 2 m by 2 m [41]. The incorporation of ground-penetrating radar (GPR) and ultrasonic testing since 2020 has bolstered confidence in the robustness of these findings [42]. Figure 1.5 illustrates the outcomes of the analysis performed on the nuclear emulsion films placed in the al-Ma'mun Corridor. It displays the angular distribution of the observed muon flux divided by the flux derived from the Monte Carlo simulation using Geant4. The simulation was based on the determined azimuthal angle from the analysis and the 3D model, excluding the descending corridor (DC) structure. The normalization of the simulation to the observation in terms of muon flux followed the same procedure used for the analysis of the DC in the area outside the North Face Corridor (NFC), excluding the Chevron region (CH) [41].

In the depths of Mt. Echia in Naples, Italy, another intriguing archaeological discovery unfolded [43,44]. This historic site, marking the city's ancient origins dating back to the 8th century BC, is perched atop a headland, reaching a peak elevation of around 60 m above sea level. Composed primarily of soft yellow tuff, a volcanic rock, Mt. Echia harbors a complex network of subterranean passages and chambers, shaped and utilized over centuries. Notably, the renowned Bourbon Tunnel, excavated in the mid-19th century, is part of this intricate underground landscape. The initial hints of an enigmatic cavity were unveiled through a 26-day preliminary study conducted

---

(★) EM5, EM6H, EM6T, and EM7 denote the designations of the nuclear emulsion film detectors placed within the al-Ma'mun Corridor.
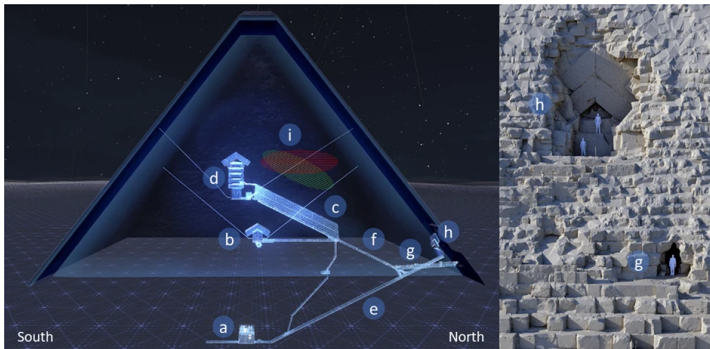
Figure 1.4. ┃ (a) Subterranean chamber, (b) queen's chamber, (c) grand gallery, (d) king's chamber, (e) descending corridor, (f) ascending corridor, (g) al-Ma'mun corridor, (h) north face Chevron area, (i) ScanPyramids Big Void with horizontal hypothesis (red hatching) and inclined hypothesis (green hatching) as published in November 2017 [40].

with the MU-RAY telescope [45], positioned within the Bourbon Tunnel and subjected to an approximately 40-meter rock cover [43]. This telescope, typically employed with horizontal orientation for volcanological research, was adapted for this archaeological inquiry, featuring a vertical orientation and reduced spacing between its detection planes. Further investigation ensued through a meticulous second phase, chronicled in Reference [44]. In this stage, the MU-RAY detector captured data from an alternative vantage point, complemented by the observations of the portable MIMA telescope [46] from a third location. What makes this discovery especially intriguing is the site's rich historical significance as the ancient nucleus of Naples. Unraveling the secrets buried deep within Mt. Echia not only enriches our understanding of the city's past but also highlights the adaptability and precision of muon radiography technology in uncovering hidden archaeological marvels.

1.4.3.2. Volcanology

Following L.W. Alvarez's pioneering experiment, the technology has been updated and adapted to volcanological applications. If the volcano's normal thicknesses are not prohibitive ($< 1000m$), muon radiography, in conjunction with standard geophysical approaches, can be a valuable aid in identifying the volcano's various eruptive modes. Muography is independent of the geophysical model and directly measures density length. If the path length is estimated using topographic information, the measurement yields the average density of cosmic-ray muons along the path line.

The presence of less dense or more dense places can be identified by monitoring the muon absorption rate. Furthermore, in some circumstances, muography may provide real-time signs of prospective structural changes, such as magma
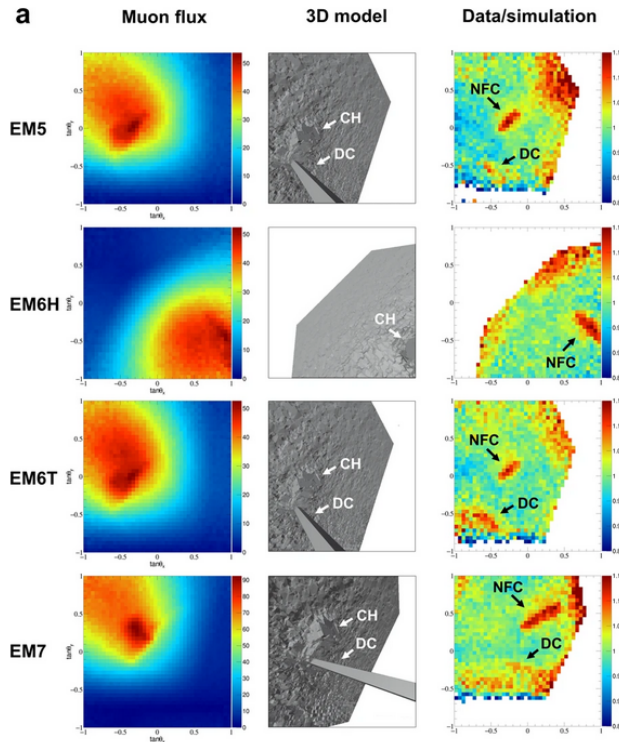
Figure 1.5. | Two-dimensional angular distribution for EM5 to EM7.[(★)]From left to right: observed muon flux (tracks/cm^2/day/sr), 3D model, ratio of muon flux of the data to simulation. Adapted from [41]

rise, which might be antecedents of a new eruption. A Japanese group of scientists suggested the use of muography to scan the body of a volcano for the first time in 1994 [47]. The plan was to employ a simple tracking device constructed of plastic scintillator bars to detect muon flux around Mt. Tsukuba.

The method was revealed to be capable of determining the internal structure of a volcano in greater detail than normal geophysical approaches. In the years after this pioneering work at Mt. Tsukuba, several volcanoes in Japan have been studied using muon radiography. The results obtained at Mt. Asama using Emulsion Cloud Chamber (ECC) detectors are described in [48], and they are among the earliest examples of the use of muography in volcanological applications. Because magma mobility in a conduit precedes eruptive processes, visualizing magma dynamics is often required to understand eruption patterns. Muon radiography measurements revealed evidence of magma movements in a volcanic conduit for the first time in 2013, as discussed in [49]. This result highlights the potential of muon radiography as a method for detecting

eruption clues. The experiment was conducted in Japan at the Satsuma-Iwojima volcano. Due to the low intensity of cosmic ray muon flux, lengthy acquisition exposures are necessary to achieve appropriate muon transmission image contrast. The system also requires sufficient temporal resolution to enable quick time sequence radiography. Figure 1.6 represents the time sequential muographic images showing the ascent and descent of the top of the magma column and its convection process, which synchronized with the timing when volcanic glow was observed during this eruption period.
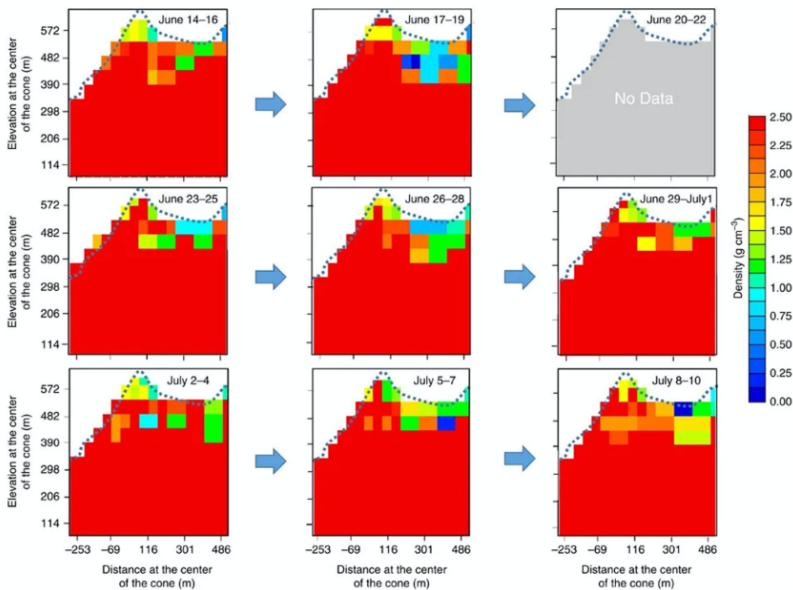
Figure 1.6. ❘ The dynamics of magma during the Satsuma-Iwojima eruption are illustrated in the diagrams. These visual representations depict the angular distribution of the upper limit of the average density along the muon path at a 1σ (68% Confidence Level). The frame rate consists of 10 frames per month. It's important to note that data collection was interrupted from June 20 to 22 due to a blackout. To enhance statistical precision, two horizontally adjacent bins were combined. The figures also provide information on the elevation and horizontal distances from the center of the cone. From [50].

In parallel, European research groups adopted muon radiography for volcano investigations. Two independent groups in France investigated the technique's suitability by applying it to two different targets: the La Soufriere de Guadeloupe, an explosive subduction volcano in the Lesser Antilles with one of the world's most dangerous volcanic hydrothermal systems, and the Puy de Dome,

an extinct volcano with an altitude of 1465 m a.s.l. and a lateral extension of more than 2 km at the base. Even though the last one may not appear to be of great interest for a geological investigation, it has been chosen as a test site for the development of muon radiography by the TOMUVOL and MU-RAY collaborations [51] based on two different technologies because it is isolated, so there is no muon absorption from other structures, the size is moderate enough to allow measurements of a large part of the edifice, and it can be observed from many locations, most of which have infrastructure reachable by roads and served by electricity. Moreover, it has been already studied with other techniques, whose data can be used to validate muography.

The DIAPHANE team studied La Soufrière de Guadeloupe using a plastic scintillator-based detector (see section 1.5) with three XY planes of $50 \times 50 cm^2$ area. Volcano density structures have typically been researched using gravity measurements, but 3-D models based purely on these data are extremely non-unique and have poor resolution, especially given how difficult it is to get excellent data coverage in the field. The DIAPHANE collaboration created the 3D picture by inverting gravity data and muon data together. The muographic data are made up of three independent observations obtained from three telescopes at the same time. The combination of gravimetric and muographic data provided for better resolution than gravity or muon data alone [52].

This collaborative effort demonstrated muon radiography's capability to detect and describe mass movements in the shallow hydrothermal systems of low-energy active volcanoes.

Italy, home to numerous hazardous and active volcanoes, also became a focal point for muon radiography. One such example is Mt. Etna, a particularly active stratovolcano on the island of Sicily, which may produce eruptions from any of its four summit craters as well as from vents or fissures. Its height is around 3350 m, while the base has a circumference of 40 km. Due to its frequent activities, its flanks were not heavily urbanized. A telescope with two detection planes, each with 16 X and 16 Y scintillator strips, was used to study Mount Etna using muon radiography for the first time in 2010 [53]. The primary goal of this first activity was to evaluate the feasibility of using a double-plane telescope while avoiding excessive background. They discovered a significant bias in the measured flux due to fake muon tracks. This background is created by low-energy particles that, by accident, hit the telescope's two planes at the same time. Because of this circumstance, a telescope with more than two planes is required in order to prevent the contamination of real tracks with fake ones. However, an approximate estimate of the chance of having these accidental tracks has been examined, and the result is consistent with the actual measurement. Despite the large quantity of background in the measurement, which is incompatible with an accurate calculation of the density distribution

inside the volcano, an evidence of a reduced opacity zone was exhibited once the background was subtracted, as anticipated by the synthetic model.

In 2019, Stromboli, a prominent Italian stratovolcano within the Aeolian archipelago, unveiled its internal structure through muon radiography, employing nuclear emulsion films [54](discussed in detail in the detector section 1.5). The observational campaign commenced on October 22, 2011, and concluded on March 24, 2012, spanning approximately five winter months. Within the crater zone, the experiment unveiled a notable surplus of muons compared to the anticipated flow. In comparison to the bedrock, this surplus corresponds to a 30–40% reduction in density, as illustrated in Figure 1.7. The precision of density estimation within the anomaly region carries an estimated uncertainty of 18%, comprising two primary components: 10% attributed to statistical factors and 15% to systematic factors. Systematic uncertainties encompass several considerations, including the modeling of the low-momentum segment of the muon spectrum, the precision constraints of the digital elevation model (limited to 10 m), and the accuracy of angular alignment between Monte Carlo simulations and actual data.
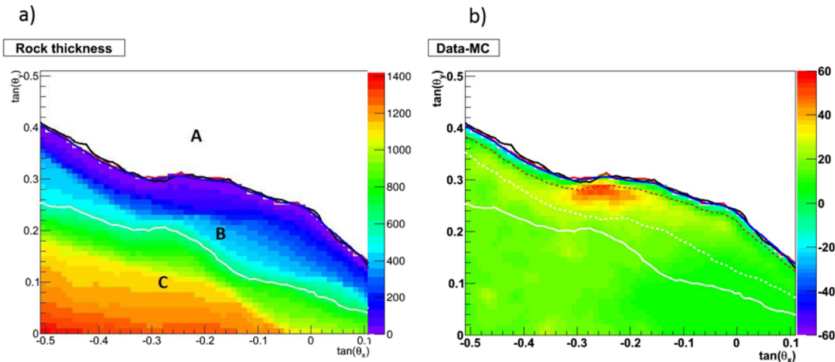
Figure 1.7. ┃ (a) Visualization of rock thickness and the Stromboli's crater profile captured by the emulsion detector. The color scale illustrates rock thickness in meters.(b) Representation of the discrepancy between the observed muon flux and the flux predicted by Monte Carlo simulation within an angular range centered on the crater region. The color scale indicates muon counts. Variables θ_x and θ_y represent azimuthal and elevation angles, respectively. "Region A" corresponds to the open sky, while "Regions B and C," separated by a white line (indicating the sensitivity limit based on Monte Carlo simulations assuming zero background), define the accessible muography area and the "deep rock" region (unreachable by muography). The sensitivity limit corresponds to an anticipated flux of 2.3 muons (90% confidence level, assuming zero background) per $20{\times}20$ $mrad^2$ bin (equivalent to approximately 10×10 m² projected at the crater). Reproduced from [54].

Notably, the systematic component becomes dominant beyond the threshold

marked by the red dashed line in Figure 1.7(b), representing a rock thickness of 40 m. Conversely, below the white dashed line, statistical uncertainty takes precedence. The continuous white line serves as a reference, indicating the statistical sensitivity limit derived from Monte Carlo simulations conducted in the absence of background contamination. These findings hold particular significance in the realms of geophysics and hazard assessment, offering valuable insights into the structural characteristics of this specific segment of the volcanic formation.

Finally, in light of extensive urbanization in the region and its status as one of the world's most hazardous volcanoes, Mt. Vesuvius became a subject of intense scrutiny. The surrounding 'red zone', designated as a high-risk region where evacuation might be required in case of an eruption, is home to approximately half a million people. Since the last effusive eruption in 1944, there has been relative calm; nonetheless, a potential fresh eruption might be quite damaging for the neighboring population centers. Due to this risk, Mt. Vesuvius is the subject of a thorough examination and surveillance. The Italian National Institute of Nuclear Physics (INFN) provided funding for a research and development initiative on muon radiography that was specifically used to examine Vesuvius between 2009 and 2012. The Italian National Institute of Geophysics and Volcanology (INGV) collaborated in the development of the MU-RAY and MU-RAY2 prototypes ($1m^2$ of active area), which were tested on Mount Vesuvius. Based on the lessons learned from the MU-RAY project, the Italian Ministry of Research and Education has sponsored the MURAVES experiment. The experiment has been collecting data since the first of the three hodoscopes was set up there in the summer of 2019. This thesis emphasizes the MURAVES simulation chain, with comprehensive details provided in Chapter 3.

1.4.3.3. Nuclear safety and security

In the realm of both absorption and multiple scattering approaches, significant applications with implications for industry and security have been developed or are in planning stages. One such application involves monitoring blast furnaces. The Mu-Blast project, funded by the EU [55], explored muon tomography's potential to provide insights into the distribution of crucial components within a blast furnace, like coke and burden, during its operational phases. Analysis of scattering, particularly the determination of linear scattering density (LSD) for different materials, enables discrimination and highlights distinct material distribution within the furnace body. While simulation studies have indicated the potential for generating informative images with full detector coverage, deploying large-scale detectors in challenging environments, such as near a furnace, presents significant logistical challenges.

A more practical arrangement involved simulating a pair of detectors, positioned on opposing sides of the blast furnace. These results emphasized the need to measure individual particle momenta to generate usable images of the furnace interior. Developments in designing and constructing detectors capable of measuring muon momenta have shown promise in obtaining meaningful images within approximately 8 hours. Building upon the Mu-Blast project, the EU-sponsored BLEMAB (Blast furnace stack density Estimation using online Muons Absorption measurements) project [56], initiated in 2020, seeks to further explore the imaging potential of blast furnace inner zones using a muon absorption detector designed for blast furnace. The project employs muon detectors made of three independent 80 cm × 80 cm tracking modules, measuring two coordinates of muon impact points along orthogonal axes (XY). This innovative tracking technology, similar to the one used in the MURAVES and MIMA [46] projects, enables BLEMAB to achieve exceptional accuracy in capturing muon trajectories and interactions within the furnace [57].

Another valuable industrial application of muon scattering tomography relates to transportation and nuclear control. Specifically, this technology is instrumental in combating nuclear smuggling by inspecting vehicles and containers for potential heavy metal contents. The Los Alamos group introduced and commercialized this approach, deploying portals for muon tomography transport control utilizing drift tube technology [58].

Illustrated in Figure 1.8 and 1.9, a portal developed by Decision Sciences can scan entire vehicles, detecting material irregularities. In the context of transport control, the Mu-Steel European project [59] devised a methodology for identifying potential radioactive sources within containers transporting scrap metal. Radiation portals, usually installed at foundry entrances, might miss sources concealed within heavy metal shipping casks, such as those made of lead. Consequently, melting the source could have detrimental effects. Mu-Steel's results have demonstrated that a muon tomography system, when combined with radiation detectors, can effectively identify radioactive sources within a timeframe consistent with truck flow, typically within a 5-minute scanning period.

1.5. Detectors for muography application

In the realm of muography, particle detectors must fulfill a diverse set of criteria, often different from those applicable in mainstream particle physics. Primarily, a muography particle detector must demonstrate robustness, enabling remote operation with minimal human intervention. Depending on the deployment context, power consumption can become a crucial consideration. Fortunately, the inherently low event rate implies that data rate and the speed of data acquisition (DAQ) and front-end (FE) electronics typically do not pose critical

Figure 1.8. ❘ large area detectors of Decision Sciences for the scanning of commercial trucks. Reproduced from [58].
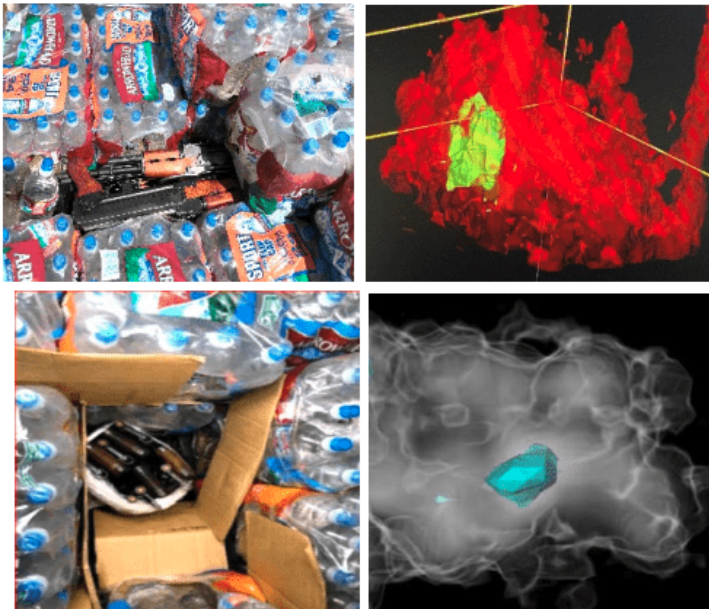

Figure 1.9. ❘ Concealed weapons are hidden behind a shield of bottled water and their clear images were obtained using the Discovery® scanning system. Reproduced from [58].

bottlenecks. It is essential to recognize that various muographic applications require different detector geometries and employ distinct detection technologies. Consequently, a wide variety of muon detectors have emerged over the past few decades, often sharing limited commonalities. A notable shared limitation across these detectors is the inability to measure muon momentum on an individual basis, despite the significant desirability and potential significance of such an advancement in muography. In contexts where the detector system is tailored for Scattering Muography (SM), precise reconstruction of
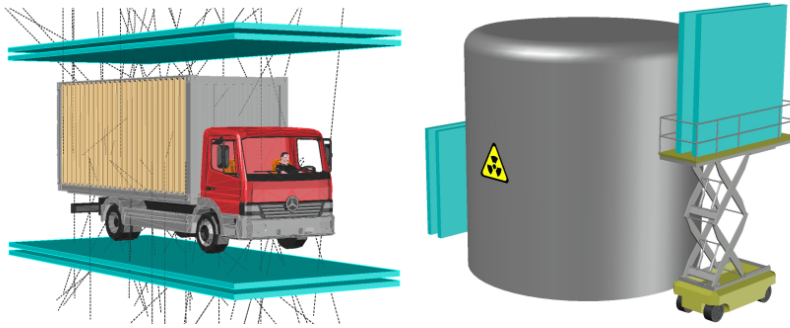
Figure 1.10. | Detector geometry depends on the application, left: cargo inspection, right: nuclear storage inspection. From [32].

the muon trajectory is of paramount importance, often requiring a resolution of 1 milliradian (mrad) or higher both before and after the muon traverses the target of interest. A typical detector configuration, as illustrated in Figure 1.10 (left), includes two tracking systems positioned both above (upstream) and below (downstream) the target. This setup leverages the augmented muon flux from the zenith, effectively reducing data acquisition duration. However, it is crucial to acknowledge that the optimal geometry may vary depending on specific application scenarios (see Figure 1.10). Due to the inherent limitations associated with such setups, the detectors tend to have substantial dimensions, ranging from 2 to 10 m^2, to optimize muon acceptance. In scenarios where
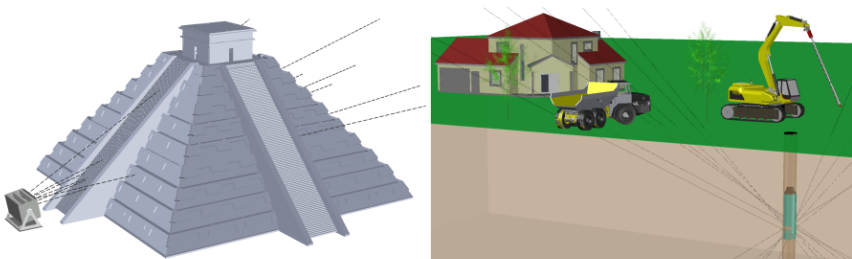
Figure 1.11. | The geometry of the detector in absorption muography depends on the application, left: scan of a large open-air structure (e.g. a pyramid), right: borehole application for underground imaging. From [32].

Absorption Muography (AM) is adopted, such as for imaging expansive man-made structures ($\sim$ 10 to 100 m^2) or exceptionally vast entities like volcanoes, a relatively more compact detector ($\sim$ 1 to 2 m^2) can be placed laterally to the target, as depicted in Figure 1.11 (left). This common detector configuration resembles a "muon telescope," comprising position-sensitive layers situated at a defined distance from the target. Since quantifying multiple scattering angles

is not the primary objective, the angular resolution may be limited to 10 mrad or more. Given a predefined X-Y spatial resolution for a single detection plane, the angular resolution of a telescope primarily depends on the separation distance between the first and last plane. A greater interplane distance enhances angular resolution but simultaneously reduces the telescope's acceptance.

In situations requiring muography of an underground target, the telescope geometry can be effectively deployed only if sufficiently spacious tunnels exist beneath the target. In scenarios where such tunnels are unavailable, and considering the significant financial investment associated with subterranean drilling or excavation, cylindrical detectors specifically designed for Absorption Muography have been proposed and concretely realized [60]. These detectors can be inserted into boreholes, as illustrated in Figure 1.11 (right), where safety concerns preventing the use of gaseous detectors in such instances.

The following subsection will explore distinct muography detectors, distinguished based on their respective detection mechanisms.

1.5.1. Nuclear emulsion detectors

The journey of nuclear emulsion detectors in the realm of particle physics traces back to Becquerel's serendipitous discovery in 1896 when radiation emissions from uranium ores left imprints on photographic plates [61]. This discovery sparked the evolution of nuclear emulsions as radiation detectors, initially based on photographic plates. Over the years, these detectors underwent substantial refinement, particularly in their sensitivity to minimum ionizing particles. A pivotal moment arrived in 1947 when Lattes and colleagues identified pions in cosmic rays at high altitudes [4], showcasing the detector's prowess in particle identification. These breakthroughs highlighted the detectors versatility and sensitivity, propelling their significance in scientific explorations. As the applications expanded, Niwa and collaborators in 1974 introduced an automated nuclear emulsion scanning system [62]. This innovation allowed for the efficient analysis of a large number of events recorded on nuclear emulsions. These developments underscore the detectors versatility and sensitivity, paving the way for their crucial role in scientific explorations. The CHORUS experiment [63] followed by the OPERA experiment [64] stands out as a pivotal milestone, using nuclear emulsions in neutrino experiments and inspiring subsequent advancements in muography applications [40, 54, 65], where Figure 1.12 shows the impressive improvement of nuclear emulsion technologies results, specially for analyzing speed through technical development for past particles discovery and recent muography. The technology behind nuclear emulsions, while reminiscent of photographic emulsions, is distinctly specialized. These detectors, typically consisting of silver bromide crystals dispersed in a gel, operate by ionizing particles sensitizing the crystals they pass through, creating a latent
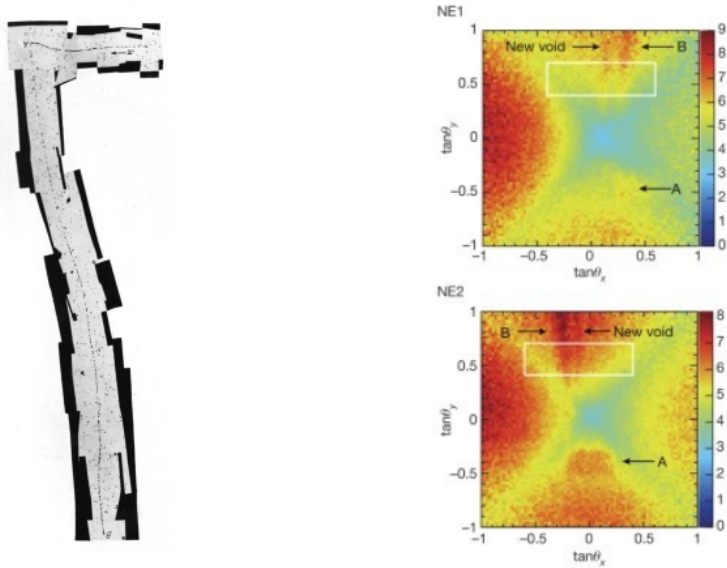
Figure 1.12. | Left: Photomicrographs of one example of pion decay into muon taken from [4], Right : Muograph of the Khufu pyramid obtained by using nuclear emulsion detector (A: King's chamber, B: Grand Gallery), adapted from [40].

image. During the development process, metallic silver coalesces onto the sensitized sites, forming grains visible under transmitted light. These grains align along the particle's path, providing nuclear emulsions with inherent 3D tracking capabilities and sub-micrometric precision, unmatched by other detection technologies.

However, nuclear emulsions are sensitive not only during exposure but also throughout their journey, susceptible to thermal effects, humidity, and chemical reactants. The structure of detectors based on nuclear emulsions is modular, with films rarely exceeding 1 m per dimension. To achieve high statistics, large-scale applications require at least 1 m^2 of detectors, with ongoing efforts to construct larger detectors spanning 10 m^2 and 100 m^2. Stacking films enhances angular precision, allowing for precise particle identification and kinematic measurements. Addressing the detectors sensitivity, careful handling is crucial, especially during transportation and removal, as nuclear emulsions retain tracks until developed. Background noise remains a challenge during muographic exposures, demanding active efforts to differentiate genuine signals from instrumental and physical backgrounds. Despite these challenges, nuclear emulsion detectors stand out for their cost-effectiveness, typically priced at a few euros per film, and their independence from power supplies, making

them ideal for long-term campaigns in remote locations. These detectors, with their ability to record charged particle trajectories in three dimensions with sub-micron spatial resolution, continue to shape the landscape of particle physics, leaving an indelible mark on scientific exploration.

1.5.2. Scintillation detectors

The scintillation detector stands as a cornerstone in modern nuclear and particle physics, offering a reliable method for detecting charged particles and radiation. Its principle lies in the phenomenon of scintillation, where certain materials emit a flash of light upon interaction with nuclear particles or radiation. Initially demonstrated in the early 20th century with devices like Crookes' spinthariscope [66], scintillators experienced a resurgence in 1944 when Curran and Baker replaced human observation with photomultiplier tubes, marking the birth of the modern electronic scintillation detector [22]. One notable application is in muon imaging, where plastic scintillators have gained prominence. These scintillators, known for their rapid response, adaptability, and ease of use, are ideal for muon tracking due to their sturdy construction. When a muon traverses scintillator materials, these materials exhibit luminescence —an ability to absorb energy and subsequently emit it as visible light. In instances where reemission occurs almost instantaneously, typically within 10^{-8}s (reflecting the time for atomic transitions), it's termed fluorescence. Conversely, delayed reemission due to a metastable excited state is known as phosphorescence or afterglow. This light, detected and converted into electrical pulses by a photomultiplier, provides crucial data about the incident muon. Plastic scintillators, with their ability to be molded into various shapes, are especially suited for applications where spatial resolution is not the primary concern, making them valuable tools in muography experiments [40, 46, 67, 68].

In the domain of scintillation-based detection, a noteworthy example is the MURAVES detector, a subject we will thoroughly examine in MURAVES chapter. This exploration will offer in-depth insights into its applications in muography. Furthermore, in subsequent RPC chapter, we will delve into the section on external trigger (section 4.3), providing a detailed showcase of our methodologies in working with these detectors.

1.5.3. Gaseous detectors

In muography, diverse gaseous detectors have been chosen for various applications. This section offers brief descriptions of a few selected types.

1.5.3.1. Multi-Wire Proportional Chamber

In 1968, George Charpak introduced a revolutionary particle detector: the Multi-Wire Proportional Chamber (MWPC) [69] and earned the Nobel Prize

for this invention in 1992. This innovation marked a significant milestone in particle detection technology, owing to its exceptional precision in identifying particle positions and its ability to measure rates that surpassed all previous devices. The MWPC [70] consists of a gas-filled enclosure with an anode wire plane and two cathode planes, which can be constructed using wires, strips, or pads. To accurately determine the avalanche position in two dimensions, it's crucial for at least one cathode wire or strip to be perpendicular to the anode wire plane. When a charged particle passes through the detector volume, it generates primary electrons in its path. These electrons then move towards the anode plane, where the strength of the electric field is inversely proportional to the distance from the wire. As a result, multiplication occurs within regions just tens of microns around the wire. Signals are detected not only from the wires but also from the nearby cathode strips due to capacitive coupling.

However, a new generation of detectors known as Micro-Pattern Gaseous Detectors (MPGDs), has been developed. These detectors are manufactured using advanced microelectronics techniques, ensuring precise gaps and strips down to a few microns. MPGDs are highly regarded for their exceptional spatial resolution, timing response, energy resolution, rate handling capacity, and resistance to radiation. For a practical application of MWPC in muography, you can refer to the source provided in reference [71].

1.5.3.2. Drift Chambers

A drift chamber serves as a precise particle tracking device, determining the spatial position of a ionizing particle based on the time it takes for ionization electrons to drift through a gas [72]. These detectors rely on measuring the time it takes for electrons, produced when an incident muon interacts with an active gas mixture, to reach a high-voltage anode wire. Achieving this involves a series of cathode strips kept at high voltage, creating a drift field between two printed circuit boards (PCBs). The anode wire generates a signal in response to these drifting electrons, which is then captured by the system's electronics and directed by the electromagnetic field.

To establish a single three-dimensional track point, two perpendicular detectors are necessary, as drift chambers measure the interaction location in one dimension. The importance of drift chambers in muon scattering tomography is evident in the array of research efforts cited in the subsequent references [73–75], highlighting the widespread adoption of these chambers by various research groups.

1.5.3.3. Micro-MEsh GASeous structure (Micromegas)

Micromegas detectors, as documented in the reference [76], stand out as intricate yet highly effective parallel plate structures. Positioned a few hundred

microns above the anode, a delicate micromesh partitions these detectors into two essential domains: the drift gap and the amplification gap. Within the amplification gap, an intense electric field reigns, making it a zone of critical importance. Here, primary waves generated in the drift region trigger a cascading avalanche effect, a phenomenon crucial for particle detection accuracy. Notably, the compact dimensions of the amplification gap minimize the disruptive impact of space charge, ensuring precise and reliable tracking of particles' paths. One notable observation involves a subtle bending of the micromesh toward the anode plane. This phenomenon arises due to the strong electric field within the detector. To optimize performance, additional gaps are strategically integrated, addressing potential dead areas and enhancing overall efficiency. Furthermore, stringent precautions are taken to prevent discharges, safeguarding the integrity of the anode and the entire electronic system. For a practical illustration of the application of Micromegas detectors in muography, consult the provided example in references [40, 77].

1.5.3.4. Gas Electron Multiplier (GEM)

The Gas Electron Multiplier (GEM) detector comprises a thin polyamide foil sandwiched between metal layers, typically copper, on both sides, featuring a dense array of holes, typically 50–100 per mm^2. Application of high voltage across these sides prompts primary electrons to generate cascades within the holes. Subsequently, a significant portion of secondary electrons moves to the opposite side, while ions are predominantly collected by the upper metal layer. The movement of these transferred electrons induces a signal on copper-based readout elements (strips or pixels) situated a few millimeters away from the foil on a printed circuit board [78]. Similar to the Micromega detector, their primary advantage lies in their production through microelectronic technology. This process allows for high granularity, providing excellent 2D position resolution, often reaching as fine as 20–40 μm —an achievement challenging to attain with conventional detectors. The reduced distance between the anode and cathode electrodes, sometimes even as low as 50 μm, significantly lowers the required operating voltages compared to traditional detectors. However, the narrow gap between electrodes and the fine electrode structures makes them electrically fragile, and they can be easily damaged during occasional breakdowns. These detectors serve as trackers in muon tomography applications. For practical examples of their application, refer to [79–81].

1.5.3.5. Resistive Plate Chamber

Resistive Plate Chambers (RPCs) are efficient and cost-effective gaseous detectors commonly used in high-energy physics experiments. The active detection component of a RPC is the gas contained in a thin gap between two parallel

plates of high resistivity. A semi-conductive coating is applied to the exterior surface of each plate, allowing the application of a high voltage to generate a uniform electric field across this volume. When a charged particle passes through the gap, gas molecules along its path are ionized, releasing free electrons that are accelerated towards the electrode. The collisions of those electrons in the gas itself lead to a multiplication of the electrons causing an avalanche. This charge motion induces an electrical signal on metallic strips used as electrodes that are read out individually. RPCs offer excellent time resolution, making them suitable for high-rate experiments in particle accelerators. In addition to high-energy physics, RPCs find applications in muography [82, 83]. A lot of work on this thesis is based on RPC detectors. Proper description about RPC is included in Chapter 4.

2. Chapter

Monte Carlo Simulations

In this chapter, we delve into a detailed Monte Carlo simulation, encompassing the entire process from cosmic muon generation, their passage through the object of interest, to the intricate details of detector response.

2.1. Cosmic-ray muon generation

In the realm of muography applications, the first crucial simulation step involves generating muons and background particles, such as electrons, positrons, and hadrons, utilizing realistic models. In this section, a detailed examination and comparison of three Monte Carlo tools—CRY [84], CORSIKA [85], and EcoMug [86]—will be conducted.

2.1.1. COsmic Ray SImulation for KAscade (CORSIKA)

CORSIKA [85] stands out as a prominent cosmic-ray air shower (CRAS) generator, simulating the complete cascade of secondary particles initiated by primary cosmic rays. This Monte Carlo toolkit is crafted to replicate the development of Extensive Air Showers (EAS) in the atmosphere, whether initiated by photons, protons, nuclei, or other primary particles. CORSIKA meticulously tracks all particles until their interactions, decay, or absorption. Hadronic interactions are modeled using various reaction frameworks like EPOS-LHC, SIBYLL, and QGSJET-II for high energies, and GHEISHA and UrQMD for lower energies. Electromagnetic interactions offer a choice between the EGS4 shower program [87] or analytical NKG formulas [88].

CORSIKA's computational demands can be substantial due to its detailed simulation of EAS evolution. Despite its indispensable role in numerous cosmic-ray, gamma-ray, and neutrino astronomy experiments over the past three decades [89], its implementation in FORTRAN 77 presents limitations, including memory management and lack of object orientation. To address these constraints, ongoing efforts are directed towards rewriting the entire code. Version 8, currently in progress, is being developed using modern languages such as C++ and Python [90].

While CORSIKA provides an exhaustive simulation of EAS evolution, its computational intensity has led to the development of alternative tools like CRY an EcoMug, as discussed below.

2.1.2. Cosmic-RaY shower generator (CRY)

Among the Monte Carlo programs capable of simulating sea-level cosmic ray muons, CRY emerges as one of the most widely employed in practical applications. Notably, it diverges from CORSIKA by utilizing precomputed input tables, generated through extensive MCNPX [91] simulations of protons within the energy range of 1 GeV–100 TeV, introduced at the upper atmosphere levels. In this approach, the primary cosmic ray is generated following the empirical formula outlined by Papini et al. [92], accounting for solar modulation, latitude-dependent geomagnetic cut-off, and altitude variations. The atmospheric conditions are based on the 1976 US atmosphere model, although the model assumes a flat atmosphere, neglecting the curvature's impact on cosmic ray attenuation before reaching sea level, as highlighted by [84].

Moreover, users have the flexibility to generate particle showers from flat surface at three distinct elevations (sea level, 2100 m, and 11300 m) and have control over geomagnetic cutoff and solar cycle effects. However, while CRY offers enhanced computational performance over CORSIKA, it does introduce certain approximations such as restricting the simulation to protons as cosmic primaries, operating within a limited energy range, and employing a simplified atmospheric model.

2.1.3. Efficient COsmic MUon Generator (EcoMug)

EcoMug stands out as a parametric generator, offering the flexibility to generate cosmic muons based on user-defined parametrizations of their differential flux. A default parametrization is available, derived from data collected during the ADAMO experiment [93]. Unlike many cosmic-particle generators like CRY and CORSIKA, which are constrained to flat generation surfaces, EcoMug expands the possibilities. It enables muon generation not only from flat surfaces but also from cylindrical and hemispherical surfaces dependant on the detector configuration and application (see Figure 2.2). This feature ensures accurate angular and momentum distributions while maintaining a remarkable speed in the simulation process [86].

2.1.4. Generator Comparaison

We evaluated and compared the three Monte Carlo tools: CRY [84], CORSIKA [85], and EcoMug [86].

Figure 2.1 [94] illustrates the muon flux as a function of kinetic energy for CRY and five different combinations of low and high-energy hadronic interaction models available in CORSIKA, covering the range from 1 MeV to 10 TeV. We observed general agreement in peak positions and overall shapes, although there was a certain spread in predictions at high energies and at the maximum.
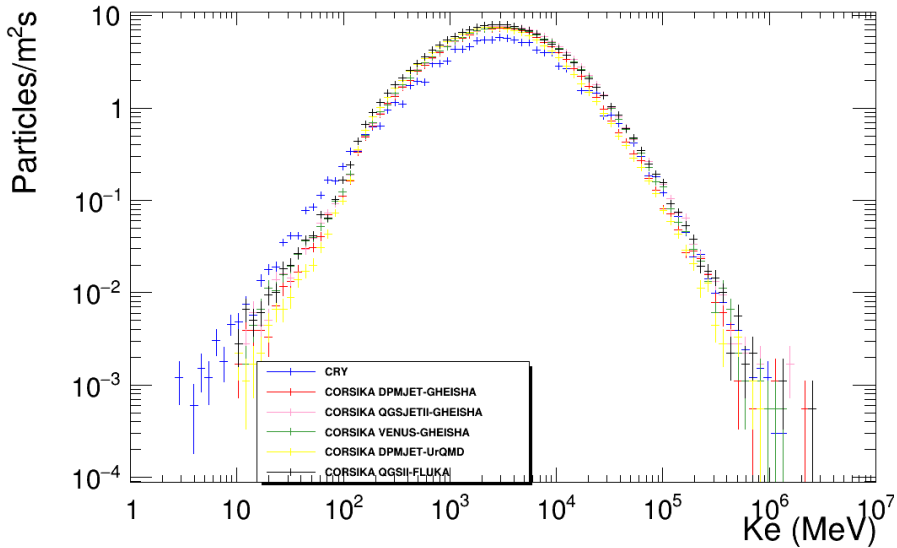
Figure 2.1. | Muon energy distribution obtained through CRY and five different hadronic interaction models in CORSIKA [94].
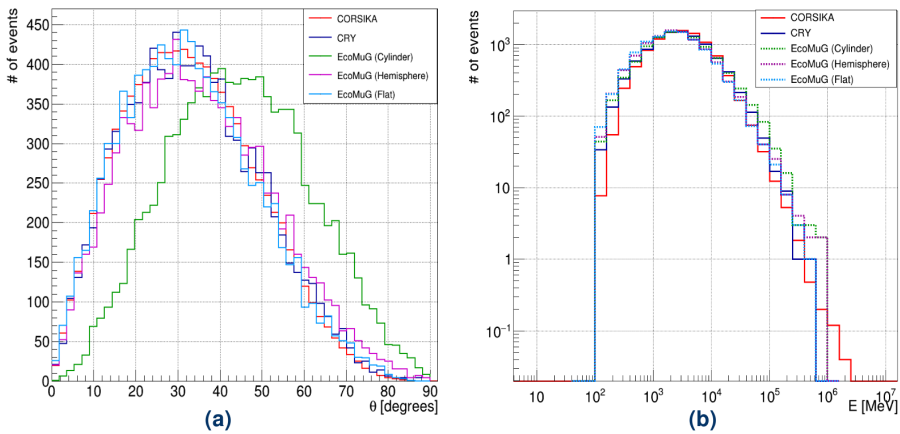
Figure 2.3 shows the distribution of zenith angle θ (a) and kinetic energy E (b) of muons simulated using CRY, CORSIKA (with the DPMJET [95] and GHEISHA [96] hadronic interaction models used respectively for high and low energy collisions in the atmosphere [97]) and the three EcoMug modes (as shown in the Figure 2.2). It can seen that the three generators yield consistent distributions for E; in θ all generators are consistent when used with a flat generation surface, while the cylindrical configuration of EcoMug shows a substantial angular bias. Intuitively, this is explained by recalling that $\theta \sim 0°$ (very vertical muons) can never happen in this configuration as it lacks the top of the cylinder.

An important practical consideration is the speed of execution, for which there are huge differences: we estimated that to generate 10^5 muons on a standard CPU, EcoMug employs O(sec) (depending on the mode: flat is faster, hemisphere is slower, as thoroughly studied in Ref. [86]), CRY O(min), while CORSIKA takes O(hours).

Table 2.1 compares the relative merits of the three generators examined, from the point of view of what is important for a muon radiography experiment. Both CRY and EcoMug can easily be interfaced to GEANT4 [98], meaning that by compiling the appropriate libraries it is possible to run muon generation and detector response simulation in the same job. Running GEANT4 on CORSIKA events requires, instead, to save the generator output in HepMC
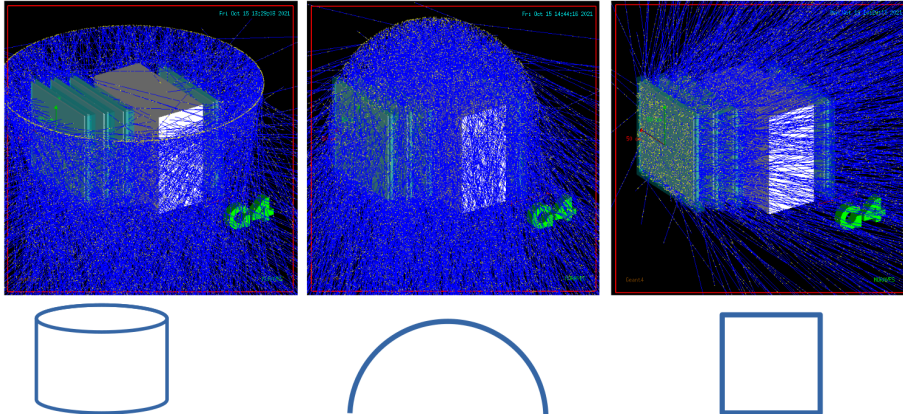
Figure 2.2. ▏ The three EcoMug modes: cylindrical (left), hemispheric (center) and flat (right) generation surfaces, here shown interfaced to the GEANT4 model of the MURAVES hodoscope described in section 3.2.

Figure 2.3. ▏ Distributions of zenith angle θ (a) and kinetic energy E (b) generated using CRY, CORSIKA and three EcoMug modes (corresponding to flat, cylindrical and hemispherical generation planes).

format [99], which complicates the storage logistics. Additional considerations, although less crucial, include the ability to simulate non-muon backgrounds from cosmic showers (e.g., electrons, positrons, hadrons) and multiple muons from the same shower (hence detected simultaneously in the same hodoscope, leading to rejection by the current tracking algorithm). Both features are naturally included in CORSIKA, as it develops the full showers. CRY contains parametrizations of all particles including backgrounds, based on MCNPX [91] and can handle multiple particles per event. The latest version of EcoMug has

been updated to accommodate multiple muons and background particles in its simulations[(★)].

Generator	CORSIKA	CRY	EcoMug
Speed (10^5 muons)	O(hours)	O(min)	O(sec)
Modeling	Ab initio, several models available	Immutable, derived from MC [91]	User-defined, default from [93]
Accuracy	State of the art	Approximate	Approximate
Use with GEANT4	Complex	Easy	Easy
Systematics	Hadronic interaction models	Time dependence (solar cycle)	Alternative parameterizations

Table 2.1. ❙ Qualitative comparison of the features of CORSIKA [85], CRY [84] and EcoMug [86] that are of particular interest for muon radiography.

2.2. Passage of muons through the object of interest

In this section, we will delve into the subsequent phase of the muography simulation process: the simulation of muon traversal through the specific volume of interest. Our exploration will focus on utilizing advanced tools such as PUMAS [100, 101] and the MUSIC code [102], these tools have been meticulously designed to optimize computational efficiency, especially when imaging large targets like volcano. In the case of conventional objects like small statues, our choice for simulating muon interactions will remain GEANT4 [98], the primary Monte Carlo method.

2.2.1. GEANT4

The GEANT4 [98] Monte Carlo framework, built on C++, stands at the forefront of simulating particle passage through various objects and materials. Utilizing the Monte Carlo method and built on a robust object-oriented framework, GEANT4 allows researchers to model complex detector geometries and precisely track particle trajectories, including muon, as they traverse different materials. Its advanced algorithms account for multiple scattering, energy loss, and a myriad of interactions, enabling accurate simulations of muon behavior within the target objects. GEANT4's flexibility enables researchers to adjust

---

[(★)] We were the first to implement and test a technical solution for simulating various types of particles, following private communication with the authors.

simulation parameters, making it adaptable to different experimental setups and diverse materials. This versatility, coupled with its ability to handle intricate particle interactions, positions GEANT4 as a powerful tool for studying muon interactions in detail, crucial for muography applications as well as various other scientific investigations.

However, it's important to note that GEANT4, while powerful, does not simulate all interactions comprehensively. For instance, in specific cases like the simulation of avalanche processes in Resistive Plate Chamber (RPC) detectors, GEANT4 might have limitations. To address this, a linkage with Garfield++ [103], a specialized simulation tool, becomes necessary. Further details regarding such specific interactions and their comprehensive simulation will be discussed in the dedicated section about Garfield++.

2.2.2. PUMAS

The PUMAS library [100, 101], developed in standard C, stands out as a sophisticated transport engine designed to accurately model the trajectories of muon and tau leptons as they traverse diverse materials. One of its notable attributes lies in its flexibility, offering configurable simulation levels tailored to specific needs. Ranging from a swift deterministic Continuous Slowing Down Approximation (CSDA) mode —where the energy loss rate along the track is assumed equal to the total stopping power, ignoring energy loss fluctuations— for rapid assessments to a comprehensive Monte Carlo simulation for detailed analyses (Straggled or Mixed transport mode), PUMAS adapts to the complexity of the study at hand.

A distinctive feature enhancing its utility is its reversibility; it can seamlessly operate in both forward and backward modes, a quality particularly valuable for nuanced muography applications. Beyond its versatility, PUMAS is engineered for efficiency, ensuring expedited computations without compromising accuracy. This efficiency becomes especially significant in time-sensitive scenarios, enabling researchers to conduct thorough simulations within reasonable timeframes. In the realm of muography, where precision and computational speed are paramount, the PUMAS library emerges as a reliable choice, providing researchers with a robust tool to explore the intricate behavior of muons and tau leptons within diverse materials.

2.2.3. MUSIC code

The MUon SImulation Code (MUSIC) [102], established in FORTRAN in 1997, stands as a pivotal tool in the realm of muon simulations, aptly capturing the intricate interactions of muons as they traverse diverse materials. A testament to its reliability, MUSIC has been instrumental in interpreting data from experiments like the Large Volume Detector (LVD) experiment at the Gran

Sasso Laboratory.
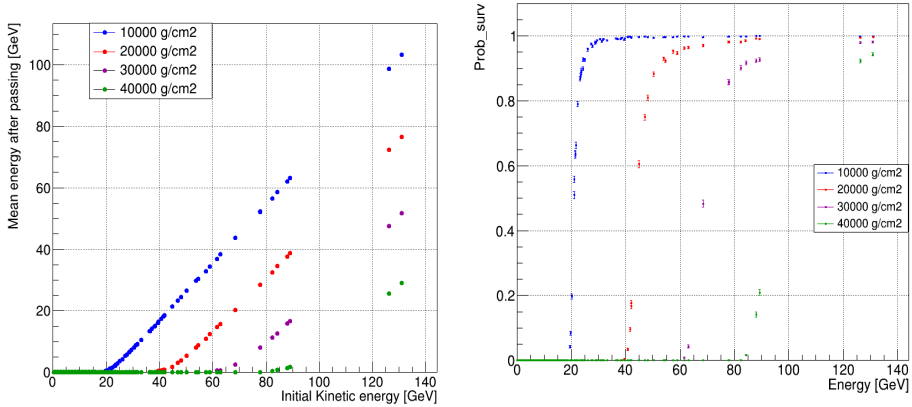
(a) Muon energy after traversing different depths of the rock as function of its energy.

(b) Probability for a muon to survive the passage through various rock depths, as a function of its energy

Figure 2.4. ❙ Study with MUSIC of the muon interaction in different standard rock thickness ($\rho = 2.65 \ g/cm^3$), where CRY was employed as the primary muon generator.

Its capabilities are vast, encompassing the calculation of muon energy losses through processes such as ionization, bremsstrahlung, electron-positron pair production, and muon-nucleus inelastic scattering. MUSIC computational efficiency is enhanced by precomputed and averaged muon interaction cross-sections for specified elements within materials. This strategic approach ensures accuracy while optimizing computational speed, crucial for time-sensitive analyses.

Figure 2.4 presents a study conducted using MUSIC, investigating cosmic muon (generated using CRY) interactions at different depths of standard rock.

2.2.4. Comparison of MC Simulations for Muon-Matter Interactions

In the realm of muon-matter interaction simulations, a comparison among the MUSIC, PUMAS, and GEANT4 Monte Carlo libraries yields valuable insights into their distinct capabilities. PUMAS and GEANT4 emerge as versatile tools, not only offering precise simulations of muon trajectories through various materials but also the ability to incorporate complex geometries, unlike MU-SIC, which lacks inherent geometry modeling capabilities. PUMAS provides different distinctive modes: the Continuously Slowing Down Approximation (CSDA) mode, representing deterministic energy losses, assuming equal stopping power at each point along the track, disregarding any fluctuations in

energy loss. In contrast, the Straggled mode employs a mixed Monte Carlo algorithm accounting for both soft and hard collisions, with straggling in energy loss due to soft electronic collisions.
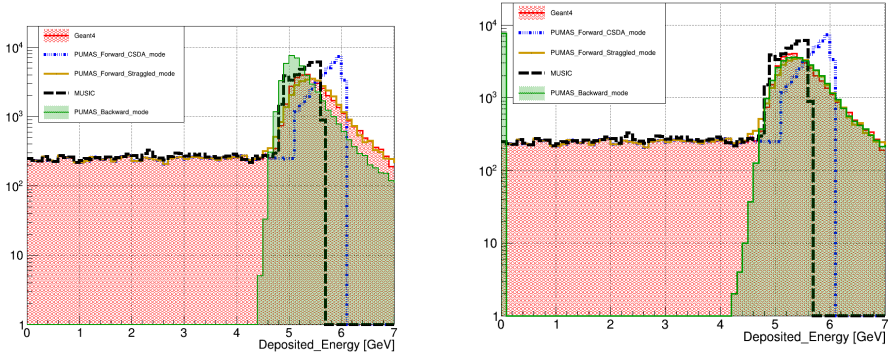

(a) The final energy range of MUSIC output is given to PUMAS backward mode.

(b) The exact final energy distribution of MUSIC output is given to PUMAS backward mode.

Figure 2.5. ┃ Comparison of energy loss distribution in GEANT4, MUSIC and different modes in PUMAS, with initial energy 0 - 20 GeV muon in a standard 10 m thick rock ($2.65\ g/cm^3$).

A comprehensive investigation of these modes involved simulating muon energy loss in a standard rock with a thickness of 10 m and a density of $2.65 g/cm^3$. Initial muon energies ranging from 0 to 20 GeV were utilized in both PUMAS and MUSIC forward modes, revealing intriguing insights upon comparison. In the forward simulations (Figure 2.5), the energy loss distributions of PUMAS and GEANT4 exhibits remarkable resemblance, particularly evident in the Straggled mode, reflecting a rich energy spectrum. In contrast, the CSDA mode in PUMAS displays a sharp cut after the peak position, aligning more closely with MUSIC, albeit with a notable 400 MeV shift. This deviation prompted further investigations into the CSDA mode's parameters.

During backward Monte Carlo simulations, which run simulations in reverse from the detector back to the sky, modeling muon scattering as they pass through the object of interest is crucial, especially for low-energy muons that undergo multiple scattering near the surface, leading them into the detector's acceptance area at misleading angles. In these simulations, inputting the final energy of muons after they have traversed the object is important. In this mode, PUMAS provides limited information in the lower energy range since it can only capture particles passing through the rock.
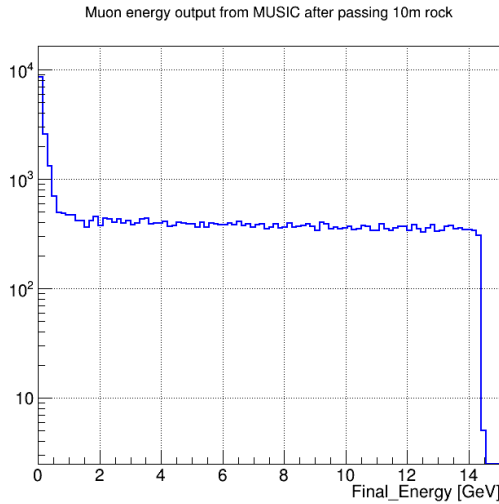
Figure 2.6. | Energy of muons after passing through a 10m rock in MUSIC code.

To comprehend its behavior, a comparative analysis was conducted, considering two scenarios: one utilizing the exact energy distribution obtained from MUSIC (Figure 2.6), represented in Figure 2.5b, and the other where we provided PUMAS with the minimum (0 GeV) and maximum (14.462 GeV) values extracted from this distribution, aiming to explore its behavior in this energy range (Figure 2.5a). This comparison revealed intriguing nuances. Although discrepancies persisted in the lower energy spectrum, significantly better agreement was observed when utilizing the exact energy distribution. Notably, Figure 2.5b revealed a peak at 0 GeV, reflecting PUMAS's anticipation of very low initial energies for stopping particles.

Furthermore, integrating MUSIC into the workflow involved using the HepMC [99] format to link it with GEANT4, a step essential for ensuring a seamless exchange of data between the two platforms. In the case of PUMAS, the challenge arises when working in the backward mode, as its linkage with GEANT4 (which can only operate in forward mode) is not straightforward. This intricacy highlights the need for advanced strategies and meticulous considerations when aiming to integrate these simulation tools effectively.

Additionally, it is essential to emphasize the computational efficiency of these simulations. GEANT4 simulations for 50,000 events require several hours, whereas both MUSIC and PUMAS complete the same task within minutes. This significant difference in simulation time underscores the advantage of using MUSIC and PUMAS for timely analyses in muography applications. However, it is important to note that for MUSIC, additional simulation time is needed to calculate the transportation distance in the external code-simulated

Aspects	MUSIC	PUMAS	GEANT4
Speed (50000 muons)	O(min) + time for code-simulated geometry	O(min)	O(hours)
Simulation Directions	Forward	Forward and Backward	Forward
Modeling	Parametric simulation	Diverse modes: CSDA, Straggled and Mixed	State of the arts
Geometry Modeling	Not designed for geometry implementation	Capable of implementing geometries: using TURTLE [104]	State of the arts
Use with GEANT4	Using HepMC format	complex	/

Table 2.2. ❘ Qualitative comparison of muon transport monte carlo tools.

geometry, a factor that should be considered for a comprehensive evaluation of computational efficiency and overall workflow optimization. This comparison offers valuable insights into the strategic integration of these Monte Carlo tools, guiding their synergistic utilization in complex research scenarios, considering both accuracy and computational efficiency.

2.3. Detector simulation

In this step, we utilize GEANT4 [98], the widely adopted Monte Carlo particle transport simulation and detector geometry tool extensively employed in particle and nuclear physics, as previously detailed. In the following, the intricate detector geometries for the three detectors —MURAVES, Muoscope and Cosmic bench—will be meticulously presented, offering a detailed insight into the simulation setup.

2.3.1. MURAVES detector

For the MURAVES simulation studies, we built a detailed model of a hodoscope in Geant4. It comprises four tracking stations, with a thick lead wall of thickness 60 cm positioned between the 3rd and the 4th stations that acts as 'minimum muon energy' selector with a turn-on point of 0.9 GeV (see section 3.5.3). All the detector parameters detailed in section 3.2 were accurately incorporated into the simulation setup. Figure 2.7 illustrates the interaction of a 1 GeV muon with a MURAVES hodoscope.

An additional software, PHITS [105] (integrated with PARMA/EXPACS [106] for muon generation), was explored as a potential alternative to GEANT4. We managed to create a rough approximation of the MURAVES configuration within this framework. However, due to challenges in replicating all geometric
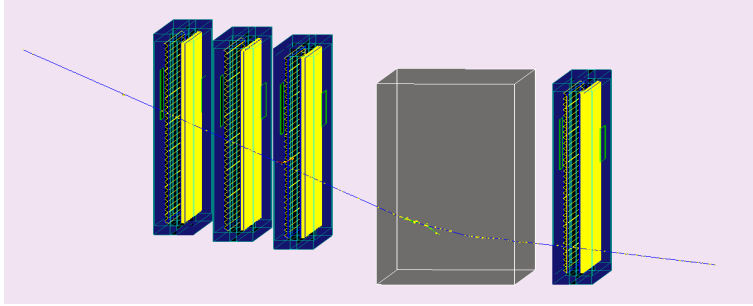
Figure 2.7. ❘ Interaction of a 1 GeV muon with one of the MURAVES hodoscopes in GEANT4.

intricacies accurately, we opted to concentrate on GEANT4 for the detector response simulation.

2.3.2. Portable Muoscope

The active detection component of an RPC comprises a gas layer enclosed between two parallel plates of high resistivity. The setup includes four identical RPC layers, each housed within a aluminum box. Moreover, the muoscope is equipped with an external trigger system matching the active area of our RPCs positioned above and below our telescope. All specifications of the detectors outlined in section 4.2 are integrated into the simulation setup. Figure 2.8 illustrates the interaction of three particles with our simulated portable Muoscope : a μ of 48 MeV (i.e. at the limit of detectability, anything lower than this energy would be fully absorbed, see section 5.1.3) and a μ and an $e-$ of 1 GeV.
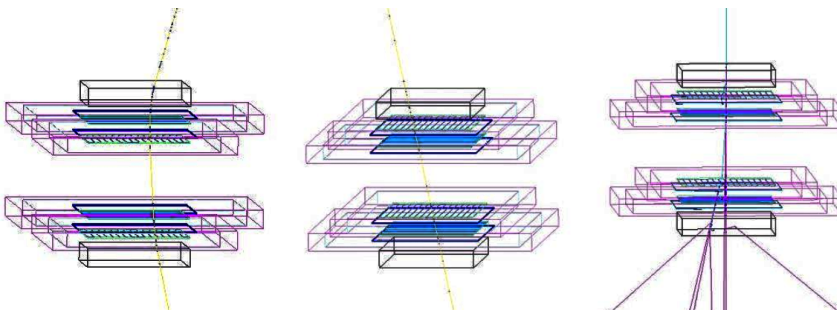
Figure 2.8. ❘ Simulation with GEANT4 of the passage of a 48 MeV muon (left), a 1 GeV muon (centre) and a 1 GeV electron (right) with the addition of two plastic scintillator slabs indicated as white boxes. Muons are in yellow, electrons in blue and photons (from bremsstrahlung) in pink.

2.3.3. Cosmic Bench

One of the detectors in our laboratory is the cosmic bench, originally designed for student projects and calibration of other detectors rather than muography research. This detector consists of two tracking stations positioned 130 cm apart. Each station comprises X and Y planes, each equipped with 16 scintillator bars. These bars are coupled with a light guide to a Photomultiplier Tube (PMT) and enclosed within aluminum boxes. The active area of each station is 160×160 cm^2, and the planes are oriented orthogonally to provide two-dimensional information about cosmic particle hits. The scintillator bars have a rectangular cross-section, measuring 10 cm in width and 1 cm in thickness. All these specifications have been incorporated into a comprehensive simulation setup.

Figure 2.9 displays the GEANT4 simulation configuration of the detector, while Figure 2.10 illustrates the actual setup of the detector in our lab. It's important to note that this entire simulation project, starting from cosmic particle generation to their interaction with the scintillator bars, has been meticulously executed. Additionally, efforts were made to find the optimal working high voltage, scan parameters and data analysis. However, due to the detector discontinuity concerning my thesis work, my discussion will be limited up to this point.
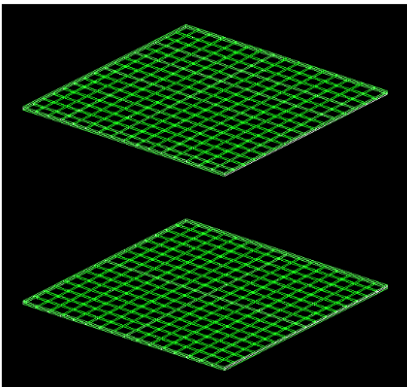
Figure 2.9. ❘ Configuration of the cosmic bench in Geant4.

Figure 2.10. ❘ The actual setup of the cosmic bench in our laboratory, including the frame of reference.

3. Chapter

MURAVES: MUon RAdiography of Mt. VESuvius

3.1. Purpose and motivation : Mount Vesuvius

Italy stands at the crossroads of the Eurasian Plate and the African Plate, making it highly susceptible to seismic and volcanic activities. In this dynamic landscape, Mount Vesuvius, in the southern region near Naples, emerges as one of Europe's most active and perilous volcanoes. Despite its threat, the surrounding area is densely populated, amplifying the risks associated with potential eruptions. Continuous monitoring of this volcano is therefore essential to avert potential disasters.

Throughout history, Vesuvius has experienced several explosive eruptions, with the most infamous one occurring in 79 AD, known as the Plinian eruption, which obliterated Pompeii, Herculaneum and other nearby settlements. This catastrophic event led to the collapse of a significant portion of the volcano's structure, forming the Mt. Somma caldera, from which the current Vesuvius cone emerged.

Over the years, Vesuvius's eruptive activities have altered its physical features, including significant changes in its crater, as depicted in Figure 3.1. The most recent eruption occurred in 1944, reshaping the crater dramatically, as shown in Figure 3.2. This event left high-density lava deposits on the northeast side and scattered low-density deposits on the volcano's summit.

Understanding Vesuvius's internal density distribution is crucial for deciphering past explosive events and predicting future volcanic activity. Muon radiography, a technique used to reveal density variations within the volcano, plays a pivotal role in this endeavor. When combined with conventional gravimetric measurements, muographic data enhance the accuracy of the information obtained from each method, providing comprehensive insights into the volcano's behavior.

In pursuit of this knowledge, the MURAVES (MUon RAdiography of Mt. VESuvius) project has been initiated. This collaborative effort involves the Istituto Nazionale di Geofisica e Vulcanologia (INGV), the Istituto Nazionale di Fisica Nucleare (INFN), and the Universities of Naples "Federico II" and Florence. Furthermore, since 2019, also UCLouvain and University of Gent
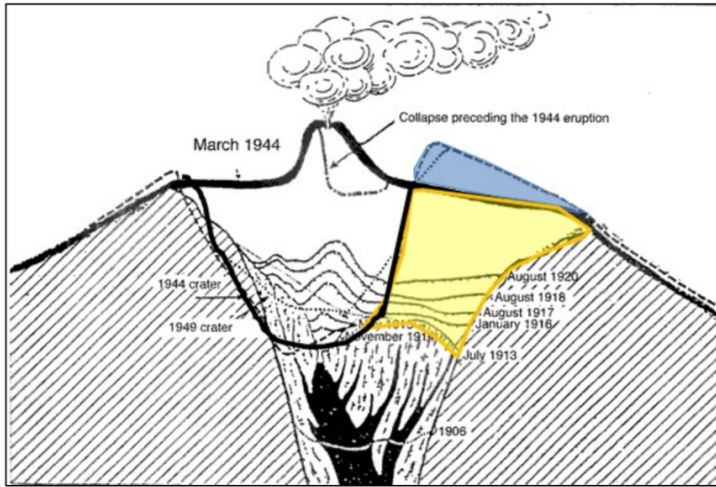
Figure 3.1. ❘ The changes in Vesuvius crater from 1906 to 1944 were documented through observations made by Malladra and other researchers affiliated with the Osservatorio Vesuviano [107].
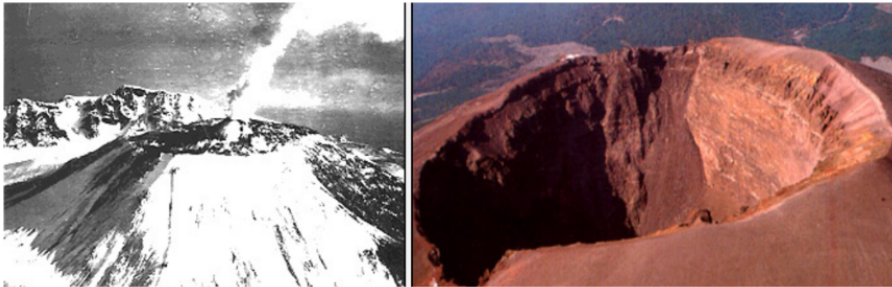
Figure 3.2. ❘ The crater of Vesuvius before the 1944 eruption (on the left) and its current appearance (on the right).

joined this collaboration.

In the following sections, we will offer an in-depth overview of the MU-RAVES project, delving into its methodologies and discussing the anticipated contributions. This includes insights into Vesuvius's crater density and the comprehensive simulation work undertaken to establish the complete simulation chain for this project.

3.2. The MURAVES detector

MURAVES has been developed based on the prior expertise gained from the MU-RAY prototype. The project comprises three muon hodoscopes, named ROSSO, NERO, and BLU, each with a cross section area of 1 m^2, resulting in

a total sensitive area of 3 m^2, where two of them are positioned in "forward-looking mode" to take Mt. Vesuvius data, while one is installed in reverse orientation, to acquire a free-sky control sample. Each hodoscope consists of four pairs of tracking planes that measure XY coordinates. The fundamental unit of the hodoscope is a set of 32 plastic scintillator bars, referred to as a module, as illustrated in the Figure 3.4 (b). These modules are assembled in pairs to create a single-view plane, and two such planes are interconnected orthogonally to form a tracking station. To minimize background contamination, especially from low-energy cosmic rays, a lead block is placed between the last two stations. The setup and reference frame of one hodoscope are illustrated in the accompanying Figure 3.3.

(a)

(b)
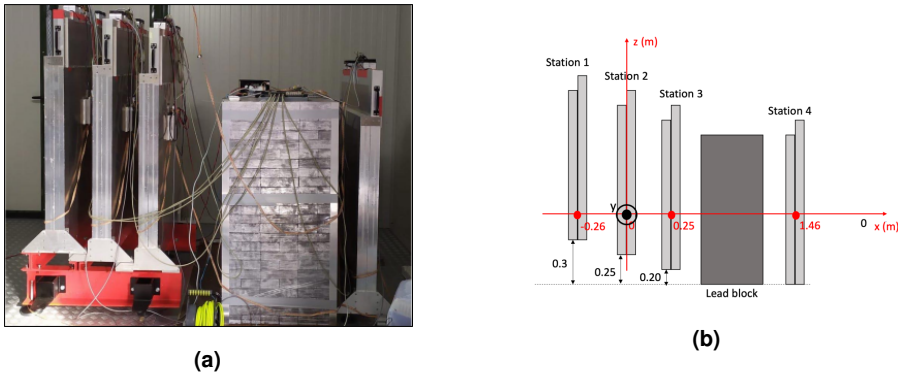
Figure 3.3. (a) One of the MURAVES hodoscopes. (b) A schematic view of the reference frame of the MURAVES hodoscopes.

The scintillator bars, supplied by FERMILAB-NICADD, are extruded with a central hole $\sim 1.5 \pm 0.1 mm$ in diameter to accommodate a wavelength shifting fiber (WLS). They are coated with a TiO_2 layer to enhance internal reflectivity and shield them from environmental light. The scintillator plastic consists of polystyrene bulk infused with PPO and POPOP scintillation dopants emitting blue light at around 420 nm, with an emission time of approximately 3 ns.

The employed fibers are multiclad Kuraray Y11 S-35 type, with a diameter of 1.2 mm. They exhibit an absorption spectrum ranging from 400-470 nm and an emission spectrum falling between 470-550 nm, peaking in the green region. The scintillator bars have an isosceles triangular section with a base of 3.3 cm and a height of 1.7 cm (as depicted in the Figure 3.4 (a)). This triangular shape enhances spatial resolution by utilizing a weighted average method to calculate the muon position, with the charges collected by adjacent bars serving as weights (Figure 3.4 (c)).

The light traveling through the WLS fibers is detected by Silicon Photomultipliers (SiPMs), with each fiber coupled to one SiPM. These photosensors are

Figure 3.4. ⎮ (a) The scintillator bars possess a triangular form and are coated with a white oxide layer. Each scintillator houses a wavelength-shifting (WLS) fiber running through its center. (b) These 32 bars are bonded together in a half-plane section approximately 50 cm wide. (c) A center-of-mass algorithm is employed to reconstruct the muon coordinate based on the light collected by two adjacent scintillators.

organized into arrays of 32 elements and are situated on a hybrid printed circuit, with one circuit assigned to each detector module, as shown in the Figure 3.5.
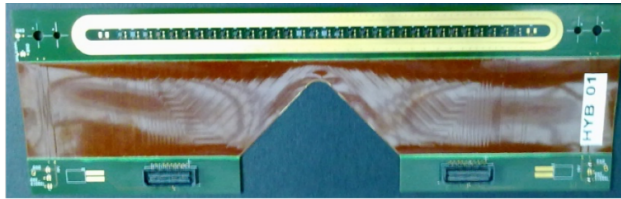
Figure 3.5. ⎮ Hybrid board with 32 SiPMs housed.

The installation in remote locations such as the side of a volcano often lacks access to a standard electricity supply. Consequently, a low-power Front-End Electronics (FEE) and Data Acquisition (DAQ) system were developed to address this challenge. The Front-end electronics comprise identical SLAVE boards, one for each module, each containing 32 SiPM channels. Each board is equipped with an EASIROC ASIC [108] that allows for SiPM gain adjustment, tunable preamplification gain, signal shaping, charge measurement, and high and low gain multiplexed outputs. Additionally, each SLAVE board incorporates a Time-to-Digital Converter (TDC) for measuring time-of-flight (ToF) with a resolution of 0.1 ns. Remarkably, each board consumes less than 2.5 W of power. This feature holds significant importance, given the absence of a power source in the remote area where MURAVES is deployed; all power supply is derived from solar panels.

The SiPM signals are amplified and converted into Analog-to-Digital Converter (ADC) counts, quantifying the charge deposited in the SiPM. Each channel generates a fast logical signal based on a tunable threshold level. The logical OR of these 32 fast signals provides the local trigger (OR32), which is then transmitted to the MASTER board to create the global trigger.

The MASTER board, equipped with a Field-Programmable Gate Array (FPGA) and a Raspberry Pi computer, manages the global trigger and the DAQ system.
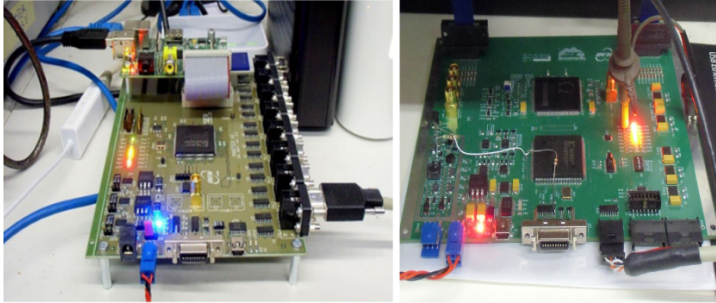
Figure 3.6. | Left: the MASTER board. Right: a SLAVE board.

It collects all SLAVE outputs, verifies if the trigger requirements set by the FPGA are met, and if affirmative, acquires and stores data in a storage unit. Figure 3.6 illustrates both a SLAVE and a MASTER board.

For each MURAVES hodoscope, the front-end electronics consist of 16 SLAVE boards and 1 MASTER board, totaling 51 electronic boards. In this setup, ASD-RGB1C-P Silicon Photomultipliers (SiPM) [109] from Advansid are employed as photosensors. SiPMs are sensitive to temperature changes; therefore, a Slow Control Unit is employed for temperature and humidity monitoring. This unit also operates an efficient Peltier cooling system, allowing the hodoscopes to function even on the hottest days by maintaining manageable SiPM temperatures. Refer to Figure 3.7 for a visual representation of this temperature control system.

Figure 3.7. | The temperaure control system. Left: the elements before installing on the detector. Right: the system installed on the detector.

3.3. MURAVES @ Mt.Vesuvius

The MURAVES telescopes are housed inside a container (see Figure 3.8) located at 1500m away from the crater summit. The container is situated on the flank of Mt. Vesuvius at an elevation of approximately 600m a.s.l. The site was

selected for its easy accessibility and optimal signal-to-noise ratio, which was assessed through Monte Carlo simulations. The placement and orientation of the container were designed to maximize the acceptance of the hodoscopes towards the volcano's crater. As depicted in Figure 3.9, the laboratory is positioned with a central line of sight rotated ~ 45 degrees with respect to the North. Inside the container, four designated spots were arranged to accommodate the muon hodoscopes.


Figure 3.8. ⏐ The container positioned atop the volcano at an elevation of 600 meters above sea level.

Figure 3.9. ⏐ Left: The MURAVES laboratory location, showing the central line of sight of the telescope with respect to the North direction. Right: The view of Mt. Vesuvius as observed by the MURAVES telescope.

The interior layout of the container, includes the arrangement of detectors and lead walls. Three of the four designated spots are oriented towards the volcano, while the fourth spot is dedicated to calibration data acquisition, as illustrated in Figure 3.10. Calibration involves estimating the incoming muon flux from the open sky, assuming an absence of the volcano's influence. To achieve this, the detector orientation was reversed, pointing in the opposite direction where
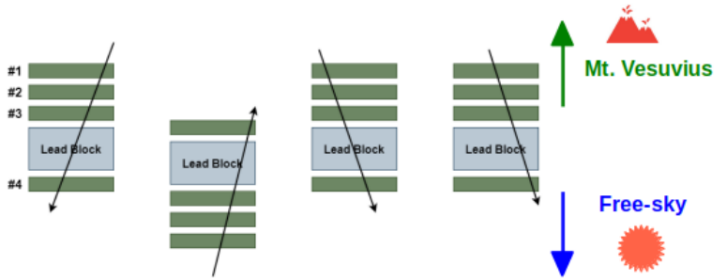
Figure 3.10. ❙ Schematic illustrating the container layout.

Figure 3.11. ❙ Battery system installed inside the container (left) and solar panels mounted on the roof (right).
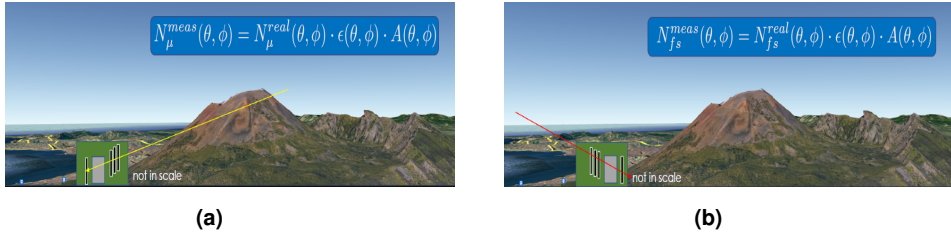
only the sky is encountered by muons before reaching the telescope, under the assumption of flux isotropy. Notably, the telescope operates on low power, with each hodoscope requiring approximately 30 W for full functionality. This power is supplied by a solar panel system installed on the container's roof, connected to an array of batteries (Figure 3.11), ensuring the continuous operation of the apparatus, even during nighttime hours.

3.4. Preliminary results

The ultimate goal of the MURAVES experiment is to achieve a density distribution measurement of Vesuvius' Great Cone. Currently, data analysis results are categorized based on the muon tracker and the specific working point. Significant statistical data are available from the ROSSO and NERO detectors, while calibration data from the BLU detector remains pending.

The available datasets are segregated into four distinct groups: two from ROSSO and two from NERO, obtained at the working points of 15°C and 20°C. As outlined in section 1.4.1, density is assessed through muon transmission, calculated by dividing the muon flux measured from Vesuvius by the flux measured from the open sky. These fluxes are determined through separate

data acquisitions, with the detector oriented inversely.

$$N_\mu^{meas}(\theta,\phi) = N_\mu^{real}(\theta,\phi) \cdot \epsilon(\theta,\phi) \cdot A(\theta,\phi)$$

$$N_{fs}^{meas}(\theta,\phi) = N_{fs}^{real}(\theta,\phi) \cdot \epsilon(\theta,\phi) \cdot A(\theta,\phi)$$

(a)   **(b)**

Figure 3.12. ▏ Visual representation of the detector orientation during data collection on Vesuvius (a) and in open-sky measurements (b).

Figure 3.12 provides a visual representation of the difference between data collection from Vesuvius and open-sky measurements.

3.4.1. Data sets

The deployment of the three telescopes (NERO, ROSSO, and BLU) spanned from Fall 2019 to Summer 2020, and data collection has been nearly continuous since. Each telescope's datasets are categorized based on their orientations (Vesuvius runs and free-sky runs) and the specific operating working points of their Silicon Photomultipliers (SiPMs).

A working point is defined by a designated target temperature, which the temperature control system maintains for the SiPM, along with an optimized bias voltage corresponding to that temperature. Ideally, the target temperature should be within 5-7 degrees of the environmental temperature inside the container. This proximity prevents excessive power consumption and ensures a safe distance from the dew point, thus preventing condensation damage. Several working points have been defined, automatically adjusting if significant external temperature changes occur. Certain performance variations have been observed based on the working point, impacting trigger rates. Consequently, all results are extracted separately for different working points and combined only when statistically consistent.

The primary working points, where the majority of data were collected, feature target temperatures of 15 and 20 degrees Celsius, denoted as WP15 and WP20, respectively. Track quality is assessed by the alignment degree of the reconstructed hits, measured using the normalized χ^2 of the linear fit divided by the degrees of freedom. An upper cutoff is applied to the normalized χ^2, but due to potential variations in performance across different telescopes and working points, the same χ^2 cutoff can yield different track rates in various datasets. To address this, a data-driven approach has been developed [110], relying on the observed χ^2 distributions in control regions $(\Delta\alpha, \Delta\phi)$ during

both Vesuvius and free-sky runs, where α is the elevation angle (related to the zenith angle θ by $\alpha = (\pi/2) - \theta$) and ϕ the horizontal angle of arrival of the muon.

Dataset	Vesuvius runs	Free-sky runs	χ^2 cut
ROSSO, WP15	51 days	9.5 days	5.0
ROSSO, WP20	40 days	14.3 days	4.4
NERO, WP15	43 days	10 days	5.1
NERO, WP20	26 days	17 days	5.1

Table 3.1. ▏ Cumulative duration of the Vesuvius and free-sky runs analysed for the first preliminary results, and upper cut on the normalised χ^2 applied to the tracks in each dataset selection [110].
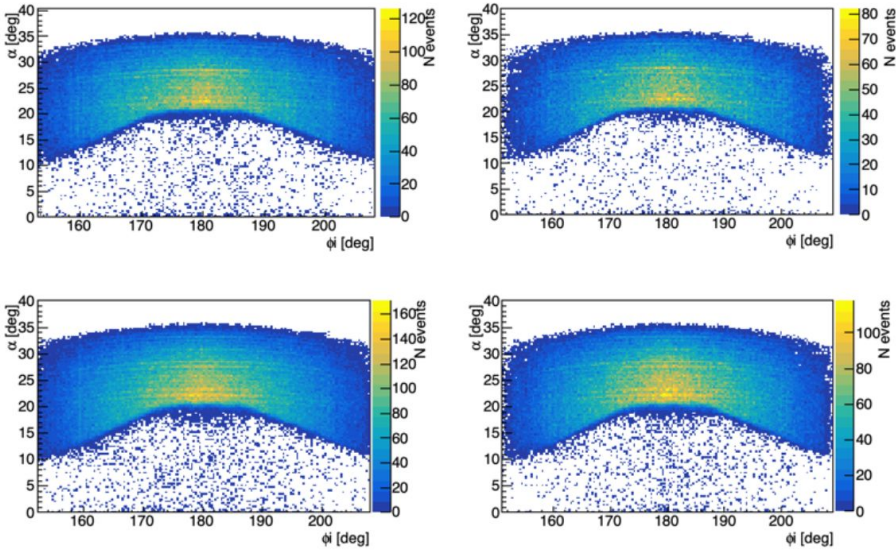
Figure 3.13. ▏ Muon counts as a function of α and ϕ for the Vesuvius datasets for NERO (top row) and ROSSO (bottom row) in WP15 (left column) and WP20 (right column) [110].

Table 3.1 provides details on the utilized datasets, their durations, and the normalized χ^2 cutoffs. While free-sky runs are shorter than Vesuvius runs, they contribute significantly to the overall statistics, as evident from the muon counts in Figs. 3.13 and 3.14. Generally, these runs do not substantially impact the statistical uncertainty in $T(\alpha, \phi)$ (eq. 1.17) for the bins corresponding to the Great Cone.
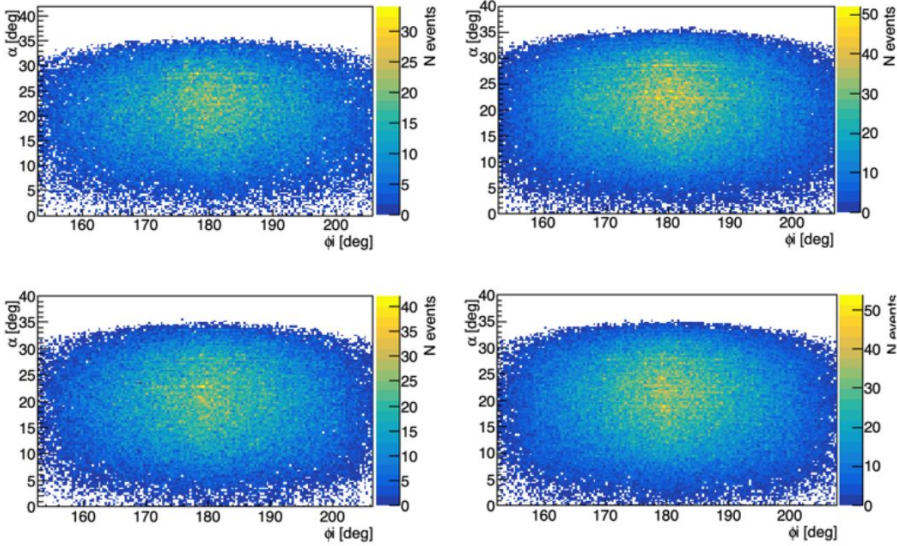
Figure 3.14. | Same as Figure 3.13 for the free-sky datasets [110].
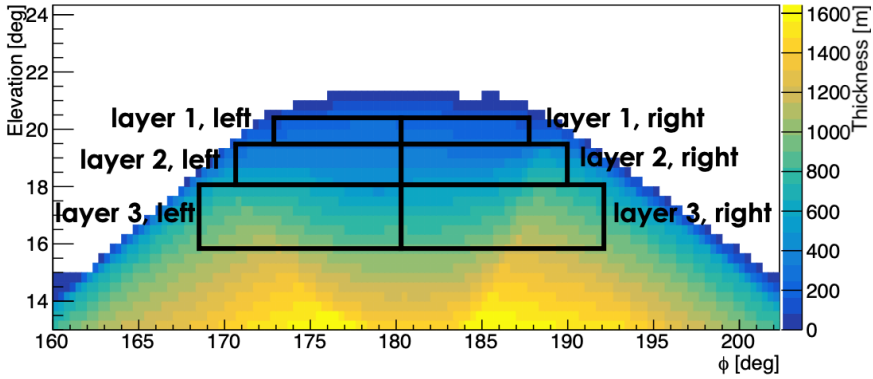
3.4.2. Density projection asymmetries

Due to the limited number of muon events surviving the passage through Mt. Vesuvius, generating a highly detailed $T(\alpha,\phi)$ map is still unfeasible. However, we can conduct an initial measurement relevant to volcanology by comparing muon flux through broad angular bins at varying altitudes.

The focus lies on the summit, specifically the elevation range $\alpha \geq 16°$, corresponding to a rock thickness of < 1 km, as depicted in Figure 3.15. The figure also outlines the definition of the (α,ϕ) regions for comparison. To minimize the impact of model assumptions, our approach emphasizes measuring ratios rather than absolute values. The muon counts within each region $^{(\star)}$ are normalized by the thickness of the traversed rock, utilizing the Digital Terrain Model (DTM) provided by INGV [112], which boasts O(m) resolution, ensuring precision at this level.

Crucially, this measurement does not employ free-sky data in the normalization, although these data have played an indirect yet pivotal role in calibrating and validating the detectors.

Table 3.2 displays the density asymmetry right/left sides at three distinct altitudes. Each layer's four independent samples align within one standard deviation (σ). The table's last column presents the layered results, assuming statistical independence. These findings indicate a higher projected density on the right side compared to the left at higher elevations as 1.5σ level , while this

---

$^{(\star)}$ Detailed numerical values can be found in Refs [110,111].

Figure 3.15. ❘ Definition of the angular regions utilized for the first measurement of density projection asymmetries. Reproduced from Ref. [111].

	ROSSO WP15	ROSSO WP20	NERO WP15	NERO WP20	Average
Layer 1	$1.08^{+0.11}_{-0.09}$	$1.16^{+0.12}_{-0.10}$	$1.07^{+0.14}_{-0.11}$	$1.02^{+0.17}_{-0.13}$	$1.09^{+0.06}_{-0.05}$
Layer 2	$0.99^{+0.09}_{-0.08}$	$0.92^{+0.11}_{-0.09}$	$0.96^{+0.13}_{-0.10}$	$0.93^{+0.14}_{-0.11}$	$0.96^{+0.06}_{-0.05}$
Layer 3	$0.87^{+0.09}_{-0.08}$	$0.92^{+0.09}_{-0.08}$	$0.94^{+0.11}_{-0.09}$	$0.91^{+0.14}_{-0.11}$	$0.90^{+0.05}_{-0.04}$

Table 3.2. ❘ Preliminary measurements of the right/left opacity asymmetry at three different altitudes, and corresponding statistical uncertainties [110].

pattern reverses at lower altitudes.

However, it is important to note that further analysis, including data from the third MURAVES telescope, is necessary to either confirm or refute these preliminary indications.

3.5. Simulation Chain of the MURAVES experiment

Comparing data with Monte Carlo (MC) simulations is very important for the imaging of a target. A popular approach in muography is to compare various density hypotheses in MC with the observed transmission map, seeking the simulated hypothesis that provides the best fit to real data. In other types of studies, one is interested in anomalies with respect to the expected map from MC. In all those cases, various effects can bias the expectations, thus it is important to quantify their impact by testing various modeling assumptions in MC, in order to do that a full simulation chain should be developed as illustrated in Figure 3.16.
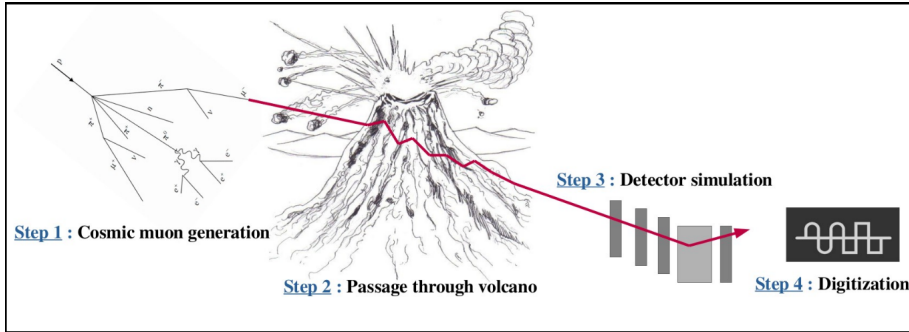
Figure 3.16. | A schematic representation of the MURAVES simulation chain.

3.5.1. Cosmic muon generation

As outlined in section 2.1.4, a comparative study involving three distinct particle generators (CRY, CORSIKA, and EcoMug) was undertaken. The decision was made to utilize CRY as the primary generator for our analysis, while keeping CORSIKA and EcoMug as alternative options for the purpose of systematics estimation.

3.5.2. Passage of muons through volcano

The probability of a muon surviving the crossing of a certain amount of rock is approximately determined by the opacity of the latter (defined as the integrated matter density ρ over the path length, i.e. $\omega \equiv \int_{entry}^{exit} \rho(x)dx$) and the initial energy of the muon. It also depends on the chemical composition of the rocks [23], but these effects are expected to be small, in the Vesuvius case, with respect to the precision expected to be achievable with MURAVES. The measurement of the transmitted flux of atmospheric muons through a target in different directions from a given point of view (the position of the muon detector) provides the two-dimensional projective measurement of the target, and the average density ($\overline{\rho}$) of the material of this target can be calculated by knowing the opacity using the equation $\omega = L\overline{\rho}$, where L is the total muon path length within the material. The path lengths corresponding to different zenith and azimuth angles of arrival of the muons, across the Vesuvius crater, are evaluated using a Digital Terrain Model (DTM) with 1 m resolution, derived using the data from [112] shown in Figure 3.17.

The expected muon flux passing through Mt. Vesuvius (Figure 3.18) is calculated using PUMAS. As discussed in section 2.2.2), PUMAS is a muon transport library that utilizes the Backward Monte Carlo (BMC) technique. Through collaboration with the authors of PUMAS and integration with TURTLE [104] for Digital Terrain Model (DTM) navigation, we identified the optimal installation point for the MURAVES detector. This determination was based on
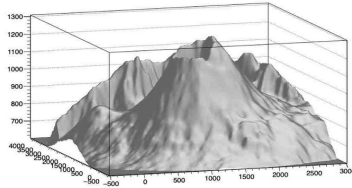
Figure 3.17. | Digital terrain model of Vesuvius crater. Based on data from [112].
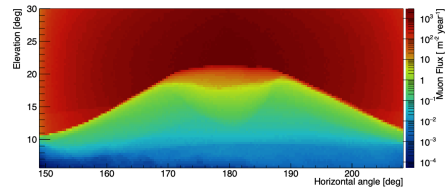
Figure 3.18. | Expected muon flux per year considering the geometrical acceptance of the detector, estimated with PUMAS.

unobstructed views of Mt. Vesuvius and the expected signal purity across most directions. In this context, purity serves as a critical metric, representing the ratio of muon flux without scattering to muon flux with scattering. A lower purity value indicates significant contamination from low-energy muons with diverse entry and exit directions due to multiple scattering. Such contamination can significantly impact the resolution of muography, underscoring the importance of selecting an installation point with high signal purity.

To seamlessly incorporate the step of muon passage through the volcano into the complete workflow, and in line with the study conducted in section 2.2.4, it is necessary to integrate the DTM file into MUSIC using Geant4 or an external geometry macro. Subsequently, the final states of muons generated by CRY, as integrated into MUSIC (refer to section 2.2.3), will be saved into a file. This file will be provided to PUMAS, allowing the output flux from PUMAS to be used in our Geant4 detector for studying its response..

3.5.3. Detector response

For the MURAVES simulation studies, we built a detailed model of a MURAVES hodoscope in GEANT4 as already described in section 2.3.1, interfaced with CRY (section 2.1.2) as source for all signal and background particles. For specific studies, single muons are simulated at specific energies and incident positions using a so called "particle gun", or the General Particle Source class.

One study aimed at determining the probability for a muon to reach the 4th station of the detector after passing through the lead wall was performed using the particle gun. This probability is defined as the ratio of the number of events that reached the 4th station to the number of events which crossed the first 3 stations. The results, as shown in Figure 3.19, revealed a 50% survival probability at 0.9 GeV (dotted red line) and nearly 100% at 1.2 GeV (solid green line). The study of this probability demonstrated that the lead wall acts as a 'minimum muon energy' selector with a turn-on point of ~0.9 GeV.

Additionally, GEANT4 was employed to inform the selection of a potential analysis step based on scattering induced by the lead wall between the 3rd and
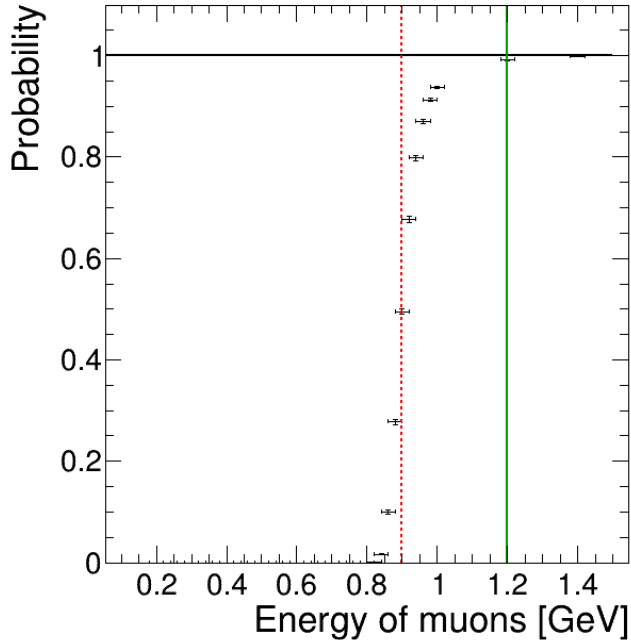
Figure 3.19. | Probability for a muon to survive the passage through the lead wall, as a function of its energy.

4th stations. The objective is to further reduce low-energy muons, post passive filtering provided by absorption in the lead wall, while retaining high-energy muons, crucial for depth information. To conduct this study, 40 million muons were generated with CRY under free-sky conditions, and events with signals in all hodoscope stations were selected. GEANT4 provided scattering points within the lead wall, approximated using angles between vectors connecting station hits as illustrated in Figure 3.21. This approach mimicked practical requirements applicable to real data tracks. The frequency of events surviving an upper cut on this angle was then calculated.

Figure 3.20 illustrates the results for muons of different incoming energy categories. The horizontal axis represents the upper cut on the scattering angle (in steps of 2.5°), while the vertical axis displays the survival frequency of muons passing this cut, among those providing hits in all stations (i.e., not absorbed in the lead wall). The data revealed that even a stringent cut of $\leq 5°$ preserves the vast majority of muons above 2 GeV (better than 90% between 2 and 3 GeV, and almost 100% above 3 GeV). However, this cut removes over 40% of muons between 1 and 2 GeV and about 70% of sub-GeV muons that passed the lead wall, due to their broad angular distribution.
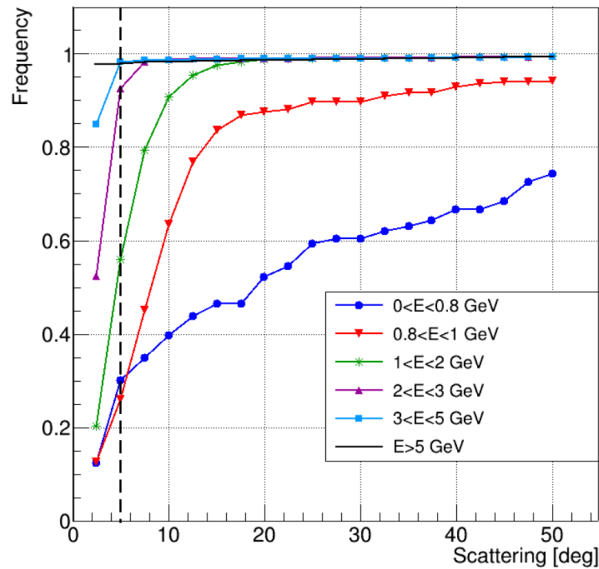
Figure 3.20. | Efficiency of various possible upper cuts on the scattering angle for different ranges of incoming muons energy.

As demonstrated in Figure 3.22, applying this cut in our simulation tracking displayed an elimination of muons traveling in the opposite direction of the detector due to lead scattering. Implementing this new cut in the data could be the next step to enhance muon selections and angular resolution.

3.5.4. Digitization, clustering and tracking

The GEANT4 output comprises "hits", representing each interaction of a particle with the sensitive detector material (scintillator bars) for each simulation step. Hits are characterized by their 3D position, time, energy deposition, and the identity of the involved particle. In the GEANT4 simulation, when a muon traverses a detector plane, it typically generates multiple hits in the scintillator bars, while in reality, only a single signal is obtained per bar. To address this, our subsequent simulation step involves the 'digitization' of these raw GEANT4 hits, which entails quantizing both their positions and energy deposits. Initially, energy deposits are summed per scintillator bar and then converted into the number of photoelectrons (nPE).

In the simulation phase, a pencil beam of 5 GeV from the GEANT4 particle gun is utilized to convert the energy deposited per hit into the energy deposited per scintillator bar for each plane. This conversion is performed by summing the deposited energies for all hits belonging to the same bar. Subsequently, the average deposited energy distributions for each plane are obtained (in MeV).
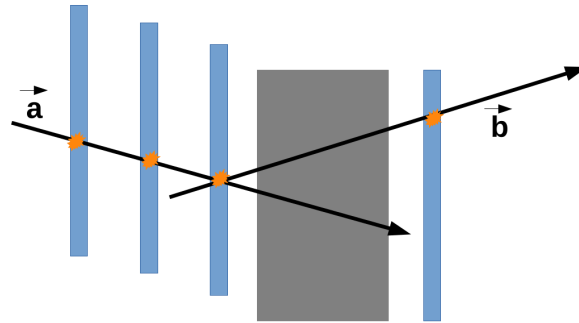
Figure 3.21. ▍ Schema illustrating the scattering within the lead wall, where $\vec{a}$ represents the vector created from hits in the first and third stations, and $\vec{b}$ represents the vector formed from hits in the third and fourth stations.

(a)

(b)
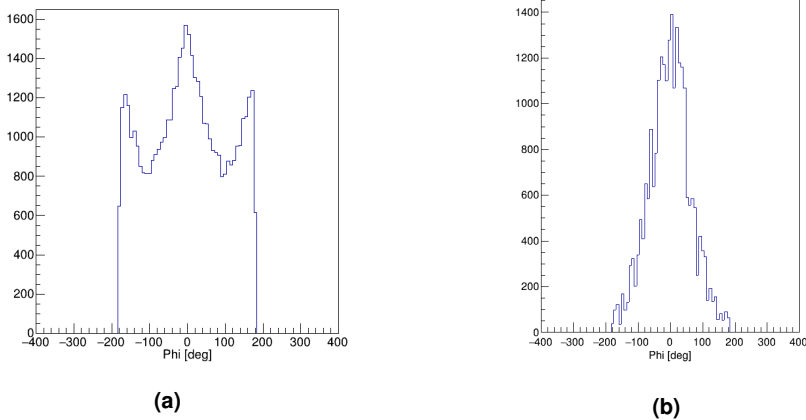
Figure 3.22. ▍ The phi distribution of tracks crossing the entire MURAVES detector before (a) and after (b) applying a scattering cut $\leq 5^{\circ}$.

The mean energy value across all planes remains remarkably stable, around 1.4 MeV, with less than a 3% variation. Figure 3.23 illustrates the simulated energy deposition distribution for one of the detector planes, 1X, as an example.

In the real MURAVES data, energy deposited per scintillator bar (in nPE) for each plane is accessible after processing through the reconstruction software. These distributions are fitted with a simple Landau function, and the most probable value (MPV) from the fit is taken as the average deposited energy for a given plane in the MURAVES data, around 10nPE (Figure 3.24 shows the energy deposition distribution in nPE for ROSSO and NERO detectors in plane 1X).
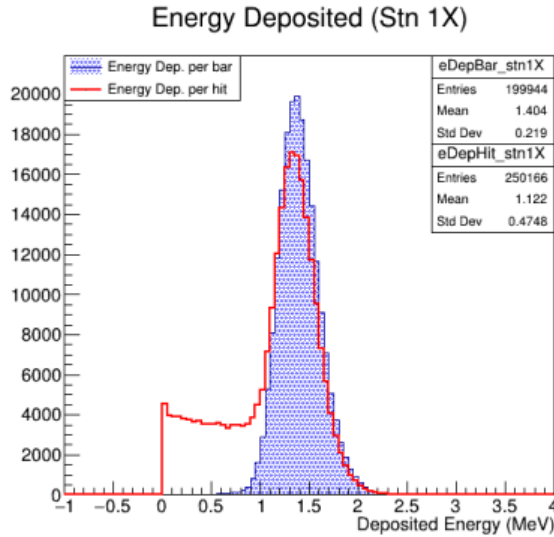
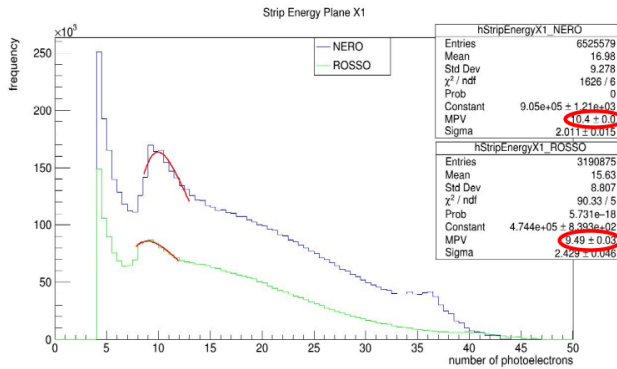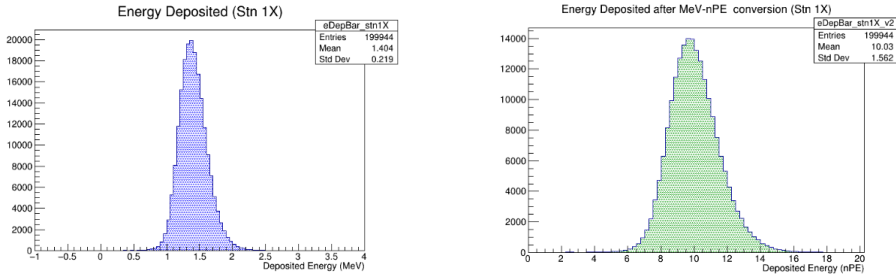**Figure 3.23.** Simulated energy deposition distribution in plane 1X per bar and per hit.

Figure 3.24. Energy deposition distribution per bar in plane 1X based on the data obtained from NERO and ROSSO detectors.

By comparing the peak deposited energies observed in real and simulated data, respectively, we establish a conversion factor of 10 nPE for every 1.4 MeV. At this stage, we obtain a single value for the energy deposited per bar, expressed in appropriate units, as illustrated in Figure 3.25 for plane 1X, allowing us to apply the clustering algorithm. Our clustering algorithm begins with energy clusterization, a method designed to process the deposits on the bars within the detector. This technique combines adjacent bar to create energy clusters, enabling precise determination of muon hit coordinates. To qualify for

Figure 3.25. | Left: Simulated energy deposition (in MeV) before conversion, Right: Simulated energy distribution (in nPE) after conversion.

consideration, each bar deposit must surpass a predefined energy threshold, set at 6 photoelectrons based on the trigger threshold.

In situations where a cluster consists of a single bar, it is accepted only if its energy surpasses 10 photoelectrons. This precautionary measure prevents single bar triggered by dark counts from being included. However, for more precise localization, in instances where there is only a single bar with a signal, the two adjacent bars are included if their signals register higher than 1 photoelectron.

Each resulting cluster is characterized by two key parameters: total energy deposit and position. The total energy deposit represents the sum of the energies of the bars within the cluster. To determine the position of the cluster accurately, a weighted mean of the barycenter positions of the bars is calculated, where the weights are determined by the corresponding signals, measured in number of photoelectrons. It's noteworthy that the same clustering algorithm and thresholds are applied in both real data and Monte Carlo simulations. Simulated clusters are fed into the tracking algorithm, which again is rigorously applied as in real data. The tracking is performed for X planes and Y planes independently. To validate the full simulation chain, the χ^2 values of the simulated tracks are compared with those of the real data from a free-sky calibration run. For this, 10^5 muon events were simulated, all crossing at least the first three planes of the detector, and the full reconstruction chain was applied. The result is shown in Figure 3.26, which also includes an alternative MC dataset where no thresholds are applied in the clustering algorithm. Although the trend is qualitatively similar between data and MC, the latter is significantly too optimistic, i.e. it has a lower tail than real data. This difference is found to be unrelated to the applied cluster thresholds, as demonstrated by the similarity of the MC distributions with and without thresholds.

A possible insight in the source of this discrepancy is offered by Figure 3.27, which shows the comparison of the size of the clusters involved in the tracks
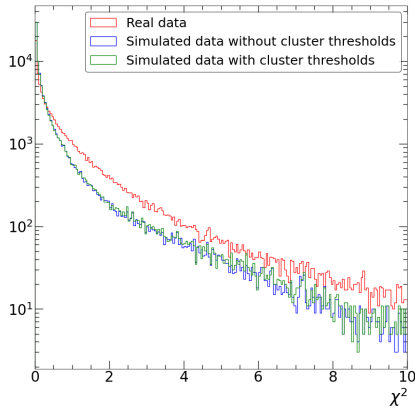
Figure 3.26. ▮ Comparison of the χ^2 of the tracks in real data and simulated data (the latter with and without clustering thresholds).
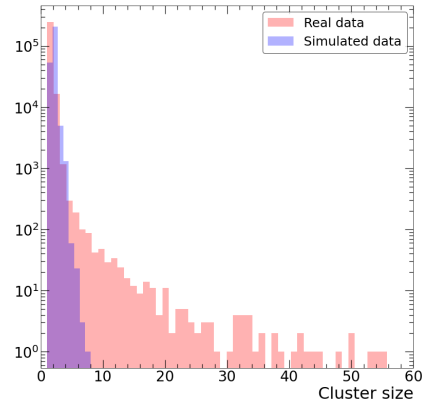
Figure 3.27. ▮ Comparison of the sizes of the clusters involved in the selected tracks ($\chi^2 < 5$) for real and simulated data.

selected with the standard cut $\chi^2 \leq 5$. The results reveal that MC fails to simulate the long tail observed in real data. This discrepancy may be due to unmodeled effects like dark noise and various front-end electronics impacts. Addressing this disparity requires either emulating these effects in simulation or refining real data selection at the cluster level. Further improvement in this area will be the focus of future efforts.

4. Chapter

Portable Muoscope

In our quest to enhance particle detection technology specifically for muography applications, our research journey steered us toward the intricate task of developing a portable Glass Resistive Plate Chamber (gRPC) detector. This chapter provides a comprehensive exploration of the extensive efforts undertaken in our laboratory, where we navigated through multifaceted challenges to develop an efficient and portable and gas tight gRPC system. Before delving into the nuanced details of our experimental methodology and discussing some simulation studies, it is essential to grasp the fundamental principles underpinning RPCs.

4.1. Introductory Overview: Resistive Plate Chambers

Gaseous detectors have historically played and continue to play a fundamental role in the field of nuclear and particle physics experiments. Their versatility allows for economical production, adaptable to both planar and cylindrical geometries tailored to specific applications. In the realm of high-energy physics (HEP), the demand for enhanced spatial and temporal resolutions led to the prominence of planar geometries. This shift was catalyzed by the introduction of high-time-resolution spark counters with localized discharge, a groundbreaking development pioneered by Parkhomchuck et al. in 1971 [113]. Subsequently, the innovation continued in 1981 with the proposal of Resistive Plate Chambers (RPCs) by Santonico and Cardarelli [114], marking a significant milestone. This novel class of detectors seamlessly integrated into a myriad of HEP and astroparticle physics experiments, demonstrating their adaptability and efficiency. Beyond their roots in fundamental physics, RPCs and related resistive gaseous detectors have found applications in diverse fields, ranging from medical imaging [115] to various muography scenarios.

One of the distinctive advantages of RPCs lies in their straightforward and cost-effective design, facilitating their production over large areas. These detectors operate continuously with electronic readout capabilities. In contemporary settings, RPC systems achieve remarkable spatial resolutions, potentially reaching approximately 50 μm, temporal resolutions below 50 ps, and boasting nearly 100% detection efficiency. These exceptional qualities position RPCs as highly attractive detection technologies for muography applications.

Moreover, RPCs have evolved dynamically, incorporating diverse working modes [116–118], gas combinations [119, 120], and designs [121, 122]. Their

affordability coupled with large detection areas has made them indispensable components in different experiments such as CMS [123], ATLAS [124], ALICE [125], CALICE [126], and various muography detectors [82, 83]. This evolution underscores their pivotal role in advancing scientific exploration and reinforces their status as foundational tools in the field of particle detection.

4.1.1. Resistive Plate Chambers basics

RPCs are parallel-plate gaseous detectors with a simple design depicted in Figure 4.1. The active medium of an RPC is the uniform and thin gas gap (~mm) situated between two parallel plates made of highly resistive material. Each plate is coated with a conductive layer on its outer surface, allowing the application of high voltage to establish a uniform electric field within the gap. This gap is filled with a specific gas mixture, serving as the detector active medium. When energetic charged particles pass through the gap, they ionize the gas molecules. The strong electric field propels the liberated free charges—electrons and ions—toward the electrodes, leading to electron multiplication through avalanching in the gas. This phenomenon, known as a Townsend avalanche, entails an exponential increase in the number of free electrons with every colliding electron liberating more electrons. This charge movement induces electronic signals on external readout boards equipped with metallic strips or pads, providing 1D or 2D positional information based on the deposited charge.
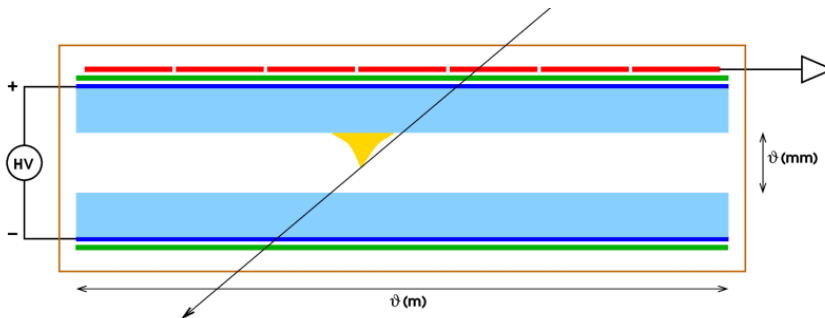
Figure 4.1. ❘ Illustration of a single-gap RPC: The gas space is confined between resistive electrodes (light blue) coated with a semiconductive layer (dark blue) on their outer surfaces. These electrodes are protected by insulating layers above and below (green). When charged particles traverse the active area, they ionize the gas, triggering an avalanche effect (yellow) and generating a signal on the strips or pads of the readout board (red). From [127]

In this context, the number of ion pairs generated per unit path length is directly proportional to the total initial number of ion pairs. Let Q represent the total charge produced by the avalanche process:

$$Q = n_0 \cdot e_0 \cdot M \tag{4.1.}$$

Where:

- n_0 : number of original ion pairs
- M : multiplication factor
- e_0 : charge of the electron

The fractional increase in the number of charged pairs per unit length adheres to the Townsend equation:

$$\frac{dn}{dx} = \alpha \cdot n \Rightarrow n(x) = n_0 \cdot \exp(\alpha \cdot x) \tag{4.2.}$$

Where,

- n_0 : number of primary ion-pairs
- α : First Townsend coefficient indicating the number of collisions leading to ionization per unit length of the particle track.
- x : Distance from the anode.
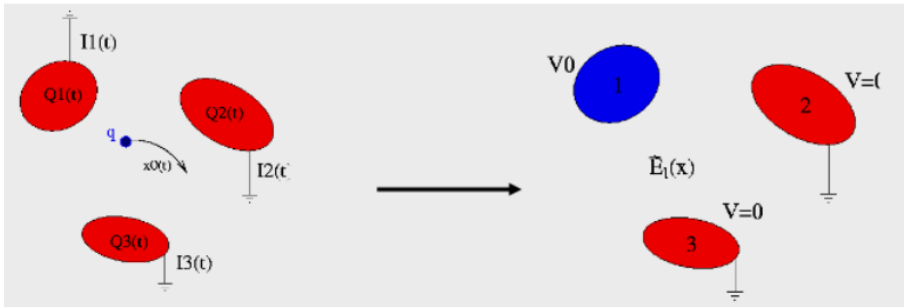
Figure 4.2. ❘ Visualization of Ramo's theorem and the concept of the weighting field enables the calculation of the induced current on a grounded electrode caused by a charge q moving along a trajectory $x_0(t)$. Figure from [128].

The signal induced on the readout electrodes, whether strips or pads, is commonly calculated using the Shockley–Ramo theorem [129, 130], often formulated with the aid of the "weighting field" E_w [131]. To compute this E_w, the readout electrode ideally assumes a "weighting potential" $V_w = 1$, while all others are set to 0 (refer to Figure 4.2). The resulting field, calculated as if computing an electrostatic field under these specific conditions, represents the weighting field E_w (relative to the weighting potential V_w). The theorem asserts that the induced current on the readout electrode by a charge q is expressed by the simple formula:

$$i(t) = \vec{E_w}(\vec{x}) \cdot \vec{v_D}(t) \cdot q \tag{4.3.}$$

where v_d is its drift velocity.

RPCs commonly employ Bakelite and glass as resistive electrodes. Bakelite, a High-Pressure Laminate, is produced from layers of paper impregnated with synthetic resin. Typically coated with linseed oil [132] for a smooth electrode surface and improved noise characteristics, Bakelite exhibits resistivity on the order of 10^{10-12} Ωcm. However, its resistivity is influenced by factors like environmental humidity [133], necessitating the use of a humidified gas mixture. In contrast, glass electrodes, ranging from regular float glass to specialized materials, can have resistivity values in the range of $10^4$to 10^{16} Ωcm. Glass electrodes offer superior surface quality and do not require humidified gas mixtures, although their production costs, depending on the type, can be significantly higher. Stable environmental conditions are critical for proper detector operation since the resistivity of both Bakelite and glass is affected by temperature fluctuations [134].

RPCs can operate in two modes based on the applied electric field. Historically, RPCs were predominantly used in streamer (or spark) mode. However, as RPC efficiency rapidly drops with increasing particle rates, they are more frequently operated in avalanche mode nowadays in experiments at accelerators. In this mode, moderate electric fields limit the amount of charge created in the gas, making it easier to detect the avalanche. Additionally, this mode helps mitigate detector aging effects caused by chemical processes within the gas volume [135, 136], which are assumed to be proportional to the total integrated charge encountered by the chamber.

RPCs have achieved intrinsic spatial resolutions of approximately 50 μm [137]. To enhance detection efficiency, a double-gap layout can be employed, where signals from two stacked RPC gas gaps are simultaneously captured by a single set of readout electronics (refer to [138, 139] for details). Due to the thin gas gap, RPCs exhibit short response times, on the order of nanoseconds. To further improve time resolution, Multi-gap RPC (MRPC) layouts were introduced in 1996 [140]. Advanced MRPCs, comprising a large stack of sub-millimeter-sized gaps [141], have achieved impressive time resolutions of 20-50 ps, as demonstrated by [142, 143].

4.1.2. Gas Mixture

Selecting the appropriate gas mixture for RPCs poses a considerable challenge, given that the gas is fundamentally essential for gaseous detectors. RPCs necessitate gas mixtures with specific characteristics:

(A) **High density of primary ion-electron clusters:** This ensures high detection efficiency and depends on factors such as particle energy deposition (calculated using the Bethe–Bloch formula), the gas mixture's average atomic number, density, and specific ionization potential.

(B) **Relevant "photon-quenching" properties:** The gas should exhibit low photon emission and/or transmission to minimize photon feedback phenomena.

(C) **Electronegativity:** The gas should be electronegative to reduce the lateral extent of discharges and enhance their localization.

(D) **Safety:** Ideally, the gas should not pose health hazards.

Additionally, desirable traits include:

1. **Limited production of aggressive chemicals and polymerization materials:** Chemical processes during electron multiplication should not produce aggressive chemicals like hydrofluoric acid, which can damage chamber and gas system components, or form unwanted deposits on the plates.

2. **Eco-friendly properties:** The gas mixture should have a negligible ozone depletion power (ODP) and low global warming potential (GWP) when released into the atmosphere to minimize damage to the ozone layer and the greenhouse effect, aligning with international protocols like the Kyoto Protocol.

Various gas combinations have been tested extensively to fulfill the essential criteria for RPCs. Specifically, for RPCs operated in avalanche mode, specific gas mixtures are used, typically comprises three primary gases:

- Tetrafluoroethane ($C_2F_4H_2$), commonly known as Freon or R134a, constitutes the predominant component, accounting for over 90% of RPC gas mixtures. Its usage is attributed to its high effective Townsend coefficient, enabling the detector to function with a higher threshold compared to gases like Argon. Operating under similar conditions with Argon would necessitate a stronger electric field, leading to a higher proportion of streamers and consequently restricting the detector's rate capability.

- Isobutane ($i\text{-}C_4H_{10}$), present in a minor proportion within gas mixtures, is employed for its ultraviolet (UV)-suppressing properties. It serves the purpose of preventing avalanche streamers induced by UV photon emission.

- Sulfur hexafluoride (SF_6) is utilized in minimal amounts due to its significant electronegativity. This compound absorbs surplus electrons, preventing the formation of streamers. However, a percentage of SF_6 exceeding 1% does not offer additional benefits in terms of streamer cancellation power but elevates the operating voltage.

Research efforts, particularly at CERN, are dedicated to discovering environmentally friendly gas mixtures that enhance RPC efficiency and sustainability [144,145]. The initial use of CF_3Br, which was harmful to the ozone layer and subsequently banned in the 1990s, led to the gradual incorporation of tetrafluoroethane into RPCs, enabling them to operate in avalanche mode. Despite

these advancements, the search for an optimal RPC gas mixture continues to be a complex and ongoing endeavor due to the multitude of potential candidates, various gas combinations, and different percentages that could, in principle, be utilized.

4.1.3. Resistive coating

The resistive layers in RPC detectors play a critical role. These layers are responsible for receiving the working voltage and ensuring its uniform distribution across the electrode surface. This uniform distribution is vital to maintain a homogeneous electric field across the gas gap. Additionally, these layers are instrumental in dissipating the charge generated during an avalanche event.

A key parameter that must be precisely controlled is the surface resistivity of these layers, which is expressed as Ohm/square ($\Omega/\square$). If the surface resistivity is too low, typically less than a few hundred $k\Omega/\square$, the signals induced by the avalanche will spread across the resistive layers over a large area. This results in the formation of large signal clusters [146]. On the contrary, if the surface resistivity is excessively high, a significant electric potential difference will develop along the surface of the detector.

In cases where RPCs are of substantial size or operate under high irradiation conditions, this high resistivity can lead to a reduced effective working voltage, especially in regions far from the point where the voltage is injected. To mitigate these issues, it is crucial to regulate the surface resistivity within a specific range, typically between several hundred $k\Omega/\square$ and several $M\Omega/\square$ [147].

Resistive layers are commonly constructed using materials such as graphite, carbon-based inks [148], or conductive sheets. Proper adjustment of the surface resistivity ensures optimal signal propagation, cluster formation, and overall detector performance in RPC systems.

4.2. First prototype

Our first experimental setup [149] comprised four planes of gRPC detectors, arranged as illustrated in Figure 4.3 (c). To maintain a distance of $14.8cm$ between the second and third planes, we utilized removable vertical bars. Each detector, depicted in Figure 4.3 (f), featured 16 sensitive strips with a $1cm$ pitch and a width of $0.9cm$. These detectors were housed in gas-tight aluminum boxes measuring $38 \times 29 \times 3.7cm^3$ (see Figure 4.3 (a)), with each plane weighing $6.5kg$. The first and third detectors were positioned orthogonally to the second and fourth ones, enabling bidimensional information (x and y orientation) to be collected at the top and bottom of the telescope. The detectors were operated with a gas mixture comprising freon (95.2%), SF6 (0.3%), and isobutane (4.5%), maintained at a slightly higher pressure than atmospheric. Prior to filling the detector casings with the operating gas, stringent leak tests were conducted.
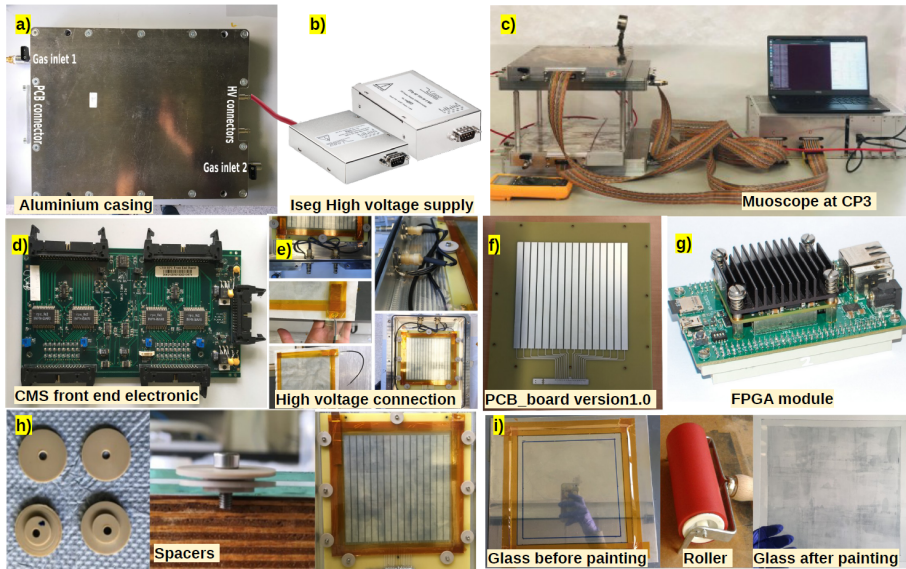
Figure 4.3. ❘ Experimental setup elements [128]. a) Aluminium casing. b) Iseg high voltage supply. c) Muoscope at CP3/UCLouvain with DAQ. d) CMS front end electronic board. e) High voltage connection. f) Version 1.0 readout board. g) FPGA module. h) Round spacers. i) Resistive coating.

Vacuum tests were performed, followed by a helium check to identify and rectify any leakage points. Initially, a few leaks were detected, but after necessary adjustments, we achieved an impressive leak rate of $10^{-9}mbar.l.s^{-1}$.

The glass sheets serving as electrodes were cut into square shapes measuring $20\times20cm^2$ and were $1.1mm$ thick. To create a uniform gas gap, we applied a resistive coating to the glass using a colloidal dispersion of antimony-doped tin oxide 'CP10MC' in water (20% powder, 80% water) mixed with an equal amount of methanol. The application process was precise, with a magnetic stirrer used to achieve a perfect blend. After cleaning the glass plates thoroughly, a uniform coating was applied using a roller. To maintain consistent spacing between the glass sheets, we inserted nine round edge spacers made from PEEK (polyether ether ketone) material with a diameter of $2cm$ and $1.1mm$ thick. For signal processing, we utilized front-end electronic boards (FEB) identical to those employed in the RPCs of the CMS experiment, illustrated in Figure 4.3 (d). Each FEB comprised four front-end modules, each housing 8 channels. Consequently, one FEB served two detectors. Each channel included an amplifier with a charge sensitivity of $2mV/fC$, a discriminator, a monostable, and an LVDS driver, which convert the digitize pulse to a signal that could read by FPGA (see Figure 4.3 (g)). Upon detecting a pulse, an $80ns$ time window opened, during which all pulses were combined using a logic OR operation

across all channels.

The external computer establishes a connection with the data acquisition (DAQ) either through an Ethernet port or WiFi. It offers a user-friendly GUI for controlling the DAQ, although it also supports command-line operations via the terminal. The computer is responsible for configuring essential parameters such as thresholds, monostable values for data acquisition, and high voltage settings. Additionally, it continuously monitors these parameters. Upon receiving commands from the external computer, the DAQ's internal CPU communicates high voltage values to the high voltage controller, threshold and monostable values to the CMS FEE, and configures the FPGA for data acquisition. Once the data acquisition starts, the CPU oversees the process, ensuring smooth operation, and saving the acquired data onto the SD card.

4.3. External trigger

In the initial muoscope prototype, RPCs were employed in a self-trigger mode, thanks to their very fast signal formation. Our default global trigger logic required a signal to be observed in all RPCs to acquire an event, interpreted as the passage of a muon. However, this configuration presented challenges in accurately assessing RPC performances, particularly in the presence of significant noise. To overcome this limitation, we introduced an external trigger system. This addition streamlined our studies on RPC efficiency and fake rate measurements.

Our external trigger setup comprises two plastic scintillator slabs, precisely sized to match the active area of our gRPCs ($16cm \times 16cm \times 2.9cm$). These scintillators are housed in black plastic boxes, featuring secure mounting mechanisms for photomultiplier tubes (PMTs). Coupled with Hamamatsu H11411 PMTs, these scintillator slabs are strategically positioned above and below our telescope.

This section delves into a comprehensive exploration of our external scintillator setup, detailing its design, calibration, and performance evaluation.

4.3.1. Assembling process

The production and assembly process took place in several stages. Initially, two plastic housings were meticulously crafted, and two plastic scintillators were precisely cut to specific dimensions ($16cm \times 16cm \times 2.9cm$) and polished with care to enhance light transmission. The housing for the plastic scintillators was skillfully designed by Nicolas Szilazi, CP3's mechanical engineer, as illustrated in Figures 4.4, 4.5. To secure the scintillators, four plastic pillars were strategically placed at the box's bottom corners, while a rectangular component was affixed to the box's lid. This rectangular piece was instrumental in holding the scintillators securely in place.
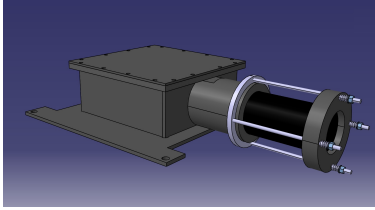
Figure 4.4. | Computer-aided design (CAD) representation showcasing the external appearance of the finalized external trigger setup.
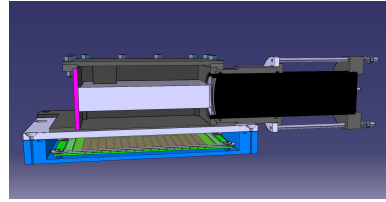
Figure 4.5. | The housing cross-section for the trigger scintillator, with the plastic scintillator represented by the white box.

On one side of the housing, a hole with a diameter of 6 cm was integrated, connecting to a 3D-printed frame designed for mounting the Hamamatsu H11411 PMT. At the bottom of the housing, four holes were meticulously aligned with the corresponding holes in the aluminum box. This precise alignment ensured that the scintillators were perfectly positioned over the RPC's active area. To attach the PMT properly, a spring mechanism was employed, along with long screws.

In the subsequent steps, white reflecting sheets were wrapped around the polished scintillators, excluding the PMT hole. This wrapping enhanced the reflection of scintillating light towards the photocathode. Small pillars were affixed to the bottom corners of the plastic box, guaranteeing the precise alignment of the scintillator.

During the final phase, optical grease was carefully applied to the photocathode, and the PMT was securely attached to the box using long screws. The application of optical grease optimized the optical contact between the PMT's scintillator and photocathode. Once the PMT was secured, the box's cover was placed and firmly secured with 16 nuts and bolts. To prevent any potential light leakage, black tape was applied to seal all edges. The completed system is illustrated in Figure 4.6.

4.3.2. Testing processes

After assembling the two scintillator detectors, the subsequent step involves calibrating the system and evaluating the PMT output for cosmic muons. To initiate this process, it is essential to power up the PMT. This particular PMT integrates a high-voltage supply, requiring only a control voltage supply ranging from 0.5 V to 1.8 V to regulate the gain, as illustrated in Figure 4.7 [150]. The precise control voltage needs calibration based on experimental data. A specialized circuit, depicted in Figure 4.4, was developed to power the PMT and adjust its control voltage.
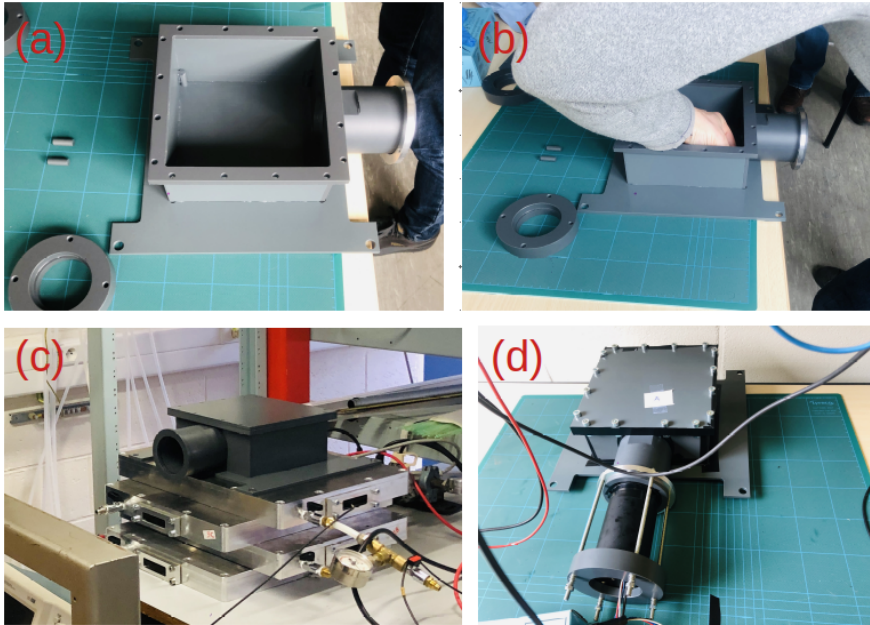
Figure 4.6. | Assembly process of the external trigger.
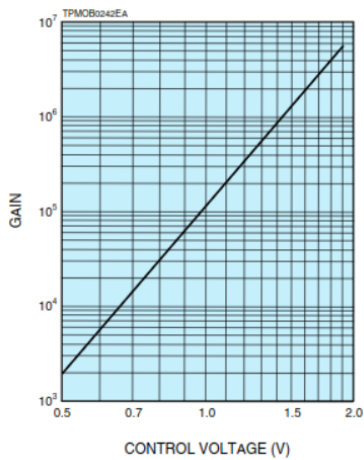
Figure 4.7. | The gain of the PMT with respect to the control voltage [150].
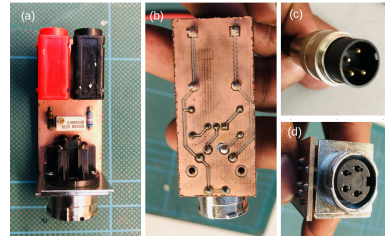
Figure 4.8. | (a) Potentiometer board and banana connectors (colored in red and black) along with a DIN female connector, (b) Rear view of the board, (c) DIN 4 male connector, (d) 71251-040/0800 DIN female connector.

This control unit features two banana female connectors, capable of powering the system with a +15 V power supply, and a 67WR500KLF trimmer poten-

tiometer [151] that can be adjusted using a screwdriver to modify the PMT's control voltage. Additionally, it incorporates a 71251-040/0800 DIN female connector [152] compatible with a DIN 4 male connector. This unit, designed and assembled in the CP3 Electronic lab, includes a pin for monitoring the control voltage via a voltmeter. Before introducing this trigger system to the muoscope, two crucial calibrations must be performed:

1. Control voltage calibration.
2. Threshold calibration for the discriminator.
3. Efficiency assessment of the two scintillators.

For these calibrations, the following modules and instruments were utilized:

- QL355TP dual channel power supply. [153]
- LeCroy quad discriminator (Model 821CS) module
- LeCroy quad coincidence (Model 622) module
- CAEN N415A 8 Ch autowalk constant fraction discriminator(CFD) [154]
- Dual timer (IPC type 2255 series)
- Two dual scalers (IPC type DS2)
- Preselection timer counter
- NIM power supply (IPC NPS 100)
- Tektronix TDS 3014 four channel digital oscilloscope [155]
- LEMO cables and onnectors
- delay module

The external trigger setup involved two scintillators named "top (A)" and "bottom (B)". Each was powered individually by the QL355TP dual-channel power supply, with the control voltage set to 1.75 V (the reference value from the data-sheet [102]). The PMT output was connected to the Tektronix TDS 3014 four-channel digital oscilloscope via a standard LEMO connector. The signal observed for cosmic particles is illustrated in Figure 4.9

To evaluate the trigger system's performance, a coincidence circuit was designed with two PMTs. Two scintillator boxes were positioned one above the other. The signals from both PMTs were sent to the LeCroy quad discriminator (Model 821CS) module for digitization. However, it was observed that PMT B was faster than PMT A, requiring a signal delay from 15 to 35 nanoseconds, which was not stable. After using the CAEN N415A 8 Ch autowalk constant fraction discriminator (CFD), a stable delay of 18–20 ns was achieved.

Once the signals were in the same time window after adjusting the delay, the coincidence module received both signals. The coincidence window's time was set to 70 ns (Figure 4.10), finalizing the setup for control voltage calibration.
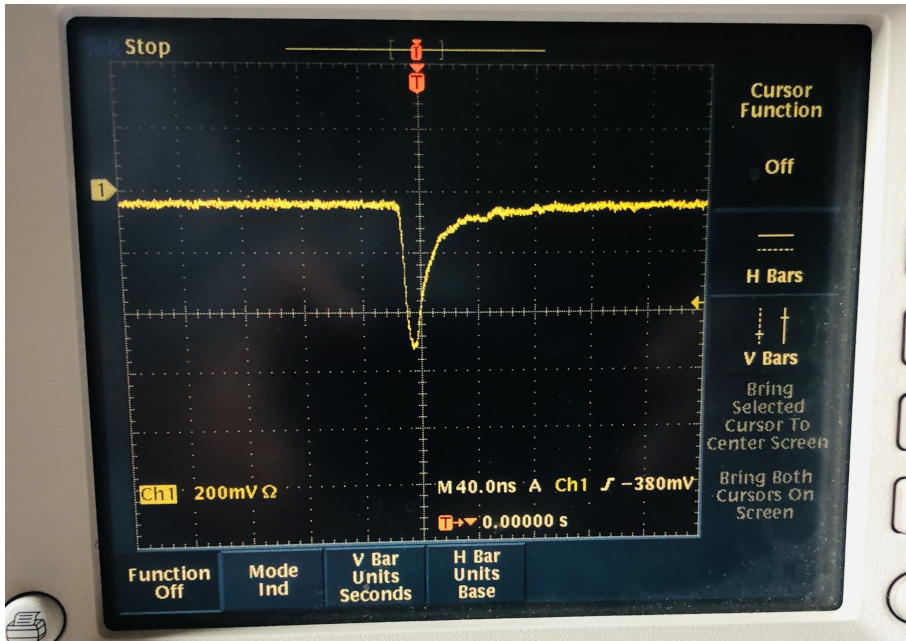
Figure 4.9. ǀ Oscillogram showing the scintillator signal from the Top(A) PMT. The oscilloscope has an input impedance of 50Ω, a voltage scale of 200 mV per square, and a time scale of 40 ns per square. The oscilloscope trigger is set at -380 mV.

4.3.3. Calibration procedure

In scenarios where photomultiplier signals are analyzed using a discriminator, a common method to determine the operational voltage is through plateau measurements. This technique involves systematically adjusting the applied photomultiplier voltage while observing the total count rate from the counter-discriminator, similar to the approach used for Geiger counters [156]. Utilizing the external trigger setup (see Figure 4.11) and an additional timer, the experimental setup was optimized by adjusting the distances between the two scintillators to maximize the solid angle, as depicted in Figure 4.12.

To find the optimal operational voltage for each PMT, one PMT's control voltage was set to the upper limit of 1.8 V, following the specifications for the H11411 PMT. The total coincidences between the two PMTs were then recorded over a 100-second period while systematically adjusting the control voltage of the other PMT from 0.5 V to 1.8 V. Analyzing the plot of coincidences versus controlled voltage (Figure 4.13) revealed a clear plateau. Using this plot as a reference, the optimal operational voltage for each PMT was determined to be the midpoint of the observed plateau, specifically 1.25 V for both PMTs.

After setting the control voltage to 1.25 V, the next step involved determining
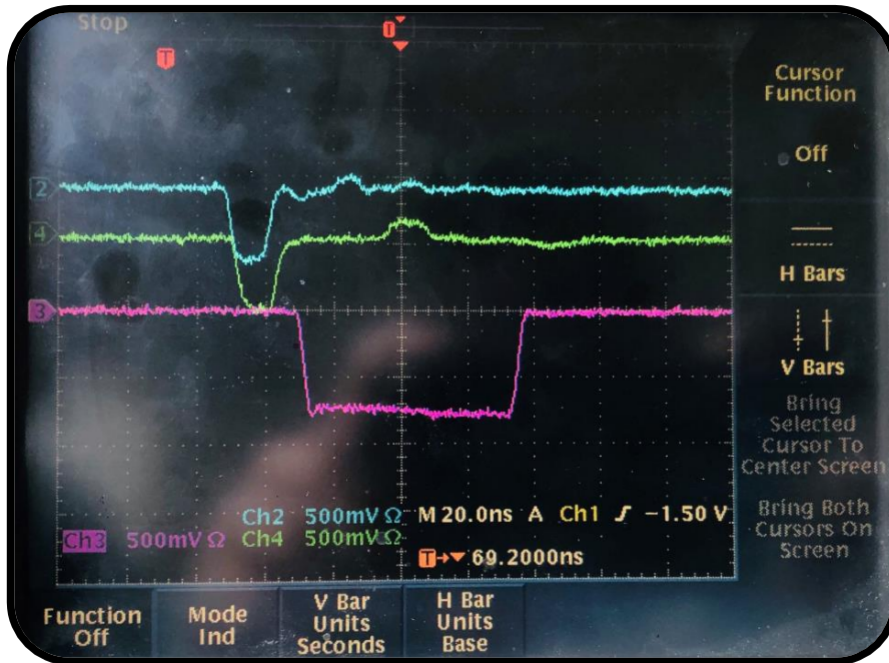
Figure 4.10. | The coincidence signal (shown in pink) within a 70 ns window, with two digitized signals from PMT A (shown in blue) and PMT B (shown in green).

the optimal discriminator threshold. The same strategy was employed: one PMT's discriminator threshold was set to the lower limit of the eCroy quad discriminator (Model 821CS) module at -0.3 V (-30 mV). The total coincidences between the two PMTs were recorded over a 100-second period while systematically adjusting the threshold value of the other PMT from -0.3 V to -1.5 V.

Upon analyzing the coincidence plot depicted in Figure 4.14, it became clear that the counts exhibited minimal variation within the range of -0.3 V to -1.5 V. As a result, any value within this range could be suitable. Therefore, a threshold value of -0.5 V was selected as the discriminator threshold for both PMTs.

4.3.4. Efficiency studies

With the PMTs threshold values and control voltages now optimized, the subsequent phase involves evaluating the efficiency of each PMT individually. To accomplish this, two sets of Hamamatsu R9800 PMTs paired with $10cm \times 10cm$ scintillators were utilized. The setup was simple: the Hamamatsu R9800 PMTs,
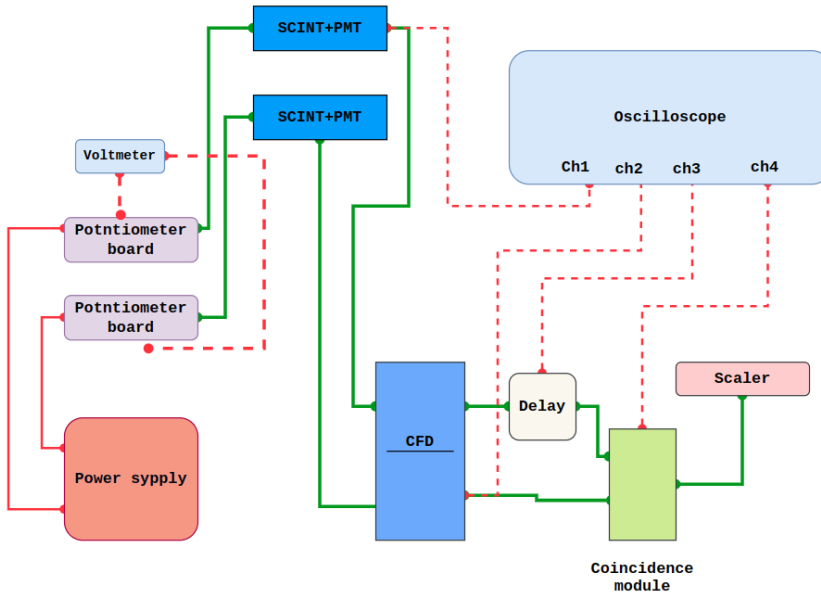
Figure 4.11. ∣ Schematics of a coincidence circuit with two scintillator + PMT Setup.

previously calibrated for high voltage and threshold values, were labeled as 'Top' and 'Bottom'. These PMTs were positioned, sandwiching the external trigger setup, as illustrated in Figure 4.15.

For these PMTs (Hamamatsu R9800: Top and Bottom), the necessary high voltage was supplied by the CAEN HV module, and using the LeCroy quad discriminator (Model 821CS) module the signal thresholds were established, as indicated in Table 4.1.

Table 4.1. ∣ Setting parameters for PMT units used in efficiency calculations.

Scintillator dimensions	Threshold/V	High voltage/V
Top (10cm × 10cm)	- 0.4978	1450
A (16cm × 16cm)	- 0.5018	1250[*]
B (16cm × 16cm)	- 0.5006	1250[*]
Bottom (10cm × 10cm)	- 0.5030	1450

[*] This is the high voltage corresponds to the control voltage of 1.25 V in PMT [150]

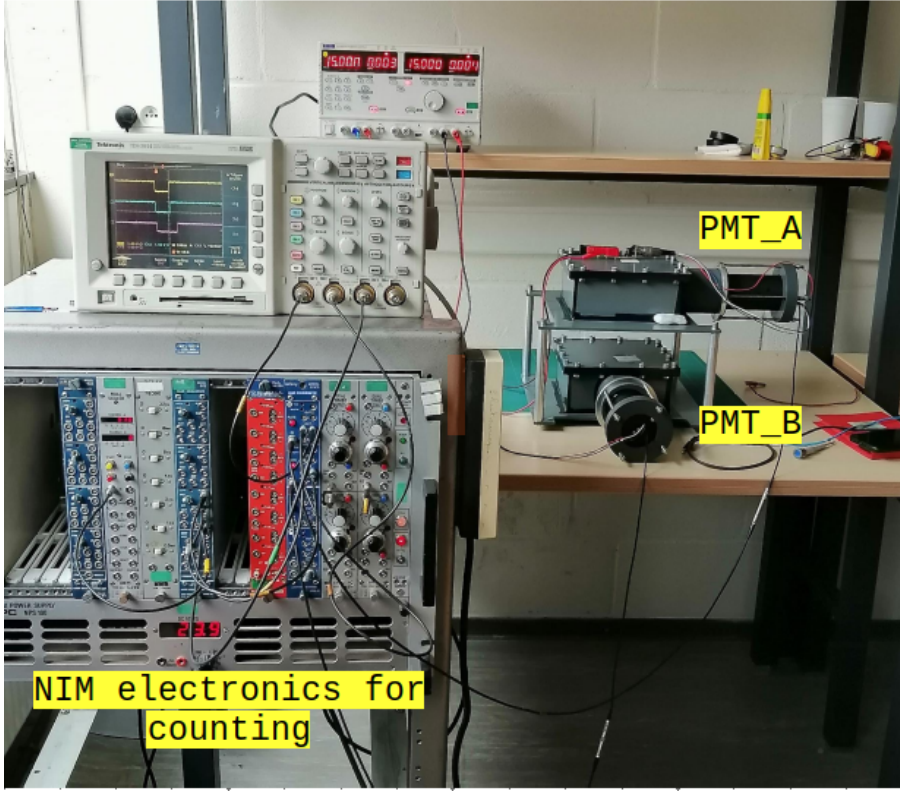Efficiency calculations were carried out using the following logic in eq. 4.4 and eq. 4.5:

Figure 4.12. ❘ Setup for the calibration for the control voltage.

$$Efficiency_A(\epsilon_A) = \frac{Top \cap Bottom \cap A}{Top \cap Bottom} \times 100\% \qquad (4.4.)$$

$$Efficiency_B(\epsilon_B) = \frac{Top \cap Bottom \cap B}{Top \cap Bottom} \times 100\% \qquad (4.5.)$$

Throughout a 30-minute data collection period, counts were recorded for both the numerator and denominator configurations of these equations (eq 4.4 and eq 4.5). Subsequently, the efficiency of each scintillator system was computed, resulting in efficiencies of $\epsilon_A = 93\% \pm 0.9\%$ and $\epsilon_B = 90.5\% \pm 1.1\%$.

4.3.5. Implementation of external trigger

Integrating the external trigger system into the RPC marked the system's next phase. Prior to its connection to the muoscope data acquisition system, the delay between the RPC and PMT signals was measured, considering the RPC signal's faster pace compared to the PMT signal.

Utilizing two unused I/O pins in the FPGA [157], two wires were soldered
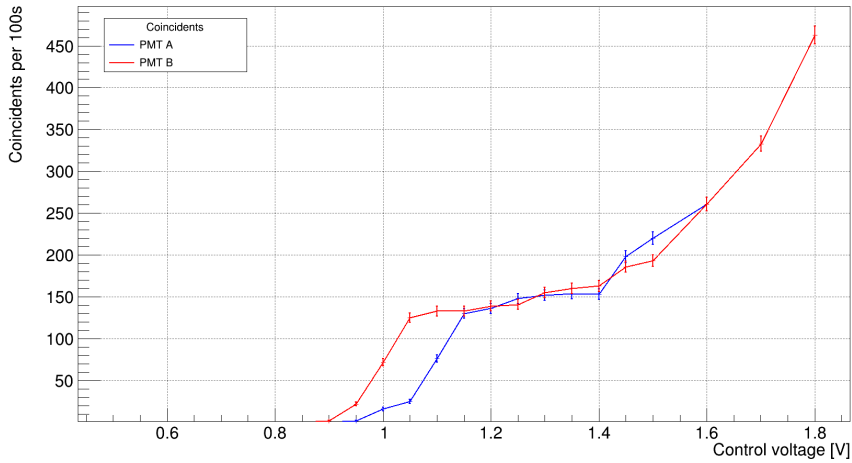
Figure 4.13. ❙ The graph illustrate how coincidence counts for both PMTs change with respect to the control voltage. The plateau for PMT A (blue curve) falls within the range of 1.15 V to 1.4 V, while for PMT B (red curve), it extends from 1.05 V to 1.4 V
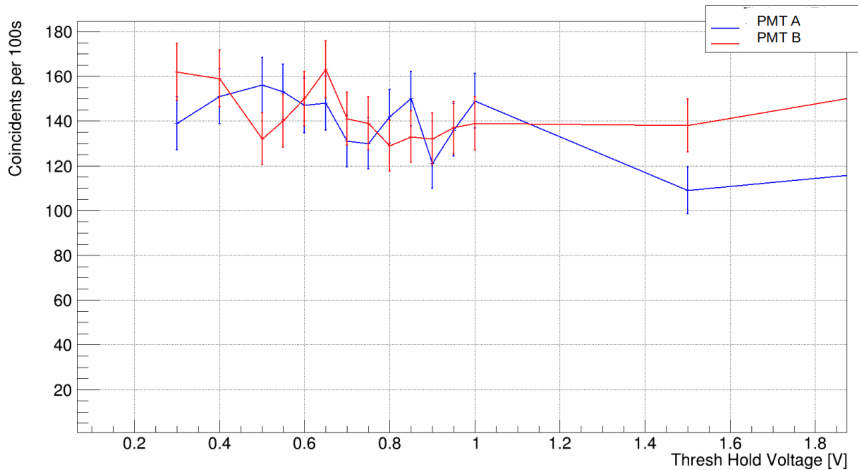

Figure 4.14. ❙ Plot showing the variation of coincidence counts for both PMTs with respect to the discriminator threshold.

onto the FPGA board to function as inputs for the signals from two PMTs. The CAEN CFD module [154] discriminated the PMT signals, after which the discriminated signal was directed to the timer module to serve as a one-shot. This one-shot signal was transformed into an LVDS signal using an LVDS drive,
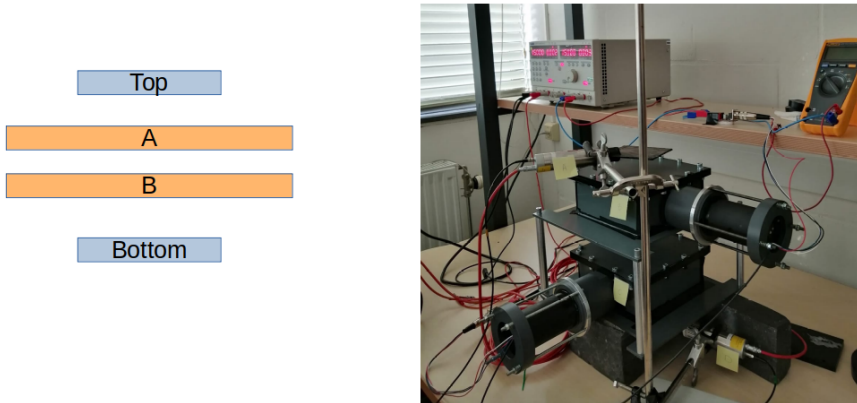
Figure 4.15. ❙ Configuration of PMTs for evaluating the efficiency of the two scintillators.
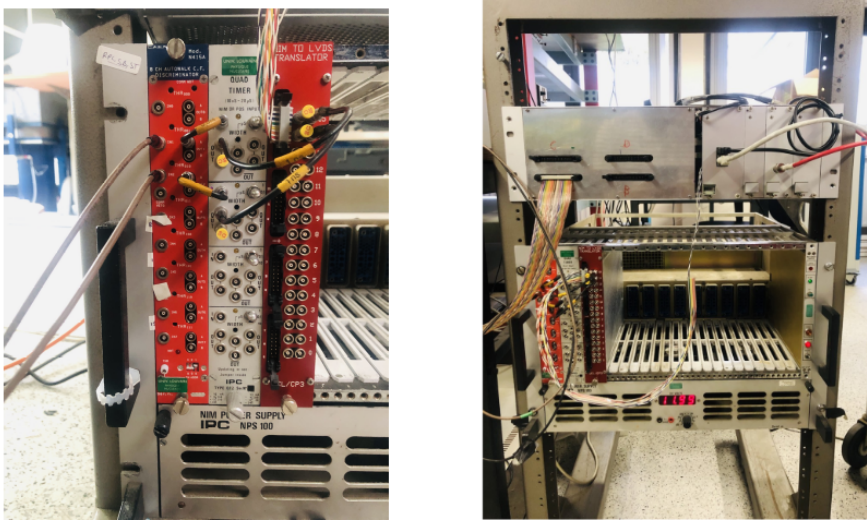
Figure 4.16. ❙ Three modules employed to integrate the external trigger to the DAQ system (left). The electronic setup of the DAQ system with the integrated external trigger (right).

feeding it into the FPGA in the DAQ system (Figure 4.16). The signals from the one-shot unit and LVDS units are showed in Figure 4.17.

Within the DAQ software, the 2 least significant bits of the time buffer were used to store data from the 2 PMTs. The monostable value was set at 40 ns after confirming that the signal met the FPGA's criteria in the DAQ.
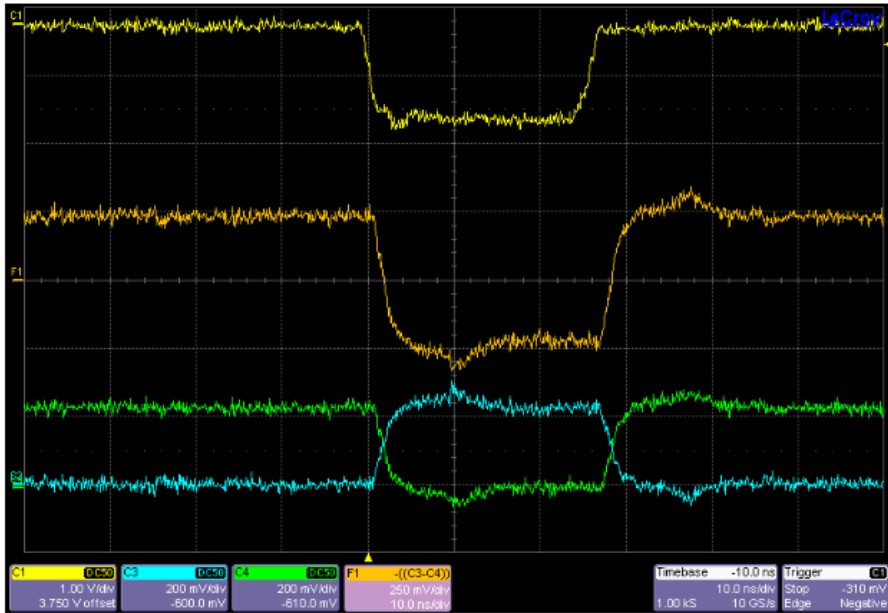
Figure 4.17. | Oscillogram of the LVDS output and monostable output. Channel 1 (yellow) represents the monostable output, while channels 3 and 4 (blue and green respectively) depict the outputs from two lines of the LVDS module.

PMT counts were obtained from the same dataset using both a DAQ and an external NIM counter, confirming the system's functionality as indicated in Table 4.2.

Table 4.2. | DAQ and External counters hits.

| Counter	Top PMT	Bottom PMT	coincidence
DAQ	2470	3511	614
NIM Ex. counter	2474	3512	614

Details regarding the modifications made to the DAQ program for implementing the external trigger are discussed in the performance study section 4.6.5.

4.4. Resistive plate production

As mentioned earlier in subsection 4.1.3, the accurate calibration of surface resistivity in the resistive coating layers holds significant importance. In this section, we delve into various versions and methods of coating glass plates. However, it is essential to first touch upon surface resistivity measurement and the diverse configurations employed for this purpose.

4.4.1. Surface resistivity

It is common to find confusion between two closely related terms: surface resistance "R_s" and surface resistivity "ρ_s".
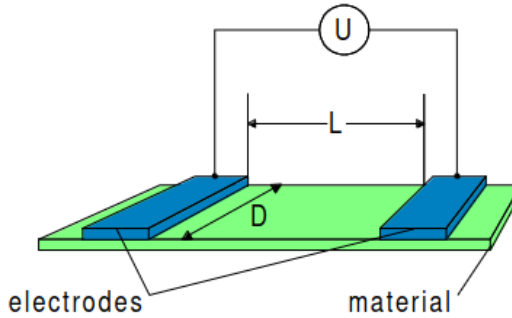
Figure 4.18. Basic setup for surface resistance and surface resistivity measurement [158].

Surface resistance "R_s" universally refers to the ratio of a DC voltage "U" to the current "I_s" flowing between two electrodes of a specific configuration that are in contact with the same side of the material under examination (eq. 4.6).

$$R_s = \frac{U}{I_s} \tag{4.6.}$$

On the other hand, surface resistivity "ρ_s" is determined by the ratio of the DC voltage drop "U" per unit length "L" to the surface current "I_s" per unit width "D" (in the case of the configuration illustrated in Figure 4.18).

$$\rho_s = \frac{\frac{U}{L}}{\frac{I_s}{D}} \tag{4.7.}$$

It represents an inherent property of the material and ideally remains constant regardless of the method or configuration of the electrodes used in the measurement. It is crucial to note that the result of a surface resistance measurement depends on both the material and the geometry of the electrodes used. The unit of surface resistivity is Ohm (Ω), which also serves as the valid unit for surface resistance. To alleviate potential confusion between these terms, surface resistivity is sometimes expressed as Ohm/square ($\Omega/\square$), although this notation lacks dimensional validity [158].

4.4.2. Surface resistivity measurement

Surface resistivity can be evaluated using various electrode configurations in our laboratory. We employ two distinct measurement methods: one involving a

straightforward parallel electrode setup (depicted in Figure 4.18), and the other utilizing concentric ring electrodes (illustrated in Figure 4.19). By determining the surface current density between the electrodes, we establish the relationship between surface resistivity and surface resistance for each configuration.

In the case of concentric ring electrodes, the electric field intensity between the rings can be computed from the surface current density (as shown in Figures 4.19).
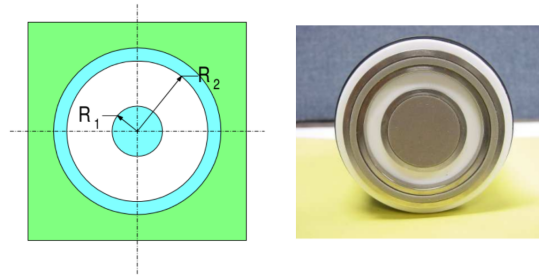
Figure 4.19. ❘ Left: Configuration for measuring surface resistivity using concentric ring electrodes (R_1: Outer radius of the center electrode, and R_2: Inner radius of the outer electrode). Right: Concentric ring probe. [158]

The surface current density (J_s) for the concentric ring electrodes is given by:

$$J_s = \frac{I_s}{2\pi r'}$$ (4.8.)

where the radius r' varies from R_1 to R_2. The relationship between current density "J" and electric field intensity "E" is described by Ohm's law, and valid surface currents are given by:

$$J_s = \frac{E}{\rho_s}$$ (4.9.)

From equations (4.8) and (4.9), E can be expressed as:

$$E = \frac{\rho_s I_s}{2\pi r'}$$ (4.10.)

The voltage (U_{R_1,R_2}) between electrodes can be found by integrating the electric field E from R_1 to R_2 :

$$U_{R_1,R_2} = \int_{R_1}^{R_2} E.dr$$

$$= \int_{R_1}^{R_2} \frac{\rho_s I_s}{2\pi r'}.dr \tag{4.11.}$$

$$= \frac{\rho_s I_s}{2\pi} ln\left(\frac{R_2}{R_1}\right)$$

From equations (4.11) and (4.6):

$$R_{s_1} = \frac{\rho_s}{2\pi} ln\left(\frac{R_2}{R_1}\right) \tag{4.12.}$$

After rearranging the equation, surface resistivity (ρ_s) is related to surface resistance (R_s) by a constant (k_1) that represent the geometry factor:

$$\rho_s = R_{s_1} \frac{2\pi}{ln\left(\frac{R_2}{R_1}\right)} = R_{s_1}.k_1 \tag{4.13.}$$

For ease of use, probes available on the market are designed with a straightforward integer value for k_1. For example, the probe used in our CP3 Lab has a coefficient factor of 10.

**Figure 4.20.** | Configuration for measuring surface resistivity using parallel electrodes.

In contrast, for the parallel electrode case, we utilize a simple setup designed by Nicolas Szilazi. It consists of two parallel copper electrodes with a width "D" of 4 cm, thickness "e" of 0.6 cm, and a distance "L" of 2.3 cm between them. Three ports are available to measure the resistivity between different parallel points, as depicted in Figure 4.20. In this configuration, the surface current density is determined as:

$$J_s = \frac{I_s}{P} = \frac{I_s}{2 \times (D + e)} \tag{4.14.}$$

where P is the perimeter of one electrode. Applying the same approach as with the ring electrodes, considering that the voltage between the two electrodes is $U = E \times L$, and referring to equation 4.9, surface resistivity can be expressed as:

$$\rho_s = R_{s_2} \times \frac{P}{L} = R_{s_2} \times k_2 \qquad (4.15.)$$

Here $k_2 = 4$ represent the geometrical factor for this particular case.
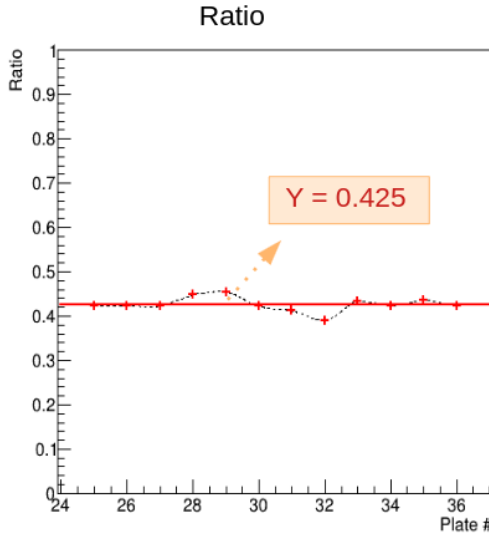
Figure 4.21. | The graph illustrates the measured ratio between R_{s_2} and R_{s_1} for different glass plates, with a corresponding fitting line corresponding to y = 0.425.

As ρ_s is not affected by the shape of the electrodes, unlike R_s, we examined the ratio between R_{s_2} and R_{s_1} for various glass plates (labeled from 24 to 36), as depicted in Figure 4.21. This verification ensured the reliability of both configurations, and as anticipated, we obtained a value of $\sim 0.4 \pm 0.02$.
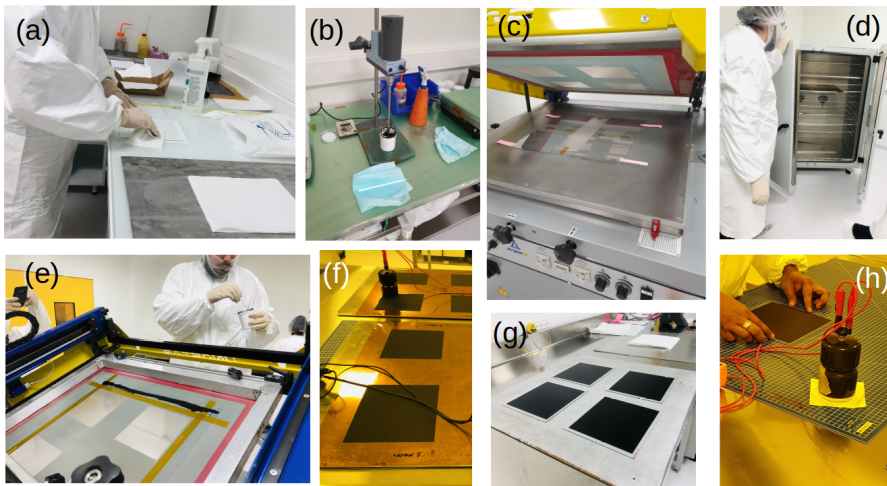
4.4.3. Resistive plate coating using serigraphy

Several methods are available for applying the semi-conductive coating, each varying in terms of automation, cost, and uniformity. In the first RPC prototype (see section 4.2), glass plates were manually coated with a paint roller, achieving a surface resistivity of about $0.3 M\Omega/\square$ [128]. However, this straightforward yet inexpensive technique led to non-uniformities of up to 200%, significantly impacting gRPC performance. This limitation drove our interest in serigraphy.

In serigraphy, also known as screen-printing, paint is transferred onto a surface, such as glass plates, leaving out areas where the stencil blocks paint penetration. We obtained glass plates with uniformly resistive layers from the CEA facility in
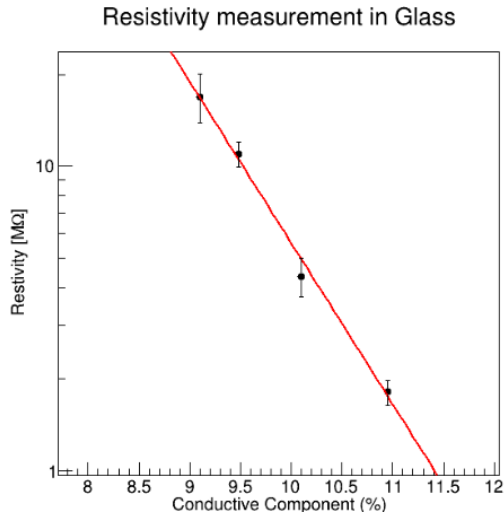
Figure 4.22. | Surface resistivity plotted against the conductive component of the paste. The black data points were utilized for fitting, producing the continuous red line represented by the equation $R = 13.94.e^{-1.22}$.

**Figure 4.23.** | Steps involved in producing the resistive plate using the serigraphy method.

Saclay, France. The initial step in serigraphy involves creating the conductive compound or paste. This paste was made by combining conductive EDAG PM 404 with the neutral EDAG 6017SS component. By adjusting the proportion of the conductive component in the mixture and measuring the resulting surface
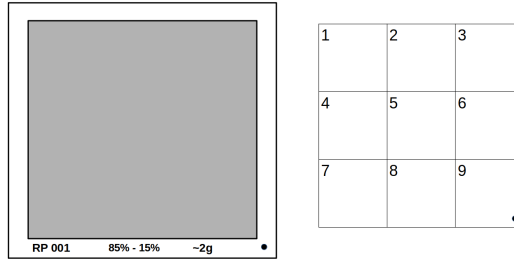
Figure 4.24. ❘ Left : Sketch illustrating labeled glass plates. Right: Nine specified positions marked for measuring paint surface resistivity.
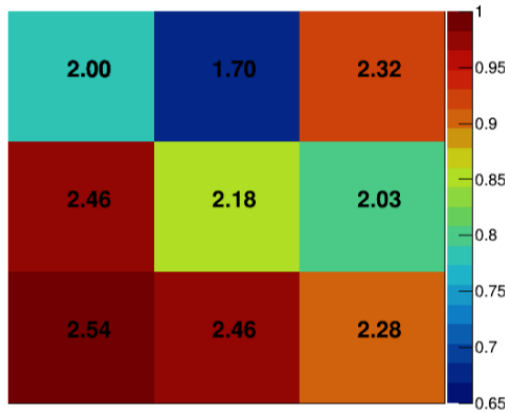

Figure 4.25. ❘ Measurement of surface resistivity (in $M\Omega/\square$) on one of the glass plates at 9 distinct locations. In the color code, a value of 1 corresponds to the highest value of surface resistivity.

resistivity, detailed alongside an exponential fit in Figure 4.22, the precise composition of the mixture was determined. For our glass plates, a 10.5% addition of the conductive component was necessary to achieve a surface resistance of $2M\Omega/\square$.

Following the mixture preparation, serigraphy was first performed on a kapton sheet before being applied to the glass surface. Subsequently, the glass underwent curing in an oven at 180°C for 4-5 hours. Figure 4.23 shows the steps involved in producing the resistive plates.

We produced eight "golden" glass plates with a surface resistivity of $2M\Omega/\square$ and monitored long-term variations. Measurements were taken at nine different locations on each glass plate (refer to Figure 4.24), and simultaneous readings of the lab's temperature and humidity were recorded during the resistivity measurements. Figure 4.25 displays a sample measurement for a single plate.

To study the enduring changes in surface resistivity, measurements on the selected glass plates began in February 2020. This assessment aimed to confirm the stability of resistivity over time and under varying environmental conditions, specifically temperature and humidity. The measured data, presented in Figure 4.26, reveal a discernible upward trend in surface resistivity over time. The extended gaps in the time axis correspond to the lockdown periods during
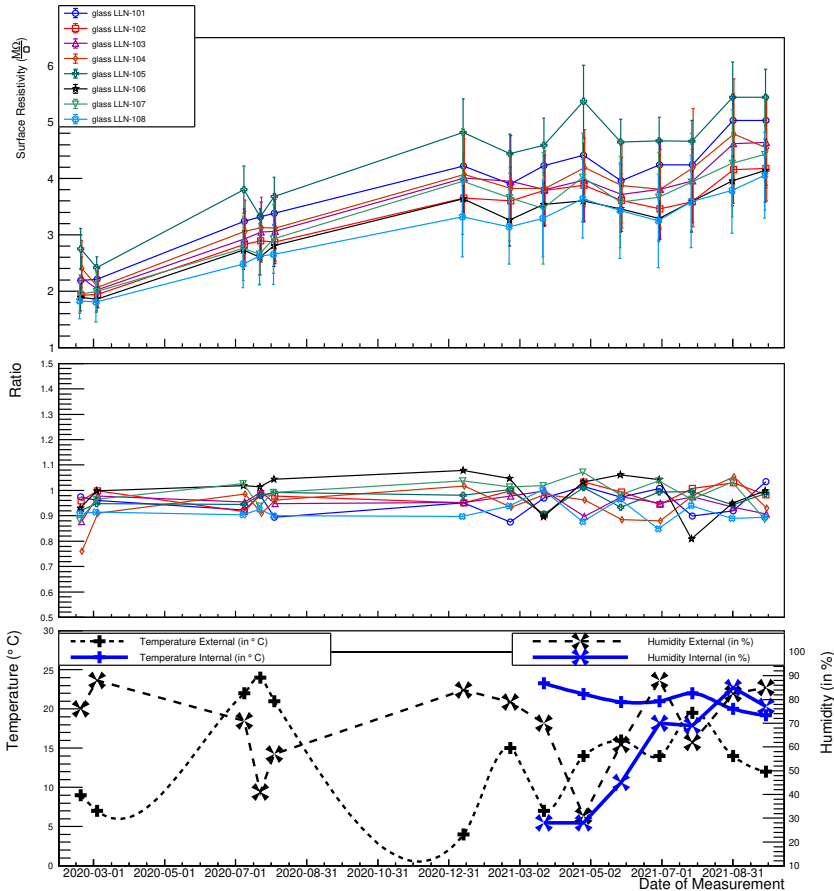
Figure 4.26. | Evolution of observables over time: Top: Average surface resistivity of eight selected glass plates with standard deviations at nine locations. Middle: Ratios of resistivity at the center to the average resistivity of other eight locations for each glass plate. Bottom: Temperature and humidity measurements from external weather data and internal Arduino-based sensor.

the Covid-19 pandemic in Belgium, restricting access to our laboratory. In the top panel of Figure 4.26, the average and standard deviation of the nine measurements for each glass plate at different times are depicted, displaying a

clear rising trend in surface resistivity. To assess spatial uniformity, the middle panel shows the ratio of the surface resistivity in the central region of each plate to the average of the other eight regions. Despite the overall increase in surface resistivity, these ratios have remained relatively constant. This stability is reassuring, indicating that non uniformity does not intensify over time. Lastly, the bottom panel presents humidity and temperature data recorded during resistivity measurements. Initially, external measurements (depicted in black) were obtained from local weather forecasts. In the last six months, internal measurements (in blue) were collected using an Arduino-based sensor during resistivity measurements themselves. While no obvious correlation has been observed between surface resistivity and environmental variables, it is crucial to note that the resistivity data for those plates are available only up to December 2021, as the RPCs were assembled at the beginning of 2022.

4.4.4. Hand-Painted resistive plate: Manual coating

Due to cost constraints and limited access to a serigraphy printer, coupled to the rising surface resistivity issues discussed in 4.4.3, adversely affecting our detector's performance, the forthcoming batch of resistive plates will be developed in-house at CP3 lab. Lessons learned from both the serigraphy and initial hand-painted techniques used in the prototype phase have guided our production strategy. Our aim is to achieve localized production, enabling experimentation with various glass plate thicknesses and surface resistivity ranges. This section offers a detailed overview of the entire production process.

Electrodag 6017SS (% by weight)	Electrodag PM-404 (% by weight)	@ 25μm dry coating thickness
100	0	35
90	10	50
80	20	70
70	30	105
60	40	170
50	50	290
40	60	675
30	70	2160
25	75	4500
20	80	35,000
10	90	> 1e9

Figure 4.27. ❘ Blending ratios of LOCTITE EDAG PM 404 E&C and EDAG 6017SS, Dried 5 minutes @ 120 ° C, Ω / □ [159].

Table 4.3 presents an overview of the instruments employed in this procedure along with their respective properties.

Before initiating our procedure, it's crucial to select the desired resistivity value and the total mixture mass. This allows us to calculate the mass of each component using the mass ratio formula:

Instruments	Properties
Glass plates	From "VERRE INDUSTRIE"
	Size = 20 cm × 20 cm
	Thickness = 0.7, 1.1, 2 mm
Roller	Size = 20 cm
Resistive paint	Conductive ink: LOCTITE Electrodag 6017SS
	Non conductive ink: LOCTITE Electrodag PM 404
Thinner	2-butoxy ethyl acetate (butylglycol acetate)
Mixer	Vacuum mixer known as SmartMix X2
Oven	UF750plus: remotely controllable
Syringe	/
Sponge wand	/

Table 4.3. | Different instruments and material used in the painting process

$$r_c = \frac{m_r}{m_r + m_c} \tag{4.16.}$$

where: r_c represents the mass ratio, m_c is the mass of conductive ink, and m_r is the mass of non-conductive ink. Manufacturers provide reference values for various compositions (refer to Figure 4.27).

Once these parameters are set, clean the glass plate with Ethanol and affix it to the table with tape. Concurrently, prepare the mixture for blending. Once the mixture is ready, the painting procedure involves two steps:

1. **First coat:**
   - Use a syringe to apply the coating on the plate, see Figure 4.28(a)
   - Ensure even distribution of the paint using a sponge wand, specially on the edge (Figure 4.28(b)). This step is vital to achieve uniform plate resistivity after baking.
   - Utilize a roller only once to evenly spread the paint and remove excess. Apply gentle pressure and avoid excessive force to prevent unevenness.
   - After cleaning the table and the roller, place the plate in the oven at 120°C for 5 minutes.

Following baking, the first coat should appear even without any patches, as depicted in Figure 4.28(c). Once the first coat is completed, proceed with the second coat using a different method.

2. **Second coat**:
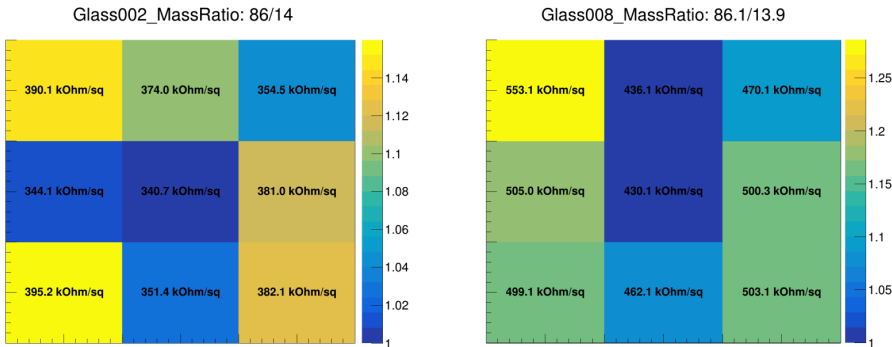   - Place a secondary dry plate next to the initial plate, and apply a few

lines of paint on it, as shown in Figure 4.28(d).

- Use the secondary plate to evenly coat the roller with a thin layer of paint (Figure 4.28(e)).
- Roll the wet roller back and forth in multiple directions to create a uniform second layer (Figure 4.28(f)).
- Illuminate the layer with a flashlight to identify patches or areas where the roller did not coat effectively.
- If necessary, reapply paint on the secondary plate, coat the roller again, and then apply it to the plate to complete the even second coat. Apply sufficient pressure to ensure the roller rolls and coats a thick layer on the surface without gliding. Apply some pressure in this step.
- Place the plate back in the oven at 120°C for 5 minutes.
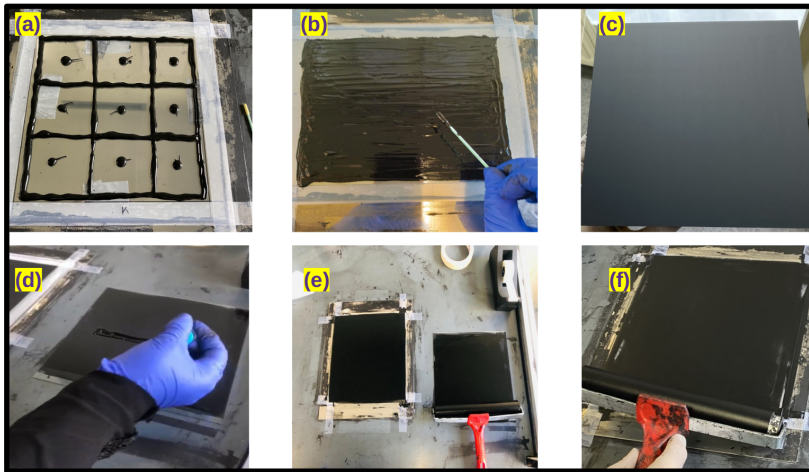
Figure 4.28. | (a) Depositing the first layer. (b) Spreading the paint on the plate using the sponge wand. (c) The plate after banking the first layer. (d) Pipping a couple of lines on a secondary plate. (e) Coating the roller with the secondary plate. (f) Coating the first plate with the wet roller.

Having confidence in our painting technique, we manufactured multiple glass plates with varied mass ratio values, resulting in different surface resistivity values. Measurements were conducted using concentric probes, as depicted in Figure 4.29. For r_c values of 0.860 and 0.861, we obtained resistivity values of 368 $K\Omega/\square$ and 484 $K\Omega/\square$ respectively. These readings exhibited a uniformity level of $\sim 20\%$, which outperformed serigraphy.

Subsequently, we calibrated the mass ratio for the surface resistance of the two components by measuring resistivity for various compositions. Figure 4.30 displays the calibration curve for the mass ratio.

Glass002_MassRatio: 86/14

390.1 kOhm/sq	374.0 kOhm/sq	354.5 kOhm/sq
344.1 kOhm/sq	340.7 kOhm/sq	381.0 kOhm/sq
395.2 kOhm/sq	351.4 kOhm/sq	382.1 kOhm/sq

Glass008_MassRatio: 86.1/13.9

553.1 kOhm/sq	436.1 kOhm/sq	470.1 kOhm/sq
505.0 kOhm/sq	430.1 kOhm/sq	500.3 kOhm/sq
499.1 kOhm/sq	462.1 kOhm/sq	503.1 kOhm/sq

Figure 4.29. | Measurement of surface resistivity of two glace plates at 9 distinct locations, employing two different mass ratios.
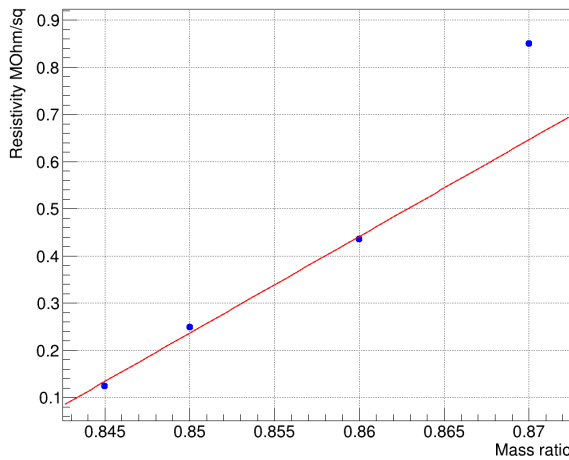

Figure 4.30. | Surface resistivity plotted against mass ratio. Experimental data points are represented by blue dots, and the red line indicates the linear fit, expressed by the equation R = 20.5 .r_c - 17.2.

Following calibration, we placed the produced resistive plate to a controlled environment to study its surface resistivity variation over time, which remained consistent. Figure 4.31 illustrates the stability of the surface resistivity of two plates over 8 months.

4.5. Challenges

Each research endeavor comes with its distinct challenges, offering valuable learning experiences. Our research journey was no exception, marked by
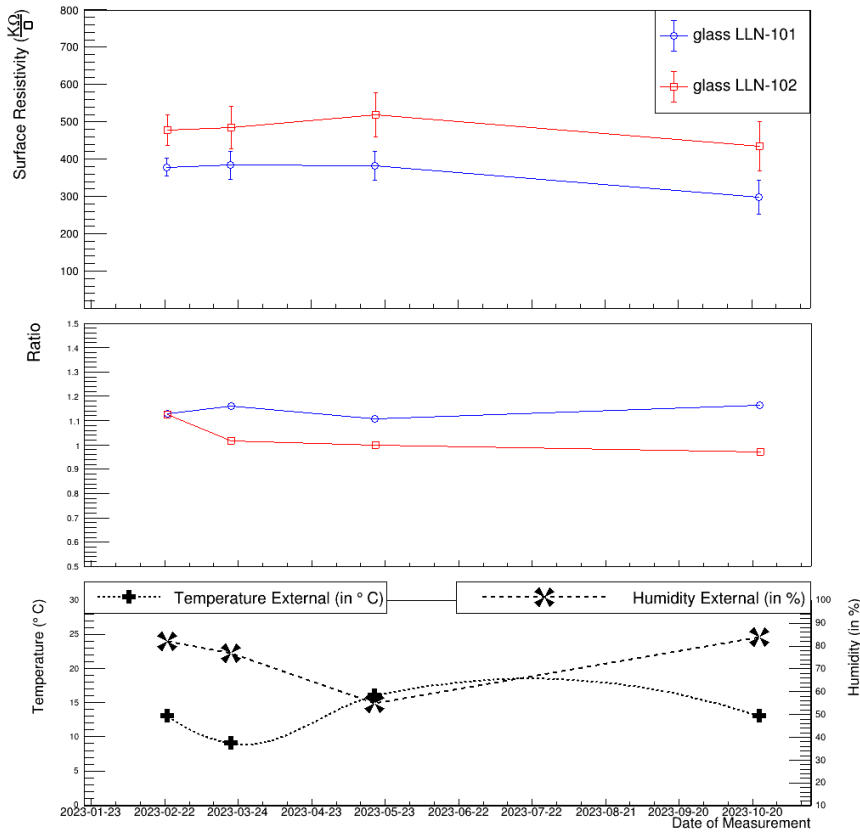
Figure 4.31. ❙ Temporal evolution of key parameters: average surface resistivity of two selected glass plates (top), ratio between the resistivity at the center and the average resistivity of other locations on the same plate (middle), and external measurements of temperature and humidity (bottom).

intricate challenges that required innovative solutions. From refining complex technical setups to addressing noise interference in data, each obstacle provided an opportunity to enhance our methods and deepen our comprehension. This section explores the unique challenges faced in our development, detailing the strategies utilized to overcome these hurdles and improve our results.

4.5.1. Environmental noise

In line with the challenges often encountered in experimental setups, we confronted several issues, with the most prominent one being the substantial presence of background noise. As illustrated in Figures 4.32 and 4.33, this noise exhibited two distinct frequencies, ~144 MHz and ~433 MHz, suggesting a high-frequency source possibly emanating from nearby FM radio or VHF

television transmissions. Our observations indicated that the noise had a high amplitude level, resulting a low signal-to-noise ratio. Consequently, our data acquisition system (DAQ) interpreted this noise as a signal.
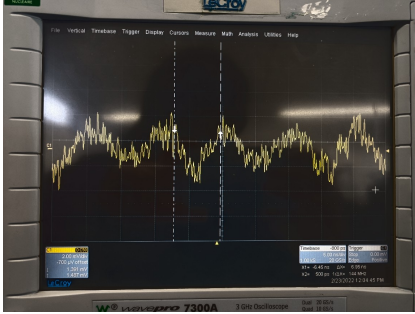

Figure 4.32. | Oscillogram displaying a noise signal at a frequency around 144 MHz.
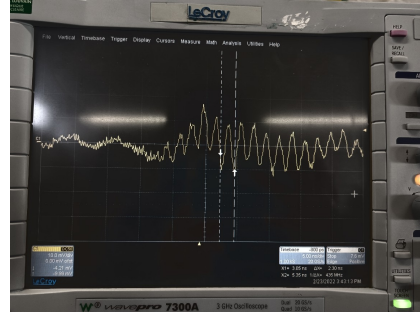
Figure 4.33. | Oscillogram displaying a noise signal at a frequency around 433 MHz.

To identify the origin of this noise, we utilized an ANRITSU MS2713E spectrum analyzer [160], which we borrowed from the electronic engineering department at UCLouvain. This portable device, equipped with a 3-D antenna, allowed us to measure signal strength as a function of frequency.
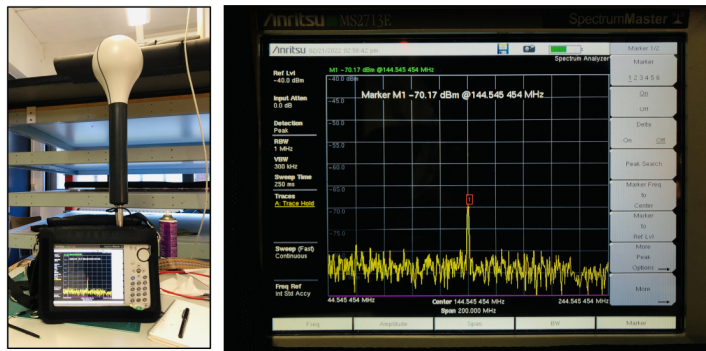
Figure 4.34. | Left: ANRITSU MS2713E spectrum analyzer [160]. Right: The screenshot of the spectrum analyzer screen in the RPC lab, displaying a signal at the frequency of 144.5 MHz.

Systematically moving around the university building, we assessed the signal strength of the 144.5 MHz signal on the ground floor of the "Marc de Hemptinne" building and at each level of Tower E. Interestingly, the signal disappeared within the tower. Further investigation revealed the installation of a new radio beacon on the rooftop of Tower E by the Royal Belgian Amateur Radio

At present, 7 frequencies are active and reported on www.beaconspot.uk

144.418 MHz (CW)   20W into a Big Wheel antenna
432.450 MHz (FSK)   20W into a Big Wheel antenna

Figure 4.35. Beacon active frequencies

Association since late 2019 [161]. This discovery clarified the signal's absence in Tower E (located beneath the antenna) and its presence in our lab. Upon informing the UCLouvain project mediator, we confirmed that these two frequencies were active antenna frequencies (refer to Figure 4.35). Consequently, the transmitters for the 144.41 MHz and 432.45 MHz signals were promptly deactivated.

4.5.2. Reflections and Impedance mismatching

After resolving the issue with antenna noise, a new problem arose: signal reflection, impacting data readings. The initial step involved replacing the deteriorated Version 1 board of the first prototype with a handmade Version 2. due to copper strip degradation over time. Assembling the chamber and filling it with gas revealed significant ringing in the signal, indicating substantial reflection, as shown in Figure 4.36.(a).

To address this, we experimented with two termination values to find the optimal one. Initially, we soldered a 50Ω resistor (2 parallel 100Ω) to each strip of board Version 2 which became Version 2.1, which reduced the reflection amplitude but didn't eliminate it entirely, as depicted in Figure 4.36.(b). Continuing our efforts, we changed the termination to 100Ω and developed board Version 2.2. This modification resulted in a clean signal, demonstrated in Figure 4.36.(c).

Consequently, we opted for a 110Ω termination. This decision influenced the design of printed readout Version 4. Additionally, we took care to maximize the distance between copper tracks from strips to connectors to minimize cross-talk between tracks, as illustrated in Figure 4.37.

4.5.3. Study the performance of RPC using NIM modules

A significant effort was invested in evaluating RPC performance using a NIM crate without utilizing the DAQ system due to the presence of 34-pin male connectors on our boards. To facilitate this study, a new version of the readout board was designed, enabling the RPC performance assessment with external NIM crate modules.

This readout board incorporated coaxial cables directly connected to the readout strips (see Figure 4.38.(a)). A specialized component was created to seal the chamber, allowing 16 coaxial cables to exit the aluminum chamber (Figure
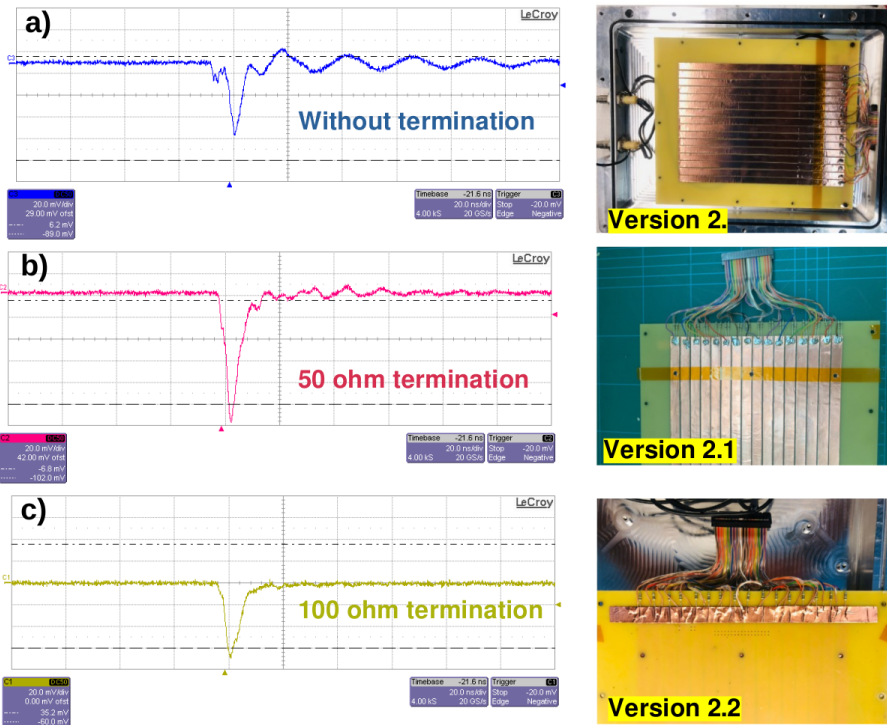
Figure 4.36. ┃ RPC signal observed from each readout board with a 7.2KV applied high voltage
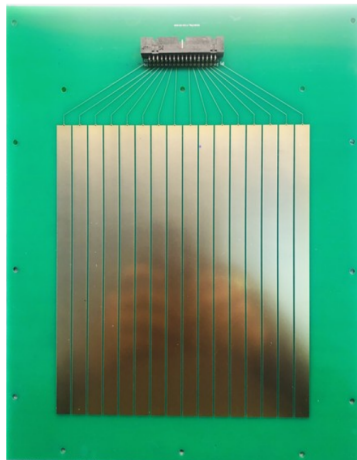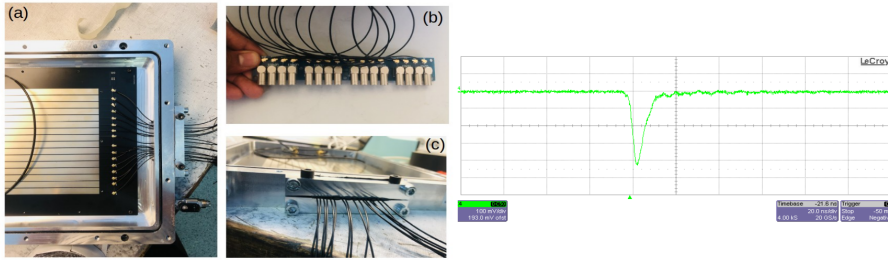

Figure 4.37. ┃ Printed readout board with better quality copper and connection compatible with the DAQ with 110Ω termination

Figure 4.38. ❙ Left: (a) Readout board inside the Chamber. (b) Board with 50 Ω NIM standard female connectors. (c) New sealing "piece" for RPC. Right: RPC observed signal with HV=-7.2KV

4.38.(b)). These cables were then connected to a board with 16 NIM outputs (Figure 4.38.(c)). Due to the small size of the coaxial cable, a direct connection to standard 50Ω NIM connectors was not possible. Consequently, the coaxial cables were linked to external boards equipped with standard NIM female connectors. The obtained signal from this board is depicted in Figure 4.38 (Right).
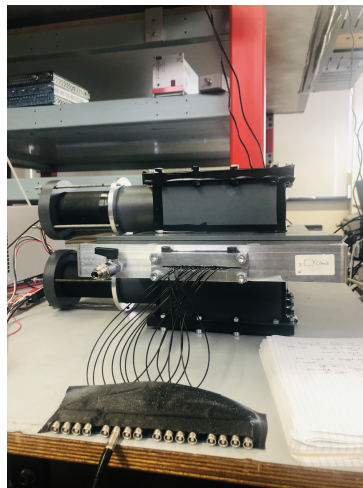
Figure 4.39. ❙ RPC configuration setup.

Upon confirming the signal adequacy, efficiency measurements for one of our RPC chambers (Figure 4.39) were conducted using the setup illustrated in Figure 4.40.(a). The NIM modules employed in this study included:

- 3 Lecroy Model 623B Octal discriminators (utilizing 18 discriminators).
- 1 Lecroy Model 429A Logic fan-in/fan-out unit.
- 1 Lecroy Model 622 Quad coincidence module.
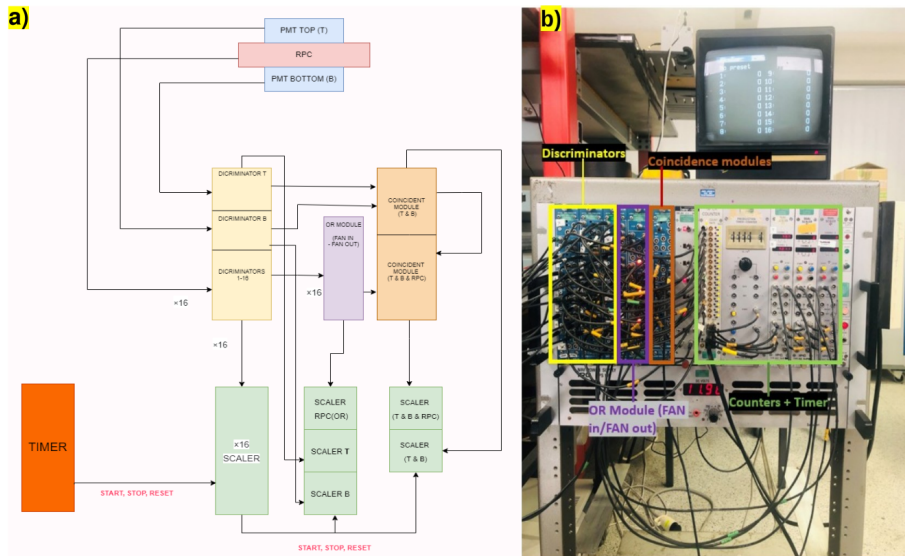
Figure 4.40. ┃ (a) Sketch for the setup. (b) NIM crate setup

- 1 Borer delay module.
- 16-channel counter.
- IPC pre-selection timer counter.
- 3 dual scalers.

This setup allowed for the counting of individual hits from each RPC strip, two PMT counts, coincidences between two scintillators, and OR operations of the 16 strips. All 16 RPC strips were connected to separate discriminators (channels 1–16). The discriminator threshold was set to -100 mV (-1 V as measured using a multimeter), and the output signal was digitized with a width of 20 ns.

The discriminator outputs were divided into three paths: one connected to the 16-channel counter, another to the Lecroy Model 429A Logic fan-in/fan-out unit, which performed the OR operation of the 16 strips. The output of this unit was linked to the delay module, with a delay set at 35 ns.

The PMTs (labeled A and B) were connected to two discriminator modules with a threshold of -400 mV and an output signal of 20 ns in width. One output from each discriminator (A, B) was connected to a channel of the dual scaler, and the other to the coincidence module (A & B). The output from (A & B) went to a counter and another coincidence unit (A & B & RPC), where the delayed signal of the OR operation of the 16 strips served as the other input. The output of A & B & RPC was connected to a single channel of the dual scaler.

The IPC pre-selection timer counter controlled the counters, providing signals for starting, stopping, and resetting them (see Figure 4.40.(b)). Readings from

all five scalers were recorded for 600 seconds at various high voltage values, ranging from 2400 to 3900 DAQ units. The chamber efficiency was calculated using the formula:

$$Efficiency_{RPC}(\epsilon) = \frac{A \,\&B \,\& \, RPC}{A \,\& \, B} \qquad (4.17.)$$

4.5.4. Study the performance of RPC using DAQ

To evaluate the performance of our RPC chamber with the DAQ system prior to the integration of an external trigger (as discussed in Section 4), we directly connected the PMT signal to the CMS FEB using two LEMO to twisted-pair female connectors.

Upon reviewing the data, we identified a noise issue captured by our DAQ system, which proved to be quite troublesome. This noise was evident in our timestamp data, manifesting as a recurring peak of events that shared the same timestamp and affected all strips. Even attempts to apply coincidence criteria between chambers and PMTs did not eliminate this noise.

To address this problem, we developed an offline macro, which served to clean the original data file. This entailed setting a threshold to filter out these noisy events based on an acceptable maximum frequency. Subsequently, a new cleaner dataset was created, aligning with this condition, and it could be used in our subsequent analyses. Figure 4.41 provides an illustration of the time
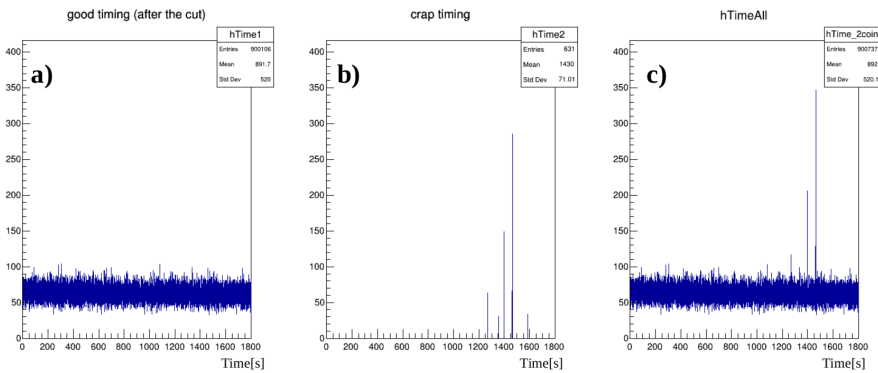
Figure 4.41. ┃ (a) Time stamp distribution after placing the cut (new dataset). (b) Crap timing distribution. (c) Time distribution before cut.

distribution before and after this filtering process, highlighting the removal of undesirable noise-related data.

However, it's worth noting that our efforts in this direction were suspended when we successfully implemented the external trigger using the two bits from

the time buffer. A different strategy, which I will elaborate on in the upcoming section (section 4.6.5), was subsequently developed.

4.6. Performance studies

In this section, our focus centers on two key parameters. First, multiplicity, which signifies the total number of strips activated in a single event, ranging from 1 to 16 in our detectors. Second, occupancy, representing how frequently each strip is activated across the entire dataset, providing insights into the behavior of individual strips. Additionally, we delve into the efficiency of the RPC chamber using eq 4.17, employing both DAQ and NIM modules.

4.6.1. RPCs with different board readout

The three RPCs were set up according to the configuration illustrated in Figure 4.42. Online coincidences were established at two, and the RPCs were powered internally at -6.6 kV. Data collection spanned 12 hours, initially in our RPC lab and later in the CMS clean room, functioning as a shielding Faraday cage.

RPC with Readout v2.1 (with 50 Ohm resistor)

RPC with Readout v3.0

RPC with Readout v1.0
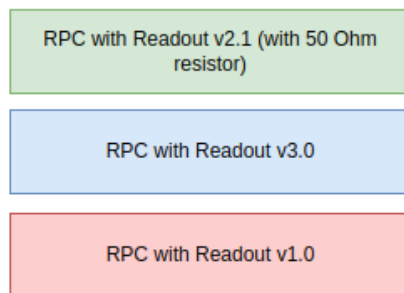
Figure 4.42. ❘ Sketch of arrangement of RPCs with different readout boards.

To ensure data accuracy, a timing cut described in subsection 4.5.4 was applied to the RPC lab data, eliminating recurrent noise at specific timestamps. Upon comparing multiplicity and occupancy data between the two labs, accounting for an offline coincidence of three chambers in our analysis code, we noticed higher counts in the RPC lab due to a higher noise rate compared to the CMS clean room.

The three RPCs exhibited diverse behaviors, with all chambers displaying a multiplicity exceeding three. The chamber utilizing readout version 3.0 showed the poorest performance, likely due to impedance mismatching, whereas readout version 2.1 demonstrated the best performance. In the occupancy plot, it became apparent that corner strips exhibited higher firing rates than

Multiplicity distribution   Occupancy distribution (log)
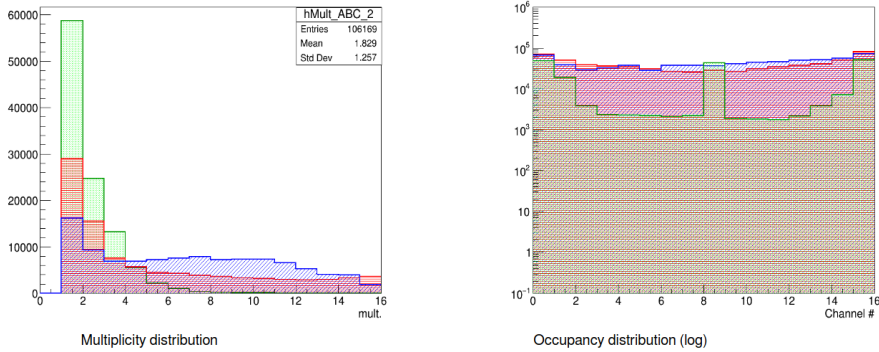
Figure 4.43. | The multiplicity and occupancy distributions of three distinct RPCs were examined in the RPC lab. The green plot corresponds to readout version 2.1 (refer to section 4.5.2), the blue plot corresponds to the RPC with readout board version 3.0 (refer to section 4.5.3), and the red plot represents the chamber with readout board Version 1.0 (refer to section 4.2).

Multiplicity distribution   Occupancy distribution (log)
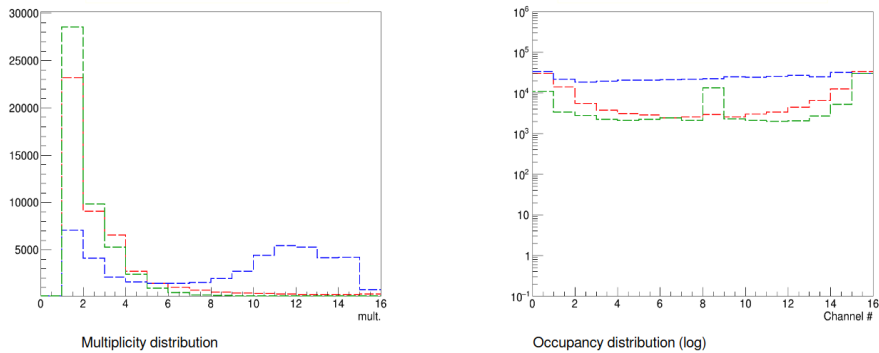
Figure 4.44. | The multiplicity and occupancy distributions of three distinct RPCs were examined in the CMS clean room. The green plot corresponds to readout version 2.1 (refer to section 4.5.2), the blue plot corresponds to the RPC with readout board version 3.0 (refer to section 4.5.3), and the red plot represents the chamber with readout board Version 1.0 (refer to section 4.2).

middle strips, an undesirable occurrence. Further investigation revealed a faulty resistor soldering on the 8th strip in the readout version 2.1, explaining the elevated counts resulting from noise caused by the loose connection.

4.6.2. PMTs to CMS FEB

After evaluating the behavior of each RPC using the self-trigger method, it becomes crucial to assess its response to an external scintillator trigger. As mentioned earlier in section 4.5.4, we initially directed the PMT signal directly to the CMS board before implementing the procedure detailed in section 4.3.5. Consequently, we connected the PMT signal to channels A and D of the DAQ, where the signal needed to be discriminated. To determine the optimal threshold for the two PMT signals, we conducted a threshold scan for 2 minutes at each threshold value.
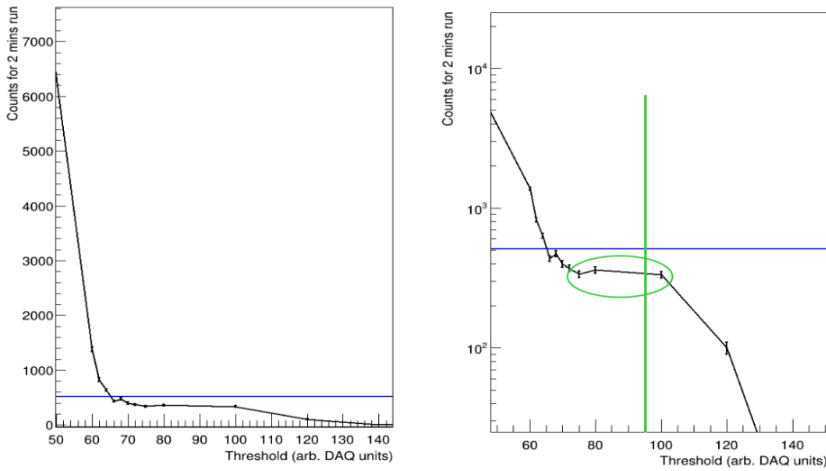
Figure 4.45. | The number of coincidences in the PMT as a function of the threshold. The left panel displays the count axis in linear scale, while the right panel depicts it in logarithmic scale for enhanced visibility of the plateau.

The scan results, illustrated in Figure 4.45, where the roughly expected number of events in 2 minutes was 512, represented by the horizontal blue line. We chose a threshold of 95 DAQ units (depicted by the vertical green line) as the PMT's threshold.

However, integrating the external trigger setup into the existing DAQ, originally designed for RPCs alone, demanded adjustments to the program for both PMTs and RPCs. After several iterations, new timing parameters were introduced into the system.

$$CoinWindow\,[ns] \;=\; (CoinValue\,[DAQ\,units] \;+\; 2) \;\times\; 5\,ns \qquad (4.18.)$$

Individual delay adjustments for channels A, B, C, and D were implemented, along with the configuration of the coincidence window (following eq. 4.18)
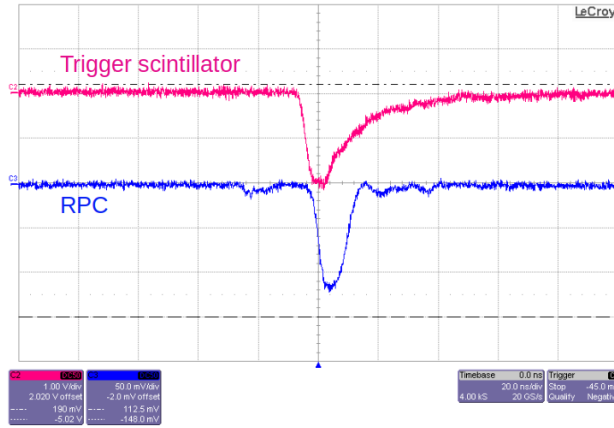
Figure 4.46. ❘ The coincidence of signals between a single strip of the RPC and the scintillator, with a 50 ns delay introduced in the RPC signal using cables and a delay module.
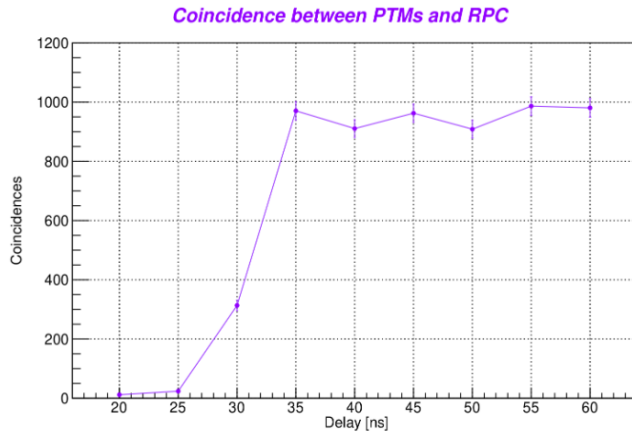
Figure 4.47. ❘ Count of coincidences at various RPC signal delay values.

among all detectors. These parameters can be fine-tuned using both the shell script or GUIs. Considering the faster propagation of RPC signals compared to PMT signals (see Figure 4.46), a delay scan was performed within the DAQ to determine the correct value. For this, an RPC chamber was placed between two scintillators, operating at -6.6kV with a 50 DAQ units threshold and a 20ns coincidence window. Subsequently, a scan of delays ranging from 3 to 15 DAQ time units (where one time unit equals 5 ns, corresponding to the FPGA clock frequency) was conducted, with 10 minutes allotted for each point.

Data were collected for various delay values, and the coincidences counts between PMTs and RPCs are shown in Figure 4.47. Based on this plot, a delay value of 35 ns appeared optimal for the data collection process. However, despite the scan indicating 35 ns as the suitable delay, an additional 1 m extension of the signal cable was necessary for the RPC setup. Consequently, a 30 ns delay, equivalent to 6 DAQ delay units, was utilized in the DAQ. With a functional external trigger established, we proceeded with the efficiency calculation of the RPC using the DAQ system, replacing the previous method utilizing external NIM electronics and enabling us to assess RPC quality with multiplicity data, a capability we previously lacked.

4.6.3. High voltage and threshold scan

After adjusting the parameters of the PMT in the DAQ, we conducted a high voltage scan for various RPC chambers equipped with different readout boards. A comparison was made between chambers with readout version 1.0 and version 3.0, utilizing DAQ and external electronic data collection via board version 3.0, following the setup described in section 4.5.3. In this scan, an
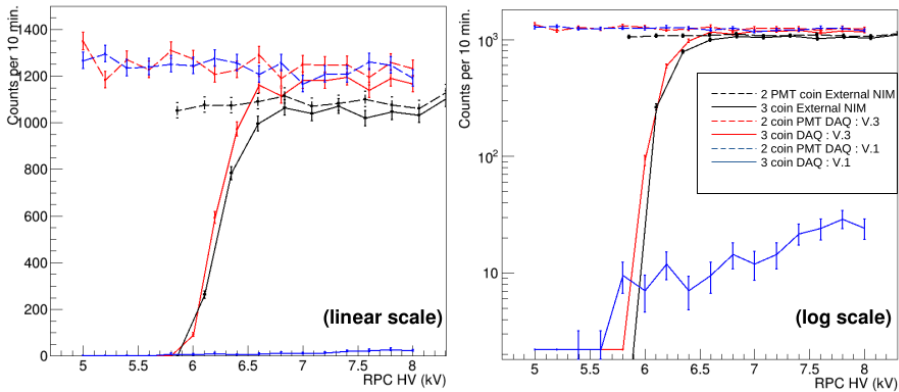
Figure 4.48. ❘ Comparison of the performance of RPCs (readout version 1.0 in blue and version 3.0 in red) and PMTs with respect to the supplied high voltage using both external NIM electronics and DAQ. The data on the left are presented in linear scale, while the ones on the right are in logarithmic scale.

internal negative high voltage supply was employed using DAQ to modulate the high voltage (the conversion factor used is represented in eq. 4.19), with RPC thresholds set to 50 DAQ units.

$$V_{out}[volt] = \frac{V_{in}[DAQ\ unit]}{4095} \times 10000 \qquad (4.19.)$$

Each data point was collected over 10 minutes, and online coincidence was set

to two. However, during data analysis, three coincidences were considered to account for RPC behavior.
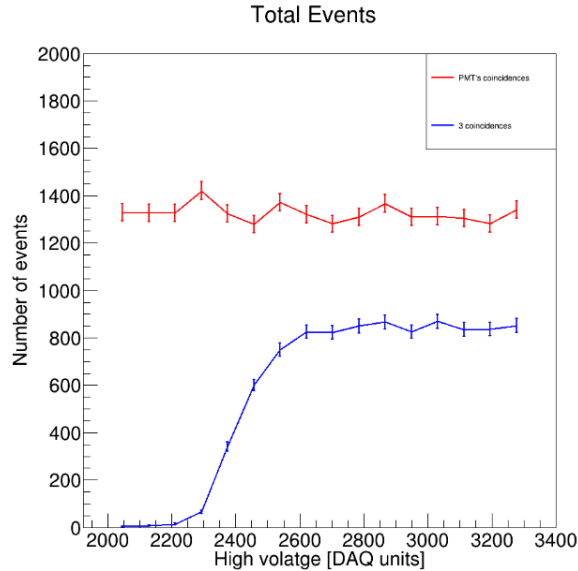
Figure 4.49. ❙ Performance of RPCs (readout version 2.2, indicated in blue) and PMTs (shown in red) with supplied high voltage.
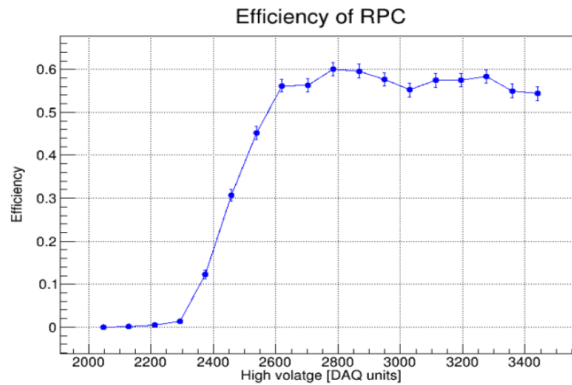
Figure 4.50. ❙ Variation in efficiency of the RPC (readout version 2.2) with high voltage.

Figure 4.48 illustrates the comparison of 2 PMT coincidences using both NIM and DAQ for the two boards. As expected, the results were nearly identical (dash lines) and the PMT coincidence count wasn't affected by the high voltage as it was powered by a fixed external power supply. Notably, the coincidence
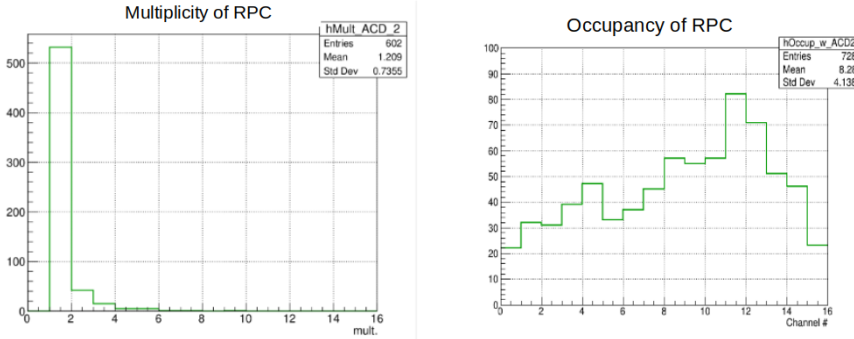
Figure 4.51. ❘ Occupancy and multiplicity plots at -8 kV of high voltage.

count for the chamber containing board version 1.0 (continuous blue line) was significantly low, indicating the need for its replacement. This was not the case for board version 3.0 (continuous red line), but unfortunately, it exhibited poor multiplicity, as observed in Figures 4.44 and 4.43.

Our focus shifted to board version 2.2, and under the same conditions, the scan results was depicted in Figure 4.49. The efficiency of this RPC, calculated using eq. 4.17, showed variations based on high voltage supplies, as represented in Figure 4.50. With this conditions, an efficiency of up to 60% was achieved. Multiplicity and occupancy plots for -8 kV (~ 3277 DAQ units) are presented in Figure 4.51.
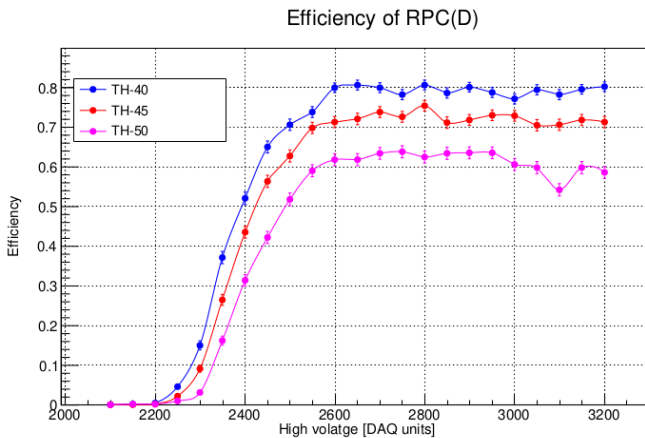
Figure 4.52. ❘ High voltage scan for RPC (readout Version 2.2) at varying threshold values.

In the multiplicity plot, over 80% of hits were single hits per strip, with more than 90% limited to 2 hits per strip. The occupancy plot revealed that hits were

concentrated in the middle of the RPC, with fewer hits observed in the corner strips, aligning with the expected RPC behavior.

Subsequently, the same scan was conducted using lower threshold values for RPC: 45 and 40, resulting in an efficiency of 80% with a threshold of 40, as illustrated in Figure 4.52.

4.6.4. Joint Data taking with UGent Detector

In parallel with our prototype, UGent University is developing another RPC prototype with slightly different characteristics. These prototypes are currently undergoing cross-validation as part of our preparations for jointly developed muography detectors in the future. A collaborative effort between UCLouvain and UGent in the field of muography research has been established. With this collaborative setup, we conducted a joint data collection campaign at the University of Ghent to assess and cross-validate the performance of the two RPC prototypes, despite their minor differences. The main distinctions between Prototype 1.L (UCLouvain) and Prototype 1.G (UGent) are outlined in Table 4.4.

Property	Prototype 1.G	Prototype 1.L
Active area	$28 \times 28 \ cm^2$	$16 \times 16 \ cm^2$
Gas Flow	Continuous	Sealed
Glass thickness	$1.3 \ mm$	$1.1 \ mm$
Strip Width	$15 \ mm$	$9 \ mm$
Strip Pitch	$16.6 \ mm$	$10 \ mm$
Semi-resistive coating	Hand-sprayer ($\sim 450 \ K\Omega/\square$)	Serigraphy ($\sim 4 \ M\Omega/\square$)
DAQ	NIM + CAEN integrated	Custom made
Portability	Not yet	Portable

Table 4.4. ‖ Main differences between the two RPC prototypes developed so far [162].

During the joint data collection, both prototypes were integrated into the DAQ system of Prototype 1.L. The operating parameters were set to our initial estimates, including a high voltage (HV) of 7 kV and a threshold discriminator value of 90 DAQ units. Figure 4.53 provides an overview of the occupancy (indicating the number of times each strip fired throughout the run) and the multiplicity (representing the total number of strips fired per event). It is essential to note that although both detectors consist of 16 strips, the plots showcase results from the last 8 strips, as the first 4-5 strips of Prototype 1.G were affected by hardware issues, which were resolved after this data collection.
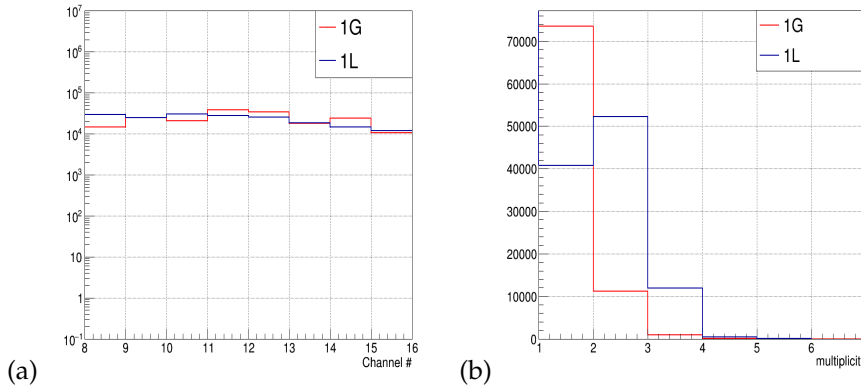
Figure 4.53. (a) Distribution of occupancy for prototype 1.L (depicted in blue) and prototype 1.G (represented in red). (b) Distribution of multiplicity for both prototypes 1.L and 1.G. [162]

In Figure 4.53, both distributions are normalized to the active area of 1.L. The occupancy distributions of both prototypes show general agreement, signifying similar behavior and functionality. Consequently, we can affirm that the two detectors exhibit consistent behavior, validating each other's performance. However, a notable distinction appears in the multiplicity distribution, which is higher in Prototype 1.L. This variance could be attributed to differences in the resistivity of the glass plates; specifically, Prototype 1.G has lower resistivity compared to 1.L. Moreover, the difference in the gap between strips influences the cross talk among them, as Prototype 1.G has a larger gap between strips (1.6 mm) compared to Prototype 1.L (1 mm).

4.6.5. PMTs to the FPGA

The process of linking the external trigger directly to the FPGA on the main board of the DAQ is described in section 4.3.5. After finalizing the trigger electronics, the DAQ was reprogrammed to integrate the trigger system. To address reflections observed from the FPGA output, LVDS termination within the FPGA was enabled, and a 2.5 V power supply was integrated into the FPGA board. In the muoscope DAQ setup, specific FPGA pins were connected to the LEMO output cable, enabling signal monitoring if needed.

Through a series of iterations, the decision was made to employ two PMT coincidences as triggers, capturing 250 consecutive data samples after each trigger. Each sample had a duration of 5 ns. Additionally, the RPC signal was intentionally delayed by 670 ns. This configuration facilitated the examination of readout strip behavior, both before the avalanche signal (representing noise) and after the signal (representing tail behavior). The timing distribution of
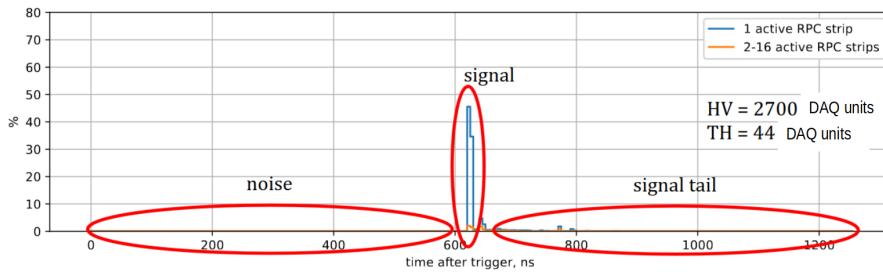
Figure 4.54. | Noise, signal and signal tail of the RPC. The Y-axis denotes the efficiency with respect to the PMT trigger.
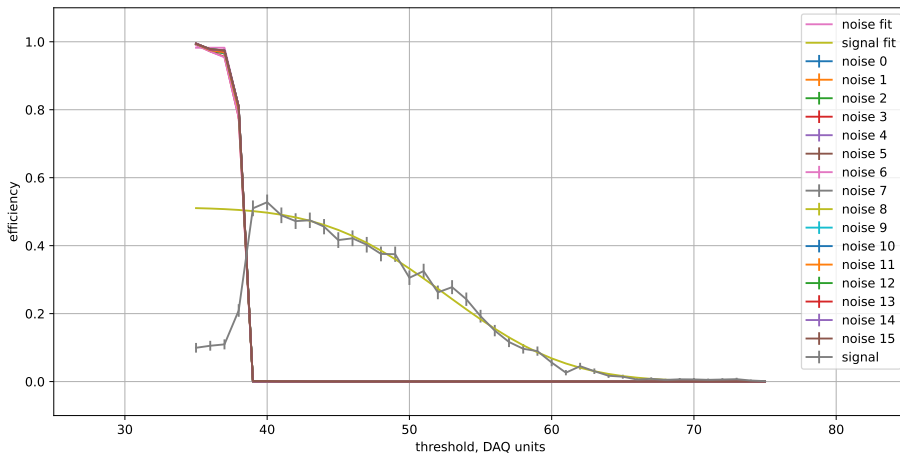
Figure 4.55. | Threshold scan for signal and noise in the RPC, the high voltage supplied for the RPC is -5.8 kV.

the updated DAQ program is visualized in Figure 4.54.This new approach allowed us to assess the noise in each strip and determine the optimal threshold value for noise cutoff. Figure 4.55 demonstrates the noise and signal variations concerning the threshold for the RPC assembled with the readout board version 2.2. For thresholds below 40 DAQ units, every strip fired with 100% efficiency. Beyond 40 units, the noise level dropped almost to zero, and the signal efficiency became evident. This plot corresponds to -5.8 kV (2400 DAQ units), which is below the average working high voltage (see Figure 4.52).

4.6.6. Performance of RPC with board version 4.0

After adopting readout version 4.0 (Figure 4.37) as our optimal configuration and implementing a new timing filter with a fixed 10 ns muon time window for event selection to reduce false coincidences, the performance of the RPC was

evaluated, as depicted in Figure 4.56. In Figure 4.56 (a) and the subsequent one (b), the occupancy and multiplicity distributions are presented, respectively. These analyses were carried out at four different threshold values in DAQ units, maintaining an HV of -7 kV. The third plot illustrates efficiency variations concerning thresholds at three distinct working points (-6.6, -6.8, and -7 kV). As expected, both occupancy and multiplicity decrease with higher threshold
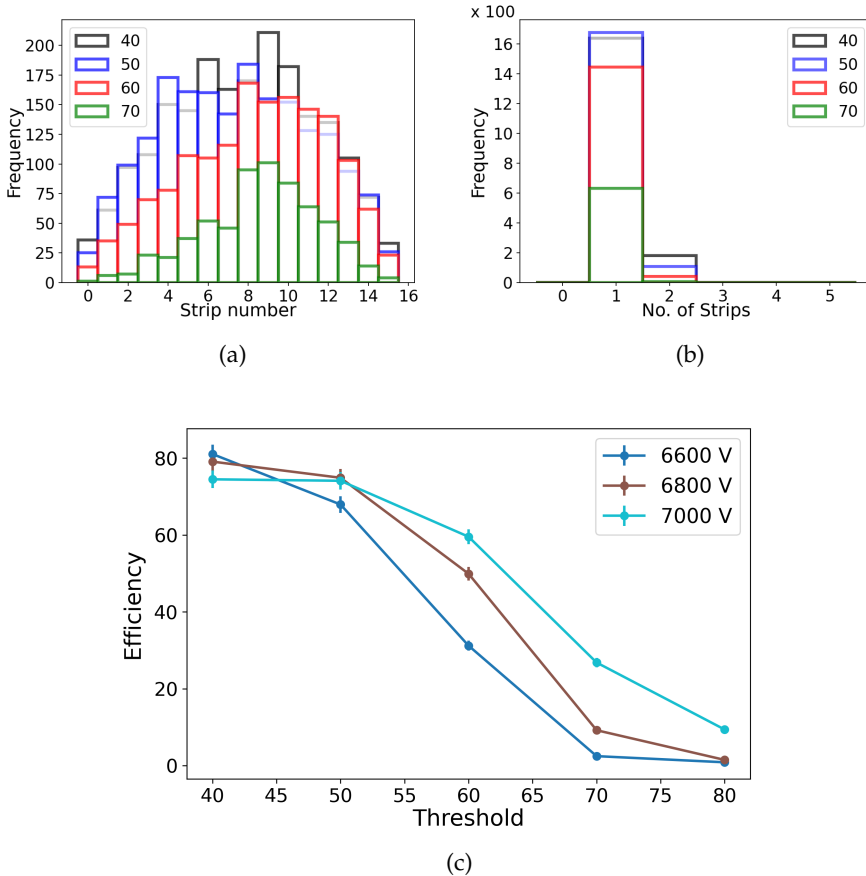
Figure 4.56. ❙ The obtained measurements illustrate (a) occupancy and (b) multiplicity, conducted at an HV of -7 kV with varying threshold values (in DAQ units); (c) illustrates the efficiency variations with respect to thresholds at three distinct working points.

values. Higher thresholds effectively reduce background hits; however, excessively high settings might exclude potentially valuable events. To determine the optimal DAQ threshold, the study focused on efficiency concerning thresholds. The results indicated that efficiency remains relatively stable up to 55 DAQ units for all three working points. Beyond this threshold, efficiency experiences a

noticeable decline. Therefore, for subsequent investigations, the threshold was fine-tuned within the range of 40 to 45 DAQ units to strike a balance between noise reduction and event retention.

4.6.7. RPC I-V characteristic

To comprehend the operating characteristics of RPCs, an equivalent circuit is commonly used to illustrate the current behavior under stable conditions concerning the operating voltage, as demonstrated in Figure 4.57 (a). In this circuit, the diode mimics the gas's role. At low voltages, the diode is "off", mirroring the gas's insulating behavior. As the voltage increases, the diode switches "on", symbolizing the initiation of the avalanche process. This complexity highlights the various factors influencing the measured current, including gas composition, operational mode (avalanche or streamer), and environmental parameters such as temperature and pressure. Determining

| (a) | (b) |
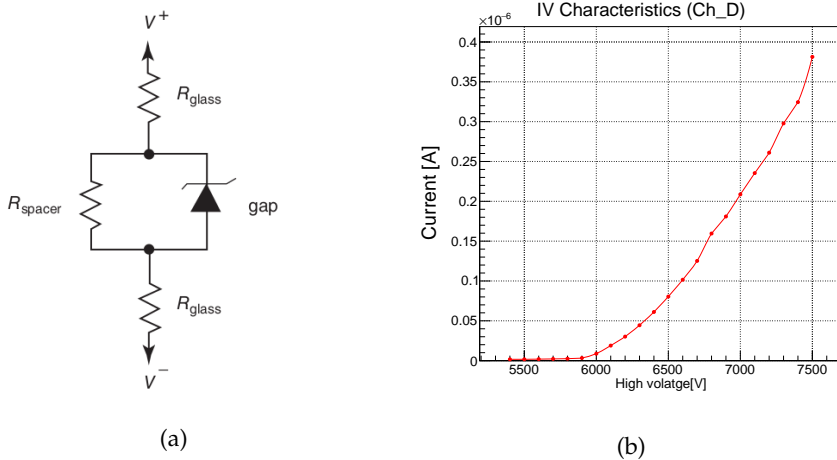
Figure 4.57. │ (a) Electrical circuit equivalent to an gRPC. At low voltage levels, the gas multiplication processes are negligible, resulting in a high gas resistance ($R_{gap} \sim \infty$) and a voltage-current relationship $dV/dI = 2R_{glass} + R_{spacer}$. Conversely, at high voltage levels, the gas resistance $R_{gap} \sim 0$ leading to a $dV/dI = 2R_{glass}$ (b) Ohmic behavior of one of our gRPC.

the optimal operating high voltage (HV) for the avalanche mode in our RPC involved measuring the current drawn by the detector across a range of HV values, as shown in Figure 4.57 (b). The current behavior, particularly in avalanche mode, exhibits a linear correlation with HV, indicating the Ohmic behavior of the detector. This linear pattern was observed within the 6.2 kV to 7 kV range, identifying suitable operational points. However, due to the wide HV span, precise fine-tuning was imperative to optimize the RPC's performance.

4.7. Garfield++

GEANT4 alone does not provide a comprehensive understanding of inter-actions in gas detectors, particularly in avalanche and streamer modes, and the subsequent signal formation. In this context, utilizing Garfield++ [103] proves valuable. When simulating a gaseous detector, the first step involves determining the ionization deposited in the gas by the incident particle. To achieve this, we employ the HEED [163] simulation software. Initially, a gas file containing the CMS gas mixture is generated using Magboltz [164,165] to model the primary ionization resulting from the passage of a charged particle through the detector.
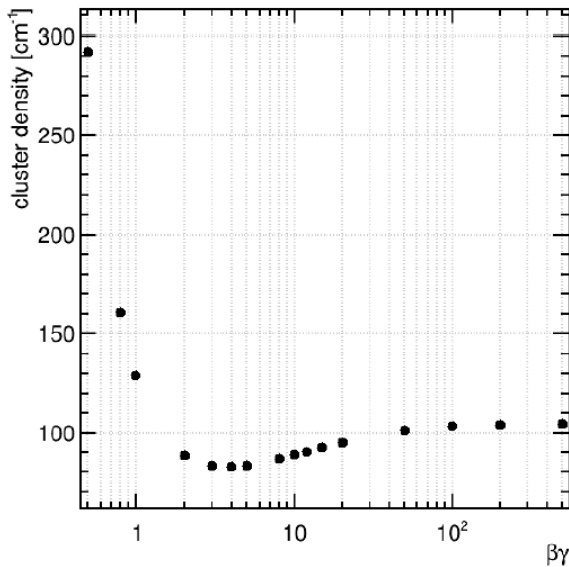
Figure 4.58. | Average clusters per cm as calculated by Heed++ for CMS gas mixture at 20° and 1.1 atm.

4.7.1. Muons Interaction

As a charged particle travels through the gas, it induces ionization along its path. Each ionization event results in the production of electron clusters, which can contain varying numbers of electrons depending on the energy lost by the particle during the interaction. The quantity of primary ionization deposited in the detector is characterized by the cluster density—indicating the number of clusters produced per unit length—and the probability distribution of the number of electrons per cluster. Figure 4.58 illustrates the cluster density for CMS gas mixture generated by incident muons. As expected, this curve exhibit behavior consistent with the energy loss predicted by the Bethe formula. On
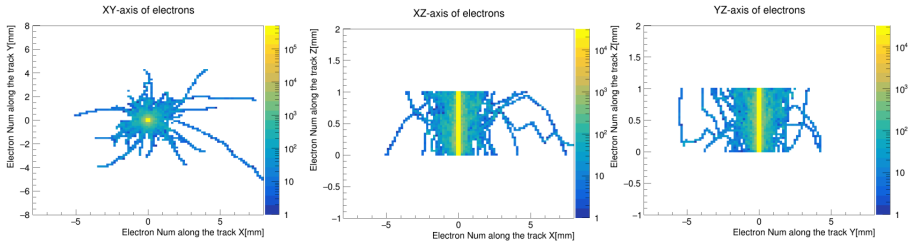
Figure 4.59. | Electron trajectory within the gas gap from different view.

average, a minimum ionizing muon in commonly used RPC mixtures produces 75 clusters per centimeter.
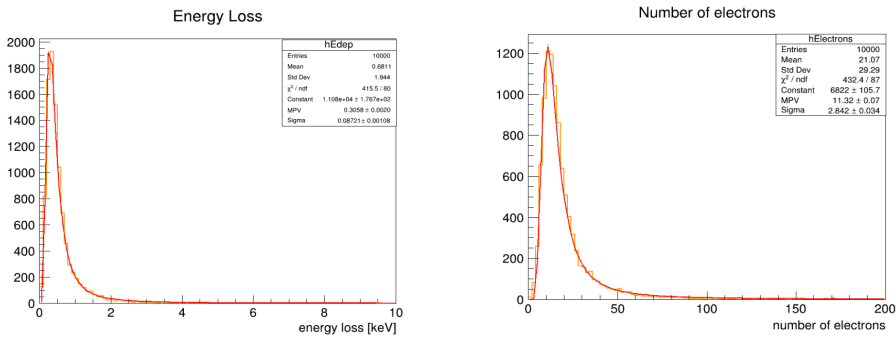
Figure 4.60. | Energy loss (left) and number of electron (right) caused by muon interaction within a 1mm thick gas.

Additionally, Figure 4.59 illustrates the trajectory of electrons in the 1 mm thick gas due to the interaction of 100,000 muons with an energy of 2 GeV, while Figure 4.60 shows the deposited energy with an average of ∼ 305 eV and a number of electrons around 11.32.

4.7.2. Electron Amplification and Attachment

As each liberated electron resulting from the passage of a charged particle traverses the gas medium, it drifts under the influence of the electric field. During this journey, the electron undergoes multiplication through interactions with gas molecules, giving rise to an electronic avalanche that progressively extends until it reaches the anode of the RPC.

For each individual electron, there exists a probability of undergoing multiplication and another probability of becoming attached to a gas molecule. Assuming that the ionization probability remains independent of previous collision histories, we can characterize the avalanche by utilizing the Townsend coefficient (representing the mean free path for ionization) and the attachment

coefficient (represents the probability of a neighboring molecule attaching and absorbing an ionized electron) . These coefficients capture the electron's behavior in terms of multiplication and attachment probabilities.
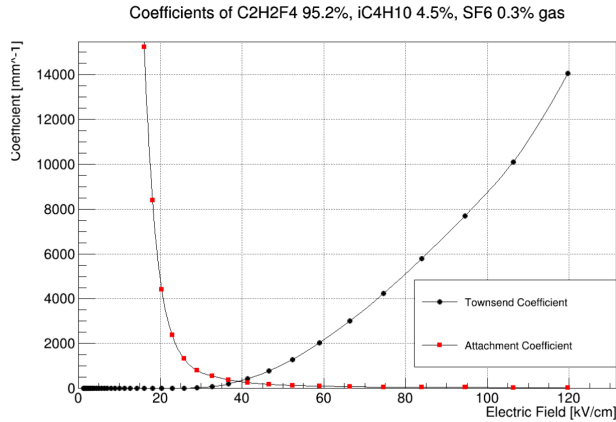
Figure 4.61. | Townsend and Attachment Coefficients for the CMS gas.

Figure 4.61 represents the viable regions that the gas would work in most optimally to produce an electron avalanche. One requires a minimum of 50 kV/cm to be able to produce a noticeable ionization avalanche. Below the electric fields of 40 kV/cm, the attachment abilities of the gas is too high and the ionization capacity is too low.

4.7.3. Drift Velocity

When a constant electric field is applied to the gas, the electron cloud experiences a consistent drifting motion alongside thermal diffusion. In the absence of a magnetic field, as is typically the case in RPCs, the motion aligns with the electric field lines. From a microscopic perspective, an electron, influenced by the electric field, moves and collides with gas molecules. Between collisions, the electron drifts a distance δz, gaining kinetic energy $T = e_0|E|\delta z$, where e_0 represents the electron charge, $|E|$ denotes the electric field intensity, and δz is the distance covered.

After each collision, the electron loses energy and slows down. Subsequently, it gains energy until the next collision, repeating this process continuously. On a macroscopic scale, observers perceive the electron moving at a constant velocity, denoted as v_D. This velocity is an average over numerous collisions and depends on the ratio E/p, where E is the electric field strength and p signifies the gas pressure. This parameter is essential for describing RPC characteristics. Given that our detector is sealed and requires a slight overpressure to prevent
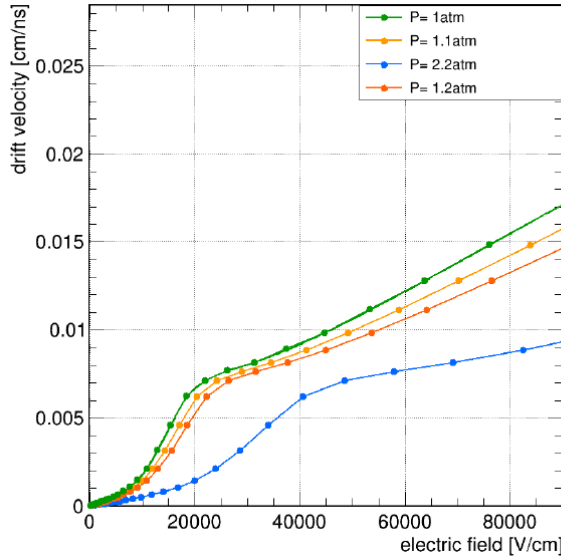
Figure 4.62. | Electron drift velocity in CMS gas mixtures for different pressure values. The temperature of the gas is T = 20°.

any leaks, Figure 4.62 illustrates the variation in drift velocity within RPC gas mixtures under different pressures, emphasizing the importance of maintaining the detector pressure within the range of 1.1 - 1.2 atm.

4.7.4. Signal Simulation and Environmental Influences

In simulating the signal using Garfield++, the process initiates with the meticulous definition of the RPC setup through the "ComponentParallelPlate" parameter. Subsequent steps involve specifying the readout structure, creating the sensor, and defining the necessary time window for signal plotting. The gas mixture and its geometry are then specified, and grid-based avalanche calculations are conducted. After configuring all the essential avalanche parameters, specific events are generated, including momentum and ID, leading to the computation of the signal within the sensor object. In Figure 4.63, the simulation results depict the Signal and Avalanche Drift arising from a 5 GeV muon, with its velocity directed solely downwards along the z-axis. As the voltage increases, the RPC undergoes a transition from avalanche to saturated avalanche and streamer mode. The latter, marked by multiple sequential avalanches, is induced by the high electric field propelling a saturated amount of ionized electrons from the gas to the electrode. Figure 4.64 visually captures this transition, representing the signal evolving from a minor bump, denoting the electric signal from avalanche, to a more significant signal owing to the
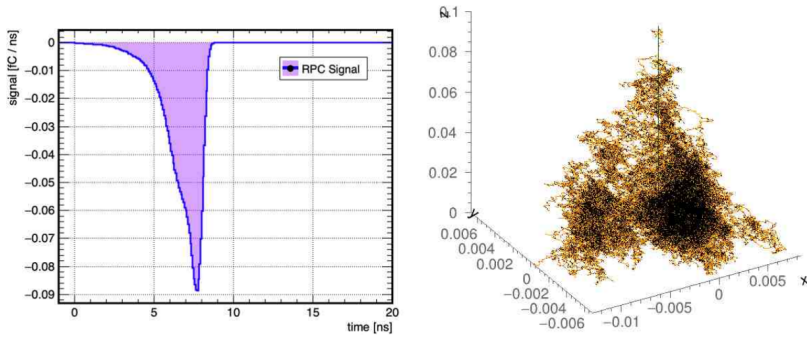
Figure 4.63. Signal and Avalanche Electron Drift (in cm) in ambient conditions and 60 kV/cm.

streamer effect. Upon an increase in gas temperature, molecular interactions
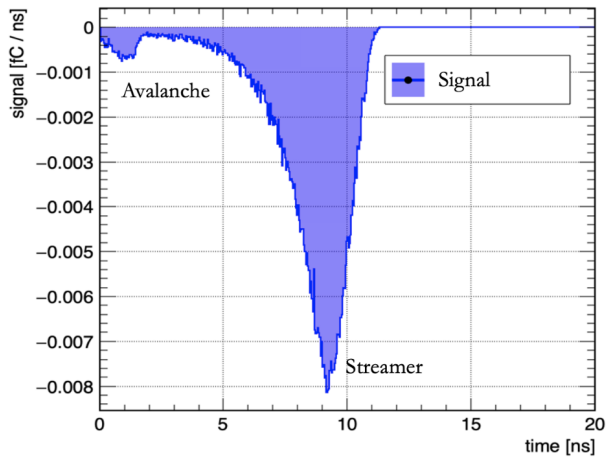
Figure 4.64. Signal showing the Avalanche and Streamer Modes.

intensify, creating a chaotic environment that hinders the penetration of ionized electrons through the gap and into the track. Consequently, elevated temperatures result in a shorter-lived and less intense signal, as evident in Figure 4.65 (b). In this scenario, where the RPC gas is exposed to a high temperature of $50°C$ and an ambient voltage of -5 kV, the recorded signal lasts just over 5 ns, significantly shorter than the typical 10 ns, and exhibits irregular and perturbed patterns. Increasing the electric field propels electrons toward the electrode, facilitating their movement even at elevated temperatures. This phenomenon is demonstrated in Figure 4.65 (c), where the RPC gas experiences both a high $50°C$ temperature and a high -6 kV voltage. Pressure variation has a more profound impact on RPC efficiency compared to temperature changes.
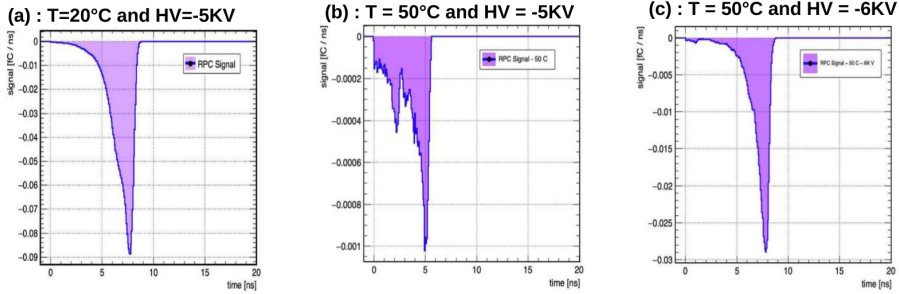
Figure 4.65. ❙ Observing RPC signals under varying temperatures and voltages.
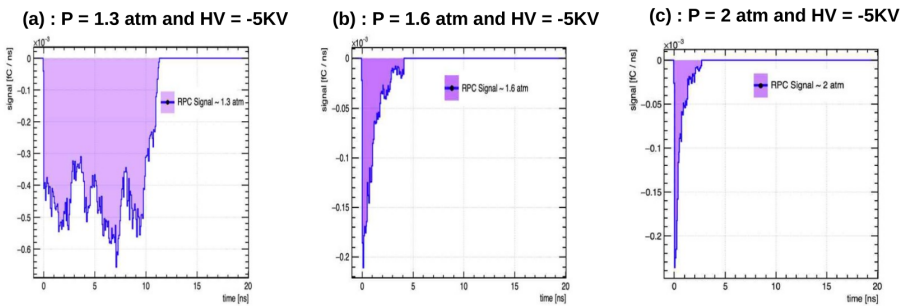
Figure 4.66. ❙ RPC signals under different pressure conditions.

Figure 4.66 illustrates the signal's development for the RPC gas under varying pressures, showcasing how the charge at each time frame decreases to 10^{-3}, and the avalanche duration significantly diminishes.

5. Chapter

Cultural Heritage

Imaging methods based on X-rays have been widely used in the context of cultural heritage preservation [166] due to their ability to penetrate various materials. However, X-ray imaging has limitations when dealing with large or dense objects like compact stone or metal, since they do not penetrate deep enough. Alternative radiation types, such as MeV-range X-rays and neutrons, offer some improvement but face challenges in transporting valuable objects to specialized imaging facilities due to size, weight, and preservation concerns. Various portable setups, such as X-ray fluorescence analysis (XRF) [167, 168] and portable X-ray computed tomography (CT) systems [169], are available for cultural heritage studies, but they have limitations in depth penetration and radiation hazards. Neutron sources [170] offer greater depth [171], but raise concerns about material activation. A recent advancement using a portable proton accelerator [172] shows promise but also suffers from radiation hazard concerns. In contrast, muography represents a promising solution. Cosmogenic muons have remarkable penetrating capabilities, making them ideal for sub-surface imaging in a variety of contexts including cultural heritage applications, including the two main methods: scattering-based and absorption-based, sketched in Figure 5.1 and Figure 5.2 respectively, which is described in sections 1.4.2 and 1.4.1 .
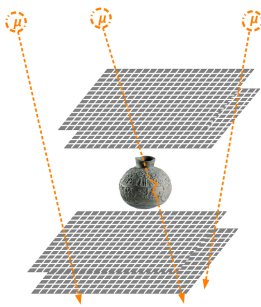
Figure 5.1. | In scattering muography, the object under investigation is "sandwiched" between muon trackers.
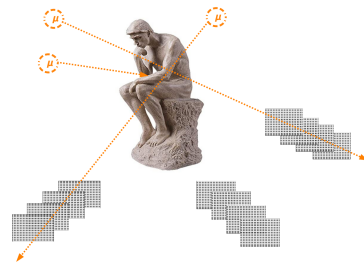
Figure 5.2. | In absorption muography, muon trackers are downstream of the object of interest; 3D imaging can be obtained by combining multiple viewpoints.

Muography has proven to be highly effective in investigating cultural heritage

sites, like The ScanPyramids project alredy described in section 1.4.3. Furthermore, scattering-based muography has been proposed to search for iron chains within the brickwork of the Florence cathedral's dome in Italy [173], and a proof-of-principle test on a mock-up wall was successfully conducted to demonstrate the conceptual validity of the method.

While most examples so far are applications to very large volumes of interest, this study advocates for the adoption of portable and safe muography as a promising imaging approach for cultural heritage studies in a regime that is new for muography (relatively low size) while being beyond reach for methods based on other radiation sources. A preliminary simulation study using GEANT4 [98] illustrates the potential applications and limitations of muography. Subsequently, our discussions delve into the study of measuring momentum and identifying electrons (e-) and positrons (e+). These endeavors are strategically aimed at substantially enhancing the sensitivity of muographic imaging.

Figure **5.3.** ❙ Picture of the wooden statue at the Africa Museum of Tervuren. From project TOCOWO (`https://tocowo.ugent.be/`).

Figure 5.4. ❙ Geant4 simulation setup; green and blue panels represent the scattering and absorption setups, respectively.

5.1. Simulated case studies

Each of the two muography techniques has its own sensitivity, applicability, and limits.

In absorption muography, a single muon tracker is able to measure the 2D projection of matter density, and the combination of measurements from different viewpoints can give a 3D density map. However, it provides no

material discrimination apart from density, and small-size or low-density objects do not stop enough muons to provide sufficient contrast.

In scattering muography, at least two muon trackers are needed, upstream and downstream of the object of interest, to reconstruct the μ trajectory before and after passing through it. This method naturally yields 3D information, and is sensitive to elemental composition because the width of the scattering angle distribution is a function of atomic number Z. However, it is impractical for human-sized statues, as the object of interest must fit between the two trackers. Either the object of interest is moved inside the set-up, or a rather complex installation of the detectors must be performed around the object. Therefore, this method is appropriate for relatively low-size objects.

We perform a Monte Carlo simulation using CRY [84] to generate muons and a Geant4 [98] model of an African statue (Figure 5.3) made of hardwood. This object, 40 cm tall, has been studied with X-rays but its size nears the limit of that method, while it is very small by muography standards. To investigate the potential of muography for material identification, we scale the statue's size by factors two and four and introduce hidden cylinders of different materials within its internal structure, as summarized in Table 5.1. In this first exploratory study, we model an ideal detector (i.e. with 100% efficiency and perfect resolution) made up of nine planes, as illustrated in Figure 5.4. Among these planes, the six indicated in green surround the target and are used for scattering reconstruction, while the remaining three (in blue) are used in the absorption reconstruction study.

Scenario	Statue size [cm^3]	Cylinder material	Cylinder radius [cm]
I (a)	80×30×30	/	/
I (b)	80×30×30	Air	5
I (c)	80×30×30	Bronze bar	5
II	160×60×60	Bronze bar	10

Table 5.1. | Different simulation scenarios.

5.1.1. Scattering reconstruction

Scattering muography is based on the measurement of muon deflections when passing through an object. The deflection angle is measured by extrapolating the incoming and outgoing trajectories observed by the two trackers and determining their point of closest approach (POCA). This approach relies on the interpretation of a POCA point as the actual place where the muon had a single high-energy elastic interaction with a nucleus, neglecting the occurrence of other electromagnetic interactions along its trajectory, which is a rough

approximation of reality but has proven to be effective in many applications (see e.g. [174]). Figure 5.5 shows the distribution of POCA points obtained in the three simulated scenarios denoted as I (a, b, c) in Table 5.1. These plots are based on 5 million muons, roughly corresponding to an acquisition time of ~8 hours, and they show how challenging it is to find a cavity within this kind of statue, as opposed to finding a high-density insertion.
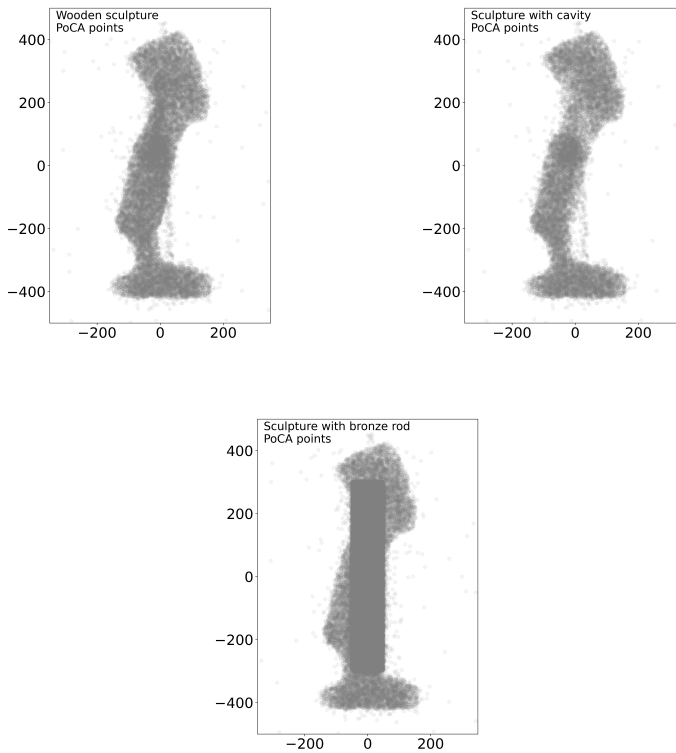
Figure 5.5. ┃ Distribution of POCA points, projected to a 2D plane for clarity, in three simulated scenarios: (left) actual wooden sculpture, (middle) with a cylindrical cavity, (right) with a cylindrical bronze rod.

The output of the muon-scattering reconstruction algorithm is a 3D distribution of POCA points, each associated to a scattering angle. Based on those raw data, some clustering algorithms can be used in order to discriminate between different material densities and elements. At present two methods are employed to analyze the object's content: DBSCAN [175] and a Neighborhood Sum [176] algorithm. DBSCAN only relies on the density of the POCA points, while the Neighborhood Sum method can consider both the density of POCA points

and the scattering angle of the tracks. We apply DBSCAN in two steps, to first remove noise points and then separate the volumes corresponding to different materials using tighter clustering criteria; the result is shown in Figure 5.6. We applied the Neighborhood Sum without (Figure 5.7 left) and with (Figure 5.7 right) considering the additional information from the scattering angles, and we obtain in both cases a good discrimination of the two materials. This discrimination is not as precise as DBSCAN, however this method is more appropriate for scenarios with low exposure times, where POCA points are scarce, and the quantitative results it provides are still reliable.
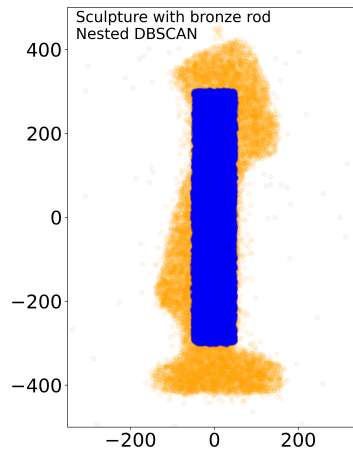
Figure 5.6. ǀ Using DBScan clustering algorithm (blue: hidden bronze bar, yellow: wood statue).

5.1.2. Absorption reconstruction

With the scenario II described in Table 5.1, we explore a challenging regime in which the statue is very big for scattering muography and very small for absorption muography. It is customary in this method, when the volume of interest is very distant from the detector (e.g. when imaging the summit of a volcano), to approximate the latter with a point, meaning that only the zenith and azimuth angles (θ, ϕ) are important while the entry point of the muon in the detector is not. However, to study human-sized sculptures we have in general the possibility to position the detectors very close to the statue, in order to maximize the resolution within the object, and this approximation is no longer valid. For this study we develop a custom back-projection reconstruction algorithm inspired by the methods of Refs. [177,178]. As illustrated
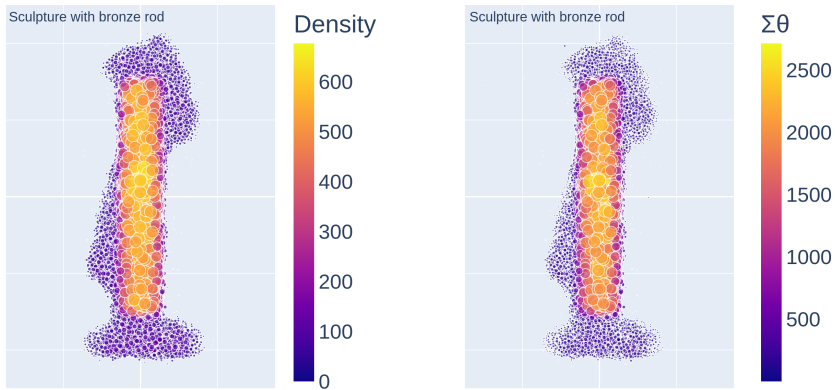
Figure 5.7. | Using Neighborhood Sum clustering algorithm (orange: hidden bronze bar, magenta: wood statue), taking as input only the POCA positions (left) and also the scattering angles (right).

in Figure 5.8, we extrapolate each muon track onto a voxelized volume, and we count the number of times a voxel is hit by this backprojected trajectory. Figure 5.9, based on the equivalent of two hours of data acquisition, shows the 3D transmission map slice by slice in the voxelized volume after selecting only muons with $E < 800\,\text{MeV}$, assuming that the detector setup also contains a way to discriminate the muons above and below this energy threshold. Energy discrimination can be achieved cheaply by introducing a passive absorber before the last detector layer, used as a veto for energetic muons, or more precisely by combining absorption, scattering, time of flight, or other variables.
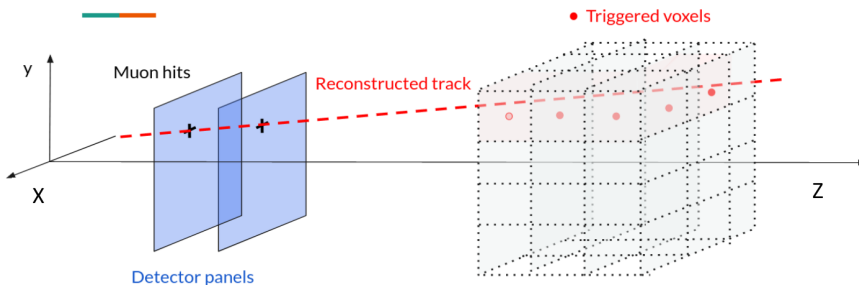
Figure 5.8. | Sketch for the back-projection algorithm.
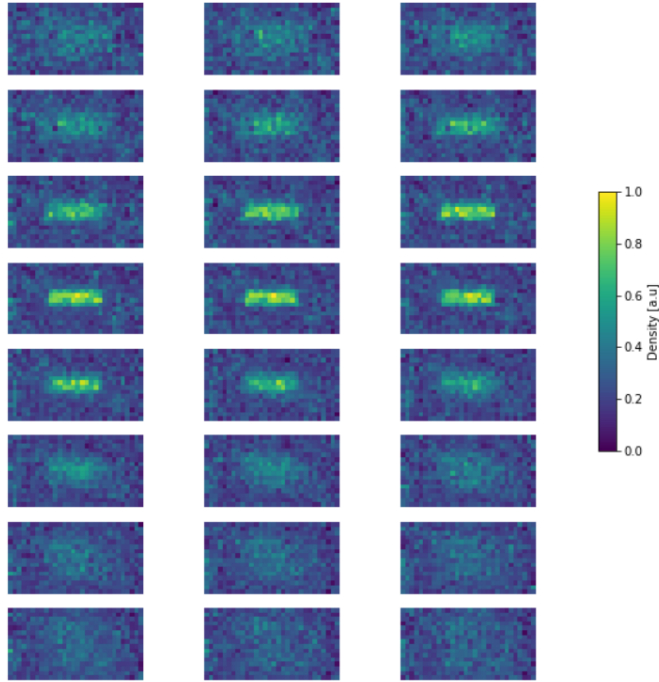
Figure 5.9. ▏ Transmission map slice by slice.

5.1.3. Momentum estimation

In the exploration of momentum estimation techniques for RPCs, our investigation delved into GEANT4 simulations, starting from the generation of cosmic rays using tools like CRY or EcoMug and extending to the intricate details of the detector geometry outlined in section 2.3.2. A well-established method for momentum estimation involves muon scattering. In muon scattering tomography, passive material slabs, often composed of lead or steel, have historically been employed for indirect momentum estimation. This method relies on scattering occurring within a known volume of material and is mathematically expressed through eq. 5.1 :

$$\sigma(\Delta\theta) \sim (13.6 \; MeV \; / \; P) \times \sqrt{x \times \lambda} \tag{5.1.}$$

where $\sigma(\Delta\theta)$ represent the RMS of the angle distribution, P is the particle momentum, expressed in MeV, x is the length of the path within the material, and λ is the scaled scattering density, which depends on the radiation length X_0 (function of the atomic number Z) and on the density of the material as $\lambda = \rho/X_0$. With this definition, λ has units of inverse length. Table 5.2 lists ρ, X_0 and λ of a few materials [10].

Material	$\rho(g/cm^3)$	$X_0(g/cm^2)$	$\lambda = \rho/X_0(cm^{-1})$
Marble	2.71	29.1	0.09
Al	2.7	24.0	0.11
Cu	8.9	12.9	0.70

Table 5.2. ❘ Mass density, radiation length and scaled scattering for a few representatives materials.
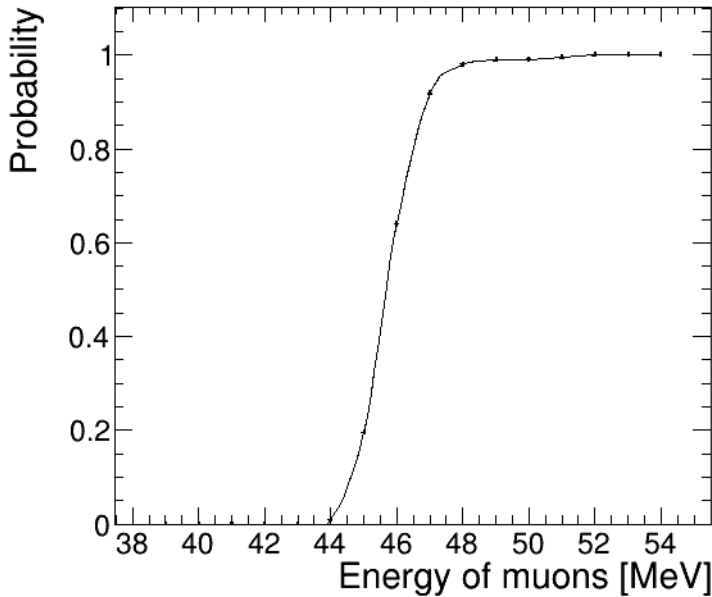
Figure 5.10. ❘ Probabiliy for a muon to survive the passage through our muoscope setup (see Figure 2.8), as a function of its energy.

While effective, this method is not conventionally employed in small detectors due to concerns about reduced portability and muon flux depletion caused by the addition of passive material. However, it's worth noting that passive materials are inherently present in detector casings, such as those enclosing our RPCs. For instance, our current prototype utilizes aluminum casings with varying thickness. Despite aluminum's modest scattering properties, its lower absorption rate is advantageous as it preserves a significant portion of the muon flux. We assessed the feasibility of measuring P with precision under these conditions using GEANT4 simulations.

In a simplified GEANT4 study, three particles traversed our setup illustrated in Figure 2.8, which consisted of 4 RPCs and two scintillator slabs. These particles
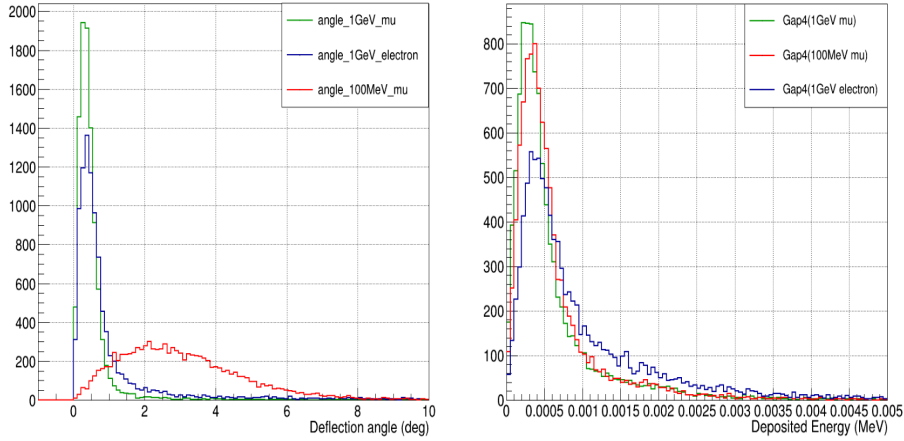
Figure 5.11. Deflection angle with respect to the entry direction (left) and deposited energy in the gas gap of the last RPC (right) for muons of 100 MeV (red) and 1 GeV (green) and electrons of 1 GeV (blue) that cross our current prototype. Simulated with GEANT4.

included a μ with 100 MeV and a μ and an e- with 1 GeV generated using the GEANT4 Particle source generator (GPS). A noticeable difference in deflection was observed between particles with low and high P, primarily due to the aluminum thicknesses (accumulating to approximately 5 cm in this scenario). Calculations based on eq. 5.1 predict a typical deflection of $\sim 0.3^{\circ}$ for 1 GeV and $\sim 3^{\circ}$ for 100 MeV. These predictions align with the outcomes of a detailed GEANT4 simulation, as illustrated in Figure 5.11 (left), where the scattering angle was defined by the angle between the initial (line connecting the first two hits) and final (line connecting the last two hits) trajectories of the same muon. This promising observation indicates the viability of estimating P based on scattering angle without additional passive material.

Furthermore, our RPC setup was enhanced by integrating two plastic scintillator slabs, coupled to photomultiplier tubes (PMT), positioned at the setup's top and bottom. Initially intended as an optional external trigger input as described in section 4.3, these scintillators may additionally provide additional benefits for our multivariate P measurement. They offer an additional, statistically independent measurement of Time of Flight (TOF) and insights into dE/dx, a parameter dependent on P through the Bethe-Bloch formula. The scintillators, 2.9 cm thick with sub-nanosecond time resolution, have room for improvement, such as thickness reduction for enhanced time resolution, although energy loss would increase with larger thickness. Figure 5.12 illustrated the anticipated separation with our current scintillators between the energy loss distributions at 100 MeV and 1 GeV, showcasing the potential for P measurement in RPCs.

(a)   (b)
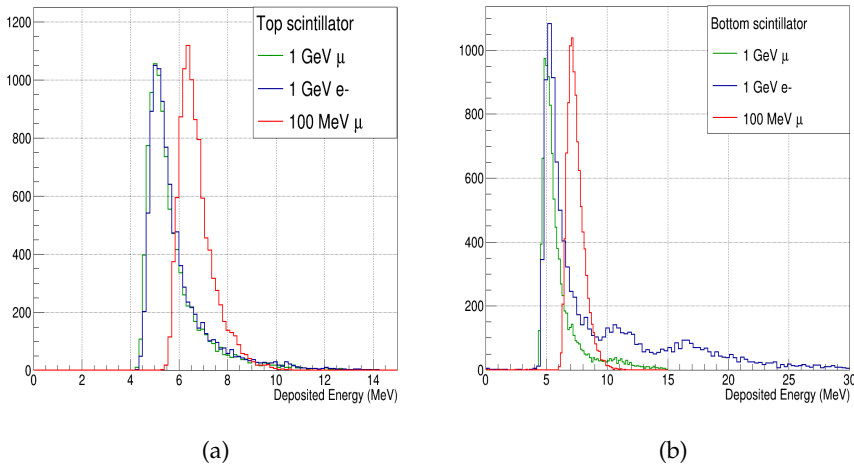
Figure 5.12. ▎ Deposited energy in two scintillators installed at the top and at the bottom of our current prototype, for muons of 100 MeV (red) and 1 GeV (green) and electrons of 1 GeV (blue) that cross our current prototype. Simulated with GEANT4.

5.1.4. Electrons and positrons : From background to signal

Cosmic showers introduce not only muons but also other charged particles, notably protons, electrons, and positrons. While protons pose limited concerns due to strong nuclear interactions, electrons and positrons, being 200 times lighter than muons, exhibit intense electromagnetic interactions. In muography, these particles are usually manageable, as passive materials effectively filter them out. However, reducing the material thickness to lower the P threshold results in higher contamination levels: vertical intensity rises from 0.2, 6 and 30 $Hz/m^2 sr$ for P>1 GeV , 100 MeV and 10 MeV [10]. Combining images from these non-muonic particles can enhance data utility, even if their resolution remains comparatively low.

Figure 5.13 illustrates absorption and scattering-induced blurring for muons, electrons, and positrons of varying energies passing through a marble structure. Despite their weaker flux, electrons and positrons yield higher-contrast images due to stronger absorption. Although their spatial resolution is compromised by increased blurring, precise P estimation, as with muons, can partially restore clarity. This, however, requires accurate P and particle discrimination estimators.

For effective particle discrimination, variables related to scattering (as depicted in Figure 5.11, left) and energy measured in the bottom scintillator (Figure 5.12, right) prove valuable. The scintillator's tail distribution reflects photons emitted during passage through RPC casings, fully absorbed by the scintillator.
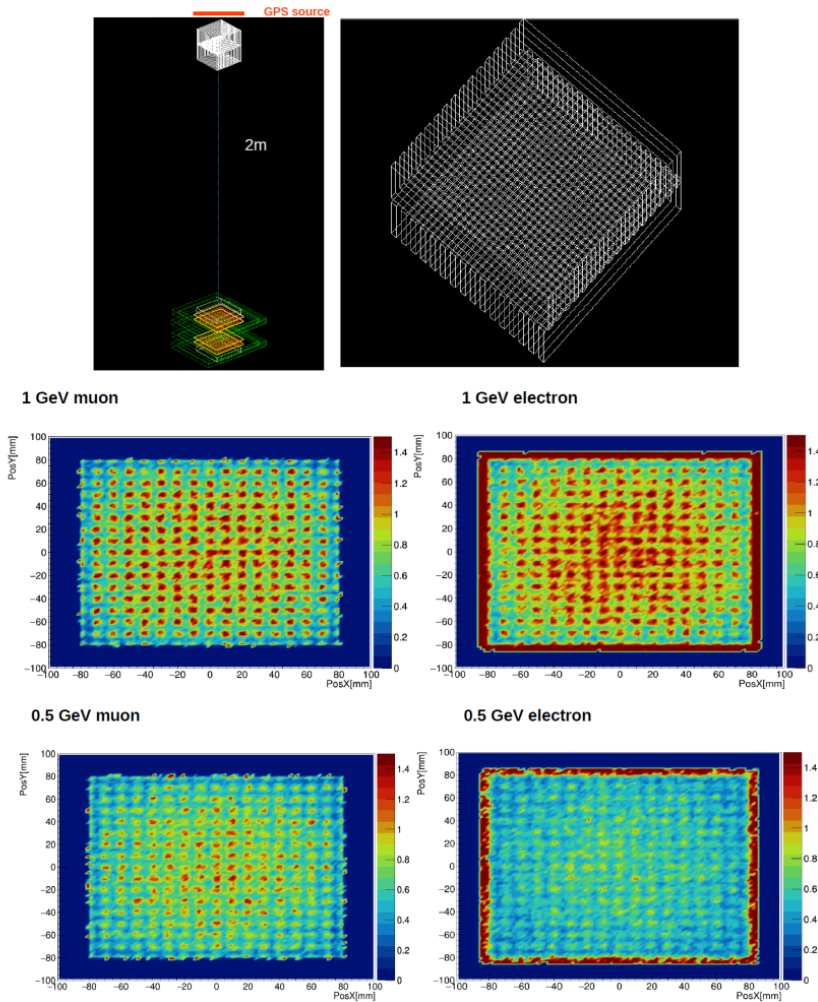
Figure 5.13. ┃ GEANT4 simulation depicting the experiment with the current detector and an idealized $16 \times 16 cm^2$ marble structure within a vacuum environment. Top left: overall setup with muons and electrons generated from the 'GPS source' area (highlighted in red) covering the marble structure. Top right: detailed view of the marble structure, featuring orthogonal layers of 1 cm wide and 5 cm thick alternating marble strips. Bottom panels: Ratio of flux observed by RPCs after absorption and scattering through the marble structure, compared to free-sky flux, for 1 GeV (middle) and 0.5 GeV (bottom) muons (left) and electrons (right). The figures highlight the substantial impact of absorption and scattering on the electron flux, ignoring RPC spatial resolution.

Moreover, differences in energy loss between e± and muons in RPC gas gaps (Figure 5.11, right) offer additional discriminatory power.

In summary, the effective integration of electron-positron ($e\pm$) based images relies heavily on accurate Particle Identification (PID) for distinguishing between electrons and muons. This, in turn, is significantly reliant on detector enhancements that must be both ambitious and feasible. Moreover, there is an interplay momentum (P) and PID estimations. Understanding particle momentum is crucial for accurate PID, and conversely, precise PID information enhances momentum determination. While the conceptual alignment of developing a single algorithm with dual outputs (P and PID) is promising, practical implementation requires careful tuning for optimal performance. It is important to note that working with electrons in reality introduces its own set of complexities, including issues related to scattering at low energies and the potential for bremsstrahlung at high energy, leading to the generation of numerous photons. Achieving successful PID under these conditions demands a complex detector setup.

5.1.5. Artificial muon beam

Muography is inexpensive and portable; thanks to the muon penetration power, it is complementary to other imaging methods. Absorption and scattering have complementary strengths and weaknesses, but some limitations are in common for both: long acquisition times are necessary, due to the relatively low natural rate, and muon direction and energy cannot be controlled.

One potential solution to address these drawbacks is the utilization of an artificial muon beam where both muon energy and direction can be precisely controlled. With even modest precision in these variables and a moderate beam luminosity according to accelerator standards, significant improvements can be achieved compared to using muons from cosmic rays. Figure 5.14 illustrates a 2D XY view of hit position distribution in the detector, normalized with respect to the muons travel distance in statues, with energy beams ranging from 200 to 1000 MeV. This study employed an artificial beam generated by a perpendicular particle generator source, "GPS."

Optimizing beam energy in advance based on the object's size and primary material is feasible. Particularly intriguing is the ability to scan an object with beams of various energies when the inner composition is completely unknown. The accessibility of a portable artificial muon source would be immensely beneficial. However, it is crucial to acknowledge the radiological hazards associated with artificial particle sources, including the byproducts of collisions necessary for muon and antimuon production.
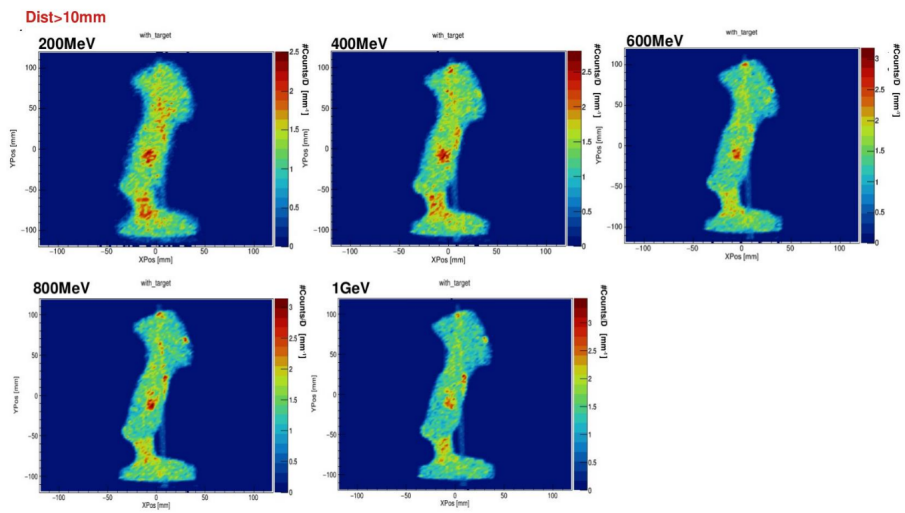
Figure 5.14. | 2D XY view after normalizing with respect to the traveled distance by muon for different energy beam (200-400-600-800-1000MeV).

Conclusion and Prospects

 This thesis focuses on two detectors utilizing distinct technologies: MURAVES and the Portable RPC Muoscope, both designed for muography applications.

The primary objective of the MURAVES experiment is to explore the summit interior of Mt. Vesuvius, targeting the potential existence of a layered structure with materials of varying densities, as proposed by volcanologists. While the experiment is still in its early stages and the analyzed statistics remain low compared to the final goal, notable advancements have been achieved. These include the development of a comprehensive data analysis engine, covering raw data processing to density evaluation. Preliminary results have undergone thorough validation and have been utilized to measure right/left density asymmetry at varying altitudes.

A complete MURAVES simulation chain has been developed. A comparative study involving three cosmic muon generators (CRY, CORSIKA, and EcoMug) was conducted for muon generation, with CRY selected as the primary generator for analysis. The CRY-MUSIC-GEANT4 chain interface has been established, with ongoing efforts dedicated to efficiently simulating the passage of muons through Mt. Vesuvius. PUMAS and MUSIC are utilized for this purpose, with continual validation against GEANT4. The simulation employs a meticulously detailed GEANT4-built geometry of the MURAVES hodoscope to simulate detector response, introducing a novel selection cut based on lead wall-induced scattering for prospective data analysis.

The MURAVES telescope is actively collecting data with the goal of achieving higher significance in the results. Continuous enhancements in simulation and analysis chains are underway to address potential background contaminations and systematics.

This thesis also provides a detailed account of the development and simulation of Resistive Plate Chamber (RPC) detectors. Unlike traditional RPC detectors that operate with gas flow, our focus is on the innovative concept of airtight RPC detectors, particularly relevant in the field of muography. As contributors to the CP3 muography team, we are actively involved in designing portable RPC detectors, known as muoscopes, featuring sealed chambers and an integrated data acquisition system. The current prototype, housing four identical RPCs with a 16×16 cm^2 active area in an airtight aluminum box with an external trigger, achieves up to 80% efficiency. Challenges encountered during development, ranging from creating a homemade resistive coating to designing new

readouts and addressing noise-related issues, have provided valuable learning opportunities.

The muoscope prototype, currently in the research and development stage, has set the stage for the subsequent high-resolution prototype. Observations of electromagnetic interference from the aluminum box have prompted plans for its replacement with a 3D-printed frame, ensuring gas tightness by adhering the resistive plates to the frame. The 3D printer is undergoing testing with various frame materials, and a plastic box will be used for system protection. Looking ahead, future design considerations include the development of a shielding Faraday cage chamber to house the detector. This proactive measure aims to prevent the contamination of noises and ensure optimal performance. The replacement of the CMS front-end module with a 64-channel MAROC 3A chip for each chamber, along with the relocation of strips (which sometimes act as small antennas) to pixels, enables high-resolution muography with precise spatial resolution. Additionally, the implementation of readout boards directly in the gap can be a promising solution to enhance efficiency.

On the simulation front, the use of Garfield++ has provided insights into the physics related to our gas mixture and its environmental performance. Optimizing the link with GEANT4 holds the potential for meaningful data comparisons. The thesis outlines the strengths and limitations of muography for cultural heritage applications and presents a preliminary simulation study involving both scattering and absorption muography for imaging statues with varying sizes and hidden materials. Future work entails a systematic comparison of multiple scenarios, considering material, statue size, hidden volume, detector resolution, and setup geometry to identify the optimal trade-off between cost and statistical identification power, in preparation for actual measurements with test objects.

References

[1] V.F. Hess, *Über Beobachtungen der durchdringenden Strahlung bei sieben Freiballonfahrten*, *Phys. Z.* **13** (1912) 1084.

[2] C. Anderson, *The apparent existence of easily deflectable positives*, *Science* **76** (1932) 238–239.

[3] Neddermeyer, S.H., Anderson and C.D., *Note on the nature of cosmic-ray particles*, *Phys.Rev* **51** (1937) 884.

[4] M. Lattes, G.P.S. Occhailini and C.F. Powell, *Observations on the tracks of slow mesons in photographic emulsions*, *Nature* **160** (October 4, 1947) 453.

[5] G.D. Rochester and C.C. Butler, *Evidence for the existence of new unstable elementary particles*, *Nature* **160** (1947) 855.

[6] T.K. Gaisser, *The cosmic-ray spectrum: from the knee to the ankle*, *Journal of Physics: Conference Series* **47** (2006) 15.

[7] G. Kulikov and G. Khristiansen*JETP* **35** (1958) 635.

[8] P.O. Lagage and C.J. Cesarsky, *Acceleration of cosmic rays*, *Astron. Astrophys* **118** (1983) 223.

[9] B. Peters, *Origin of cosmic radiation*, *Nuovo Cim* **14** (1959) 436–456.

[10] R. Workman and all (Particle Data Group), *Review of particle physics*, *Prog. Theor. Exp. Phys.* (2022) .

[11] V.S. Ptuskin, H.J. Volk, V.N. Zirakashvili and D. Breitschwerdt, *Transport of relativistic nucleons in a galactic wind driven by cosmic rays*, *Astron. Astrophys* **321** (1997) 434.

[12] A. Erlykin, M. Lipski and A. Wolfendale, *High energy cosmic ray spectroscopy. iv. the evidence from direct observations at lower energies and directional anisotropies*, *Astroparticle Physics* **8** (1998) 283.

[13] T. Stanev, *High Energy Cosmic Rays*, Springer Praxis Books (2004).

[14] G. Pfotzer, *Dreifachkoinzidenzen der ultrastrahlung aus vertikaler richtung in der stratosphÄre*, *Zeitschrift für Physik* **102** (1936) 23.

[15] G. Pfotzer, *Dreifachkoinzidenzen der ultrastrahlung aus vertikaler richtung in der stratosphÄre*, *Zeitschrift für Physik* **102** (1936) 41.

[16] H. YUKAWA, *On the Interaction of Elementary Particles. I*, *Proceedings of the Physico-Mathematical Society of Japan. 3rd Series* **17** (1935) 48.

[17] W. Yao and all (Particle Data Group Collaboration), *Review of particle physics*, *Journal of Physics G* **33** (2006) 1.

[18] P.K.F. Grieder, *Extensive air showers*, *Springer-Verlag, Berlin* (2010) .

[19] R.E. Thomas K. Gaisser and E. Resconi, *Cosmic rays and particle physics.*, *Cambriige University Press* (2001) cited on pages 3,4,6,7.

[20] D. Chirkin, *Fluxes of atmospheric leptons at 600 gev - 60 tev, arXiv: High Energy Physics - Phenomenology* (2004) .

[21] D.E. Groom, N.V. Mokhov and S.I. Striganov, *Muon stopping power and range tables 10 mev–100 tev*, *Atomic Data and Nuclear Data Tables* **78** (2001) 183.

[22] W. Leo, *Techniques for Nuclear and Particle Physics Experiments*, Springer (1994).

[23] A. Lechmann and all, *The effect of rock composition on muon tomography measurements*, *Solid Earth* **9** (2018) 1517.

[24] E. Rutherford, *The scattering of alpha and beta particles by matter and the structure of the atom*, *Philosophical Magazine Series 6* **21** (1911) 669.

[25] F. Riggi, *Interaction of muons with matter*, in *Messengers from the Cosmos: An Introduction to the Physics of Cosmic Rays in Its Historical Evolution*, (Cham), pp. 241–247, Springer Nature Switzerland (2023).

[26] E. Keil, *Single and multiple scattering of charged particles*, *Z. Naturf* **15a** (1960) 1031.

[27] G. Moliere, *Theorie der streuung schneller geladener teilchen i. einzelstreuung am abgeschirmten coulomb-feld*, *Zeitschrift für Naturforschung A* **2** (1947) 133.

[28] G. Moliere, *Theorie der streuung schneller geladener teilchen ii mehrfach-und vielfachstreuung*, *Zeitschrift für Naturforschung A* **3** (1948) 78.

[29] G.R. Lynch and O.I. Dahl, *Approximations to multiple coulomb scattering*, *Nucl. Inst. Meth.* **B58** (1991) 6.

[30] E.P. George, *Cosmic Rays Measure Overburden of Tunnel*, *Commonwealth Engineer* **July 1** (1955) 455.

[31] L.W. Alvarez, J.A. Anderson, F.E. Bedwei, J. Burkhard, A. Fakhry, A. Girgis et al., *Search for Hidden Chambers in the Pyramids*, *Science* **167** (1970) 832.

[32] L. Bonechi, R. D'Alessandro and A. Giammanco, *Atmospheric muons as an imaging tool*, *Reviews in Physics* **5** (2020) 100038.

[33] International Atomic Energy Agency, *Muon imaging: Present status and emerging applications*, IAEA TECDOC 2012, IAEA, Vienna (2022).

[34] H.K.M. Tanaka, T. Uchida, M. Tanaka, M. Takeo, J. Oikawa, T. Ohminato et al., *Detecting a mass change inside a volcano by cosmic-ray muon*

radiography (muography): First results from measurements at Asama volcano, Japan, *Geophysical Research Letters* **36** (2009) L17302 [https://agupubs.onlinelibrary.wiley.com/doi/pdf/10.1029/2009GL039448].

[35] L. Oláh, G.G. Barnaföldi, G. Hamar, H.G. Melegh, G. Surányi and D. Varga, *CCC-based muon telescope for examination of natural caves*, *Geoscientific Instrumentation, Methods and Data Systems* **1** (2012) 229.

[36] G. Saracino, F. Ambrosino, L. Bonechi, L. Cimmino, R. D'Alessandro, M. D'Errico et al., *Applications of muon absorption radiography to the fields of archaeology and civil engineering*, *Phil. Trans. R. Soc.* **377** (2018) .

[37] L. Melesio, *The pyramid detectives*, *Phys. World* **27** (2014) 24.

[38] A. Menchaca-Rocha and all, *Search for cavities in the teotihuacan pyramid of the sun using cosmic muons:preliminary results*, *Proceedings, 10th Latin American Symposium on Nuclear Physics and Applications* **XLASNPA** (2014) 012.

[39] "Scanpyramids." http://www.scanpyramids.org/index-en.html.

[40] K. Morishima and all, *Discovery of a big void in khufu's pyramid by observation of cosmic-ray muons*, *Nature* **552** (2017) 387.

[41] S. Procureur, K. Morishima, M. Kuno and all, *Precise characterization of a corridor-shaped structure in khufu's pyramid by observation of cosmic-ray muons*, *Nat Commun* **14** (2023) 1144.

[42] M. Elkarmoty, J. Rupfle, K. Helal, M. Sholqamy, M. Fath-Elbab, J. Kollofrath et al., *Localization and shape determination of a hidden corridor in the great pyramid of giza using non-destructive testing*, *NDT and E International* **102809** (2023) .

[43] G. Saracino and all, *Imaging of underground cavities with cosmic-ray muons from observations at mt. echia (naples)*, *Sci.Rep* **7** (2017) 1181.

[44] L. Cimmino and all, *3d muography for the search of hidden cavities*, *Sci.Rep* **9** (2019) 2974.

[45] A. Anastasio and all, *The mu-ray experiment. an application of sipm technology to the understanding of volcanic phenomena*, *Nucl.Inst.Meth* **A 718** (2013) 134.

[46] G. Baccani and all, *The mima project. design, construction and performances of a compact hodoscope for muon radiography applications in the context of archaeology and geophysical prospections*, *JINST* **13** (2018) P11001.

[47] K. Nagamine, M. Iwasaki, K. Shimomura and K. Ishida, *Method of probing inner-structure of geophysical substance with the horizontal cosmic-ray muons and possible application to volcanic eruption prediction*, *Nuclear Instruments and Methods in Physics Research Section A: Accelerators, Spectrometers, Detectors and Associated Equipment* **356** (1995) 585.

[48] H.K. Tanaka and all, *High resolution imaging in the inhomogeneous crust with cosmic-ray muon radiography: The density structure below the volcanic crater floor of mt. asama, japan*, Earth and Planetary Science Letters **263** (2007) 103.

[49] H.K.M. Tanaka, T. Kusagaya and H. Shinohara, *Radiographic visualization of magma dynamics in an erupting volcano*, Nature Communications **5** (2014) 3381.

[50] H.K.M. Tanaka, *Japanese volcanoes visualized with muography*, Phil. Trans. R. Soc. A **377** (2019) 20180142.

[51] P. Noli, F. Ambrosino, L. Bonechi, A. Bross, L. Cimmino, R. D'Alessandro et al., *Muography of the puy de dôme*, Annals of Geophysics **60** (2017) .

[52] M. Rosas-Carbajal, K. Jourde, J. Marteau, S. Deroussi, J.-C. Komorowski and D. Gibert, *Three-dimensional density structure of la soufrière de guadeloupe lava dome from simultaneous muon radiographies and gravity data*, Geophysical Research Letters **44** (2017) 6743 [https://agupubs.onlinelibrary.wiley.com/doi/pdf/10.1002/2017GL074285].

[53] D. Carbone and all, *An experiment of muon radiography at mt etna (italy)*, Geophys. J. Int **196** (2013) 633.

[54] V. Tioukov and all, *First muography of stromboli volcano*, Sci. Rep **9** (2019) 6695.

[55] E. Commission, D.-G. for Research, Innovation, P. Zanuttigh, S. Vanini, I. Calliari et al., *Study of the capability of muon tomography to map the material composition inside a blast furnace (Mu-Blast) – Final report*, Publications Office (2018), doi/10.2777/24858.

[56] "Blemab european project." https://www.blemab.eu/project-details.html.

[57] B. collaboration, L. Bonechi, F. Ambrosino, P. Andreetto, G. Bonomi, D. Borselli et al., *Blemab european project: muon imaging technique applied to blast furnaces*, Journal of Instrumentation **17** (2022) C04031.

[58] "The discovery® scanning system." https://www.decisionsciences.com/products-solutions/.

[59] E. Commission, D.-G. for Research, Innovation, G. Calvagno, G. Cortellazzo, P. Checchia et al., *Muons scanner to detect radioactive sources hidden in scrap metal containers (MU-STEEL) – Final report*, Publications Office (2014), doi/10.2777/75975.

[60] L. Malmqvist, G. Jönsson, K. Kristiansson and L. Jacobsson, *Theoretical studies of in-situ rock density determination using cosmic-ray muon intensity measurements with application in mining geophysics*, Geophysics **44** (1979) 1549.

[61] A. Becquerel, *On the invisible rays emitted by phosphorescent bodies*, *Comptes Rendues* **122** (1896) 501.

[62] K. Niwa, K. Hoshino and K. Niu, *auto scanning and measuring system for the emulsion chamber*, *Proceedings of the International Cosmic Ray Symposium on High Energy Phenomena* **149** (1974) .

[63] J. Konijn, R. Oldeman, C. van der Poel, J. Uiterwijk, E. Eskut, G. Onengüt et al., *The chorus experiment*, *Nuclear Physics B - Proceedings Supplements* **48** (1996) 183.

[64] A. Ereditato, P.E. Strolin and K. Niwa, *Opera: an emulsion detector for a long baseline μ - oscillation search*, *Nucl. Phys. Proc. Suppl.* **66** (1998) 423.

[65] A. Ariga and all, *A nuclear emulsion detector for the muon radiography of a glacier structure*, *Instruments* **2** (2018) .

[66] W. Crookes, *Certain properties of the emanations of radium*, *Chemical News* **87** (1903) 241.

[67] D. Mahon, A. Clarkson, S. Gardner, D. Ireland, R. Jebali, R. Kaiser et al., *First-of-a-kind muography for nuclear waste characterization*, *Philosophical Transactions of the Royal Society A: Mathematical, Physical and Engineering Sciences* **377** (2019) 20180048 [https://royalsocietypublishing.org/doi/pdf/10.1098/rsta.2018.0048].

[68] A. Bonneville, R. Kouzes, J. Yamaoka, A. Lintereur, J. Flygare, G.S. Varner et al., *Borehole muography of subsurface reservoirs*, *Philosophical Transactions of the Royal Society A: Mathematical, Physical and Engineering Sciences* **377** (2019) 20180060 [https://royalsocietypublishing.org/doi/pdf/10.1098/rsta.2018.0060].

[69] G. Charpak, R. Bouclier, T. Bressani, J. Favier and Zupančič, *The use of multiwire proportional counters to select and localize charged particles*, *Nuclear Instruments and Methods* **62** (1968) 262.

[70] F. Sauli, *Gaseous Radiation Detectors: Fundamentals and Applications*, Cambridge Monographs on Particle Physics, Nuclear Physics and Cosmology, Cambridge University Press (2014), 10.1017/CBO9781107337701.

[71] D. Varga, G. Nyitrai, G. Hamar, G. Galgóczi, L. Oláh, H. Tanaka et al., *Detector developments for high performance Muography applications*, *Nuclear Instruments and Methods in Physics Research Section A: Accelerators, Spectrometers, Detectors and Associated Equipment* **958** (2020) 162236.

[72] R.C. Fernow, *Drift chambers*, in *Introduction to Experimental Particle Physics*, p. 234–258, Cambridge University Press (1986).

[73] N.I. Bozhko, A.A. Borisov, A.S. Kozhin and R.M. Fakhrutdinov, *Cosmic-Ray Muon Tomography Setup: Long-Term Life of Drift Tube*

Chambers, *Physics of Atomic Nuclei* **83** (2020) 258.

[74] J. Burns, S. Quillin, M. Stapleton, C. Steer and S. Snow, *A drift chamber tracking system for muon scattering tomography applications*, *Journal of Instrumentation* **10** (2015) P10041.

[75] V. Anghel, J. Armitage, J. Botte, K. Boudjemline, D. Bryman, E. Charles et al., *Cosmic ray muon tomography system using drift chambers for the detection of Special Nuclear Materials*, *IEEE Nuclear Science Symposium Conference Record* (2010) .

[76] Y. Giomataris, P. Rebourgeard, J. Robert and G. Charpak, *MICROMEGAS: a high-granularity position-sensitive gaseous detector for high particle-flux environments*, *Nuclear Instruments and Methods in Physics Research Section A: Accelerators, Spectrometers, Detectors and Associated Equipment* **376** (1996) 29.

[77] H. Gómez, *Muon tomography using micromegas detectors: From archaeology to nuclear safety applications*, *Nuclear Instruments and Methods in Physics Research Section A: Accelerators, Spectrometers, Detectors and Associated Equipment* **936** (2019) 14.

[78] F. Sauli, *The gas electron multiplier (gem): Operating principles and applications*, *Nuclear Instruments and Methods in Physics Research Section A: Accelerators, Spectrometers, Detectors and Associated Equipment* **805** (2016) 2.

[79] M. Hohlmann, K. Gnanvo, L. Grasso, J. Locke, A. Quintero and D. Mitra, *Design and construction of a first prototype muon tomography system with gem detectors for the detection of nuclear contraband*, in *Proceedings of the 2009 IEEE Nuclear Science Symposium Conference Record (NSS/MIC)*, (Orlando, FL, USA), pp. 971–975, IEEE, October, 2009.

[80] K. Gnanvo and et al., *Detection and imaging of high-z materials with a muon tomography station using gem detectors*, in *Nuclear Science Symposium Conference Record (NSS/MIC), IEEE*, IEEE, 2010, DOI.

[81] K. Gnanvo and et al., *Imaging of high-z material for nuclear contraband detection with a minimal prototype of a muon tomography station based on gem detectors*, *Nuclear Instruments and Methods in Physics Research Section A* **652** (2011) 16.

[82] P. Teixeira, A. Blanco, B. Caldeira, B. Tomé, I. Alexandre, J. Matos et al., *Advancements in the LouMu project– muography for geophysical surveys in meteorology and geophysics 2023*, (2023).

[83] C. Cârloganu, *Density imaging of volcanoes with atmospheric muons using GRPCs*, vol. 055, 2011.

[84] C. Hagmann, D. Lange and D. Wright, *Cosmic-ray shower generator (CRY) for Monte Carlo transport codes*, in *2007 IEEE Nuclear Science Symposium*

Conference Record, vol. 2, pp. 1143–1146, IEEE, 2007.

[85] D. Heck et al., *CORSIKA: A Monte Carlo Code to Simulate Extensive Air Showers*, Tech. Rep. FZKA 6019, Forschungszentrum Karlsruhe (1998).

[86] D. Pagano, G. Bonomi, A. Donzella, A. Zenoni, G. Zumerle and N. Zurlo, *EcoMug: An Efficient COsmic MUon Generator for cosmic-ray muon applications*, *Nucl. Inst. Meth. A* **1014** (2021) 165732.

[87] W.R. Nelson, H. Hirayama and D.W.O. Rogers, *The Egs4 Code System*, Tech. Rep. (12, 1985).

[88] K. Kamata and J. Nishimura, *The lateral and the angular structure functions of electron showers*, *Progress of Theoretical Physics Supplement* **6** (1958) 93.

[89] R. Engel, D. Heck, T. Huege, T. Pierog, M. Reininghaus, F. Riehn et al., *Towards a next generation of corsika: a framework for the simulation of particle cascades in astroparticle physics*, *Computing and Software for Big Science* **3** (2019) 1.

[90] M. Reininghaus and R. Ulrich, *Corsika 8–towards a modern framework for the simulation of extensive air showers*, in *EPJ Web of Conferences*, vol. 210, p. 02011, EDP Sciences, 2019.

[91] D. Pelowitz et al., *MCNPX Users Manual Version 2.7.0*, Tech. Rep. LA-CP-11-00438, Los Alamos National Laboratory (2011).

[92] P. Papini, C. Grimani and S. Stephens, *An estimate of the secondary-proton spectrum at small atmospheric depths*, *Il Nuovo Cimento C* **19** (1996) 367.

[93] L. Bonechi, M. Bongi, D. Fedele, M. Grandi, S. Ricciarini, E. Vannuccini, *Development of the ADAMO detector: test with cosmic rays at different zenith angles*, *29th International Cosmic Ray Conference* **9** (2005) 283.

[94] A. Samalan, S. Basnet, L. Bonechi, L. Cimmino, R. D. Alessandro, M. D. Errico, A. Giammanco, R. Karnam, G. Macedonio, M. Moussawi, C. Rendon, G. Saracino, M. Tytgat, *End-to-end simulations of the MUon RAdiography of VESuvius experiment*, *JINST* **17** (2022) C01015 [`2109.14324`].

[95] J. Ranft, *New features in DPMJET version II.5*, Tech. Rep. FZKA 5828, Forschungszentrum Karlsruhe (1999).

[96] H. Fesefeldt, *The Simulation of Hadronic Showers - Physics and Application*, Tech. Rep. PITHA-85/02, RWTH Aachen (1985).

[97] D. Heck, *Low energy hadronic interaction models*, *Nucl. Phys. B Proc. Suppl.* **151** (2006) 127 [`astro-ph/0410735`].

[98] S. Agostinelli et al., *GEANT4 — a simulation toolkit*, *Nucl. Inst. Meth. A* **506** (2003) 250.

[99] M. Dobbs and J.B. Hansen, *The HepMC C++ Monte Carlo event record for High Energy Physics*, *Comput. Phys. Commun.* **134** (2001) 41.

[100] V. Niess, A. Barnoud, C. Cârloganu and E. Le Ménédeu, *Backward Monte-Carlo applied to muon transport*, *Comput. Phys. Comm.* **229** (2018) 54 [`1705.05636`].

[101] V. Niess, *The PUMAS library*, *Comp. Phys. Comm* **279** (2022) 108438 [`2206.01457`].

[102] P. Antonioli et al., *A three-dimensional code for muon propagation through the rock: MUSIC*, *Astropart. Phys.* **7** (1997) 357.

[103] H. Schindler, "Garfield++."
`http : / / garfieldpp . web . cern . ch / garfieldpp /`.

[104] V. Niess, A. Barnoud, C. Cârloganu and O. Martineau-Huynh, *TURTLE: A C library for an optimistic stepping through a topography*, *Comp. Phys. Comm.* **247** (2020) 106952 [`1904.03435`].

[105] S.-I. Abe and T. Sato, *Implementation of muon interaction models in PHITS*, *Journal of Nuclear Science and Technology* **54** (2017) 101.

[106] T. Sato, *Analytical model for estimating terrestrial cosmic ray fluxes nearly anytime and anywhere in the world: Extension of PARMA/EXPACS*, *PloS one* **10** (2015) e0144679.

[107] G. Imbò, *L'attività eruttiva vesuviana e relative osservazioni nel corso nell'intervallo 1906-1944 ed in particolare del parossismo del Marzo 1944*, Stabilimento Tipografico G. Genovese, Napoli (1949).

[108] S. Callier and all, *Easiroc, an easy and versatile readout device for sipm*, *Physics Procedia* **37** (2012) 20.

[109] "Advanced silicon detectors." `http : / / www . advansid . com /`.

[110] M. D'Errico, *Muon radiography applications: the study of the Mt. Vesuvius Great Cone and the search and 3D modeling of underground cavities*, PhD thesis, Università degli studi di Napoli Federico II, 2021.

[111] M. D'Errico et al., *The MURAVES experiment: study of the Vesuvius Great Cone with Muon Radiography*, *Journal for Advanced Instrumentation in Science* **1** (2022) 273 [`arXiv:2202.12000`].

[112] G. Vilardo, G. Ventura, E. Bellucci Sessa and C. Terranova, *Morphometry of the Campi Flegrei caldera (southern Italy)*, *Journal of maps* **9** (2013) 635.

[113] V. Parkhomchuck, Y. Pestov and N. Petrovykh, *A spark counter with large area*, *Nuclear Instruments and Methods* **93** (1971) 269–270.

[114] R. Santonico and R. Cardarelli, *Development of resistive plate counters*, *Nuclear Instruments and Methods* **187** (1981) 377–380.

[115] G. Belli, C. Vecchi, E. Giroletti, R. Guida, G. Musitelli, R. Nardò et al., *Rpcs in biomedical applications*, *Nuclear Physics B-proceedings Supplements - NUCL PHYS B-PROC SUPPL* **158** (2006) 166.

[116] R. Cardarelli, V. Makeev and R. Santonico, *Avalanche and streamer mode operation of resistive plate chambers*, *Nuclear Instruments and Methods in Physics Research Section A: Accelerators, Spectrometers, Detectors and Associated Equipment* **382** (1996) 470.

[117] I. Crotty, J. Lamas Valverde, G. Laurenti, M. Williams and A. Zichichi, *Further studies of avalanche mode operation of resistive parallel plate chambers*, *Nuclear Instruments and Methods in Physics Research Section A: Accelerators, Spectrometers, Detectors and Associated Equipment* **346** (1994) 107.

[118] I. Crotty, J. Lamas Valverde, G. Laurenti, M. Williams and A. Zichichi, *The non-spark mode and high rate operation of resistive parallel plate chambers*, *Nuclear Instruments and Methods in Physics Research Section A: Accelerators, Spectrometers, Detectors and Associated Equipment* **337** (1994) 370.

[119] M. Abbrescia, A. Colaleo, G. Iaselli, M. Maggi, B. Marangelli, S. Natali et al., *Properties of C2H2F4-based gas mixture for avalanche mode operation of resistive plate chambers*, *Nuclear Instruments and Methods in Physics Research Section A: Accelerators, Spectrometers, Detectors and Associated Equipment* **398** (1997) 173.

[120] P. Camarri, R. Cardarelli, A. Ciaccio and R. Santonico, *Streamer suppression with SF6 in RPCs operated in avalanche mode*, *Nuclear Instruments and Methods in Physics Research Section A: Accelerators, Spectrometers, Detectors and Associated Equipment* **414** (1998) 317.

[121] E. Cerron Zeballos, I. Crotty, D. Hatzifotiadou, J. Lamas Valverde, S. Neupane, M. Williams et al., *A new type of resistive plate chamber: The multigap RPC*, *Nuclear Instruments and Methods in Physics Research Section A: Accelerators, Spectrometers, Detectors and Associated Equipment* **374** (1996) 132.

[122] M. Williams, *The development of the multigap resistive plate chamber*, *Nuclear Physics B - Proceedings Supplements* **61** (1998) 250.

[123] M. Abbrescia, A. Colaleo, G. Iaselli, F. Loddo, M. Maggi, B. Marangelli et al., *The RPC system for the CMS experiment at the LHC*, *Nuclear Instruments and Methods in Physics Research Section A: Accelerators, Spectrometers, Detectors and Associated Equipment* **508** (2003) 137.

[124] G. Aielli, M. Alviggi, A. Ammosov, M. Biglietti, E. Brambilla, P. Camarri et al., *Test and performances of the RPC trigger chambers of the ATLAS experiment at LHC*, *Nuclear Instruments and Methods in Physics Research Section A: Accelerators, Spectrometers, Detectors and Associated Equipment* **533** (2004) 193.

[125] A. Akindinov, A. Alici, P. Antonioli, S. Arcelli, Y. Baek, M. Basile et al., *Construction and tests of the MRPC detectors for TOF in ALICE, Nuclear Instruments and Methods in Physics Research Section A: Accelerators, Spectrometers, Detectors and Associated Equipment* **602** (2009) 658.

[126] CALICE collaboration, *Description and stability of a RPC-based calorimeter in electromagnetic and hadronic shower environments, JINST* **18** (2023) P03035 [2207.06291].

[127] Editors: Laszlo Olah, Hiroyuki Tanaka, Deszo Varga, *Muography: Exploring Earth's Subsurface with Elementary Particles*, Wiley (2022).

[128] S. Wuyckens, *Development of a compact telescope for cosmic muon flux and density measurements*, Master Thesis, Université catholique de Louvain.

[129] S. Ramo, *Currents Induced by Electron Motion, Proceedings of the IRE* **27** (1939) 584.

[130] W. Riegler, *Induced signals in resistive plate chambers, Nuclear Instruments and Methods in Physics Research Section A: Accelerators, Spectrometers, Detectors and Associated Equipment* **491** (2002) 258.

[131] B. Schnizer, T. Heubrandtner and G. Schweitzer, *Simple models for RPC weighting fields and potentials, Nuclear Instruments and Methods in Physics Research Section A: Accelerators, Spectrometers, Detectors and Associated Equipment* **535** (2004) 554.

[132] M. Abbrescia and al., *Effect of the linseed oil surface treatment on the performance of resistive plate chambers, Nuclear Instruments and Methods* **A394** (1997) 13–20.

[133] G. Aielli and al., *Electrical conduction properties of phenolic-melaminic laminates, Nuclear Instruments and Methods* **A533** (2004) 86–92.

[134] R. Arnaldi and al., *Influence of temperature and humidity on bakelite resistivity, Nuclear Instruments and Methods* **A456** (2000) 140–142.

[135] M. Abbrescia and al., *HF production in CMS-resistive plate chambers, Nucl. Phys. B Proc. Suppl.* **158** (2006) 30–34.

[136] G. Aielli and al., *Fluoride production in RPCs operated with F-compound gases, Nucl. Phys. B Proc. Suppl.* **158** (2006) 143–148.

[137] C. Iacobaeus, P. Fonte, T. Francke, J. Ostling, V. Peskov, J. Rantanen et al., *The development and study of high-position resolution (50m) rpcs for imaging x-rays and uv photons, Nuclear Instruments and Methods in Physics Research Section A: Accelerators, Spectrometers, Detectors and Associated Equipment* **513** (2003) 244.

[138] A. Aloisio and al., *The RPC trigger system of the F/B muon spectrometer at the L3 experiment, Nucl. Instrum. Meth.* **A379** (1996) 552–554.

[139] J.G. Layter, *The CMS muon project: Technical design report*, Tech. Rep. , Geneva: CERN (1997).

[140] E. Cerron Zeballos and al., *A new type of resistive plate chamber: The multi-gap RPC*, *Nucl. Instrum. Meth.* **A374** (1996) 132–135.

[141] P. Fonte, A. Smirnitsky and M. Williams, *A new high-resolution TOF technology*, *Nucl. Instrum. Meth.* **A443** (2000) 201.

[142] S. An and al., *A 20ps timing device - a multigap resistive plate chamber with 24 gas gaps*, *Nucl. Instrum. Meth.* **A594** (2008) 39–43.

[143] P. Fonte and al., *Micro-gap parallel-plate chambers with porous secondary electron emitters*, *Nucl. Instrum. Meth.* **A454** (2000) 260.

[144] R. Guida, B. Mandelli and G. Rigoletti, *Performance studies of rpc detectors with new environmentally friendly gas mixtures in presence of lhc-like radiation background*, *Nuclear Instruments and Methods in Physics Research Section A: Accelerators, Spectrometers, Detectors and Associated Equipment* **958** (2020) 162073.

[145] G. Rigoletti, R. Guida and B. Mandelli, *Studies on RPC detectors operated with environmentally friendly gas mixtures in LHC-like conditions*, *The European Physical Journal Plus* **138** (2023) 841.

[146] X. Xie, G. Aielli, Z. Xue, J. Ge, Y. Sun, H. Liang et al., *A new approach in simulating RPC and searching for the causes of large cluster size of RPC*, *Journal of Instrumentation* **14** (2019) C09012.

[147] Q. Li, X. Xie, Z. Xue, J. Ge and Y. Sun, *A new layout about the graphite layers in RPC*, 2021.

[148] S. Basnet, E.C. Gil, P. Demin, R.M. Gamage, A. Giammanco, M. Moussawi et al., *Towards portable muography with small-area, gas-tight glass Resistive Plate Chambers*, *Journal of Instrumentation* **15** (2020) [2005.09589].

[149] S. Wuyckens, A. Giammanco, P. Demin and E. Cortina Gil, *A portable muon telescope based on small and gas-tight Resistive Plate Chambers*, *Phil. Trans. R. Soc. A* **377** (2018) 0139 [1806.06602].

[150] "Hamamatsu 11411 Photo-multiplier tube." https://www.hamamatsu.com/eu/en/product/optical-sensors/pmt/pmt-module/current-output-type/H11411.html.

[151] "67WR500KLF trimmer potentiometer." https://be.farnell.com/en-BE/tt-electronics-bi-technologies/67wr500klf/trimmer-potentiometer-500kohm/dp/1782676?ost=67wr500k.

[152] "71251-040/0800 DIN female connector."
https://be.farnell.com/en-BE/prehkeytec/71251-040-
0800/socket-din-pcb-4pin/dp/1193183?st=71251.

[153] "QL355TP dual channel power supply."
https://www.tme.eu/html/EN/multichannel-power-supplies-
qlx-series/ramka_11372_EN_pelny.html.

[154] "CAEN N415A 8 Ch autowalk constant fraction discriminato."
https://www.caen.it/products/n842/.

[155] "Teltronix TDS 3014 four channel digital oscilloscope."
https://www.allaboutcircuits.com/test-
measurement/oscilloscopes/tds3000-series-tds-3014/.

[156] W. R. Leo, *Techniques for Nuclear and Particle Physics Experiments*,
Springer-Verlag Berlin Heidelberg GmbH, second rev ed. (1994).

[157] "Trenz Electronic TE0720-03-1CF)."
https://wiki.trenz-electronic.de/display/PD/TE0720+TRM.

[158] W. Maryniak, T. Uehara and M. Noras, *Surface Resistivity and Surface
Resistance Measurements Using a Concentric Ring Probe Technique*,
Application Note 1005 (2003).

[159] "LOCTITE EDAG PM 404 EC." https://www.henkel-
adhesives.com/be/en/product/industrial-inks-and-
coatings/loctite_edag_pm_404ec0.html.

[160] "NRITSU MS2713E spectrum analyzer."
https://www.anritsu.com/en-us/test-
measurement/products/ms2713e.

[161] "Make more mile on VHF."
https://mmmonvhf.de/bcn.php?detail=136.

[162] Gamage R.M.I.D, Basnet Samip, Cortina Gil Eduardo, Giammanco
Andrea, Demin Pavel, Moussawi Marwa et al., *Portable resistive plate
chambers for muography in confined environments*, *E3S Web Conf.* **357** (2022)
01001.

[163] I.B. Smirnov, *Modeling of ionization produced by fast charged particles in
gases*, *Nuclear Instruments and Methods in Physics Research Section A:
Accelerators, Spectrometers, Detectors and Associated Equipment* **554** (2005)
474.

[164] S. Biagi, *Monte carlo simulation of electron drift and diffusion in counting
gases under the influence of electric and magnetic fields*, *Nuclear Instruments
and Methods in Physics Research Section A: Accelerators, Spectrometers,
Detectors and Associated Equipment* **421** (1999) 234.

[165] S.F. Biagi, "Magboltz 11."
`http://magboltz.web.cern.ch/magboltz`.

[166] M.P. Morigi et al., *Application of X-ray computed tomography to cultural heritage diagnostics*, *Applied Physics A* **100** (2010) 653.

[167] A. Bezur et al., *Handheld XRF in Cultural Heritage: A Practical Workbook for Conservators*, Getty Conservation Institute (2020).

[168] S. Ridolfi, *Portable x-ray fluorescence spectrometry for the analyses of cultural heritage*, in *IOP Conference Series: Materials Science and Engineering*, vol. 37, p. 012001, IOP Publishing, 2012.

[169] F. Albertin et al., *X-Ray Computed Tomography In Situ: An Opportunity for Museums and Restoration Laboratories*, *Heritage* **2** (2019) 2028.

[170] P. Kerr et al., *Neutron transmission imaging with a portable DT neutron generator*, *Radiation Detection Technology and Methods* (2022) 1.

[171] N. Kardjilov et al., *Advances in neutron imaging*, *Materials Today* **21** (2018) 652.

[172] F. Taccetti et al., *MACHINA, the Movable Accelerator for Cultural Heritage In-situ Non-destructive Analysis: project overview*, *Rendiconti Lincei. Scienze Fisiche e Naturali* (2023) 1.

[173] E. Guardincerri et al., *Imaging the dome of Santa Maria del Fiore using cosmic rays*, *Phil. Trans. R. Soc. A* **377** (2018) 0136.

[174] S. Barnes, A. Georgadze, A. Giammanco, M. Kiisk, V.A. Kudryavtsev, M. Lagrange et al., *Cosmic-ray tomography for border security*, *Instruments* **7** (2023) 13.

[175] M. Ester et al., *A density-based algorithm for discovering clusters in large spatial databases with noise*, in *KDD-96 proceedings*, no. 34 in 96, pp. 226–231, 1996.

[176] V. Kumar, *Comparative study of gas detectors and their suitability for imaging*, HBNI, Mumbai (2022).

[177] M. Stapleton et al., *Angle statistics reconstruction: a robust reconstruction algorithm for muon scattering tomography*, *JINST* **9** (2014) P11019.

[178] L. Bonechi et al., *A projective reconstruction method of underground or hidden structures using atmospheric muon absorption data*, *JINST* **10** (2015) P02003.